SELECTIVELY OXIDIZED PATTERNED InP-BASED VERTICAL CAVITY SURFACE EMITTING LASERS AND VCSEL ARRAYS

TECHNICAL REPORT NO. SSEL-299
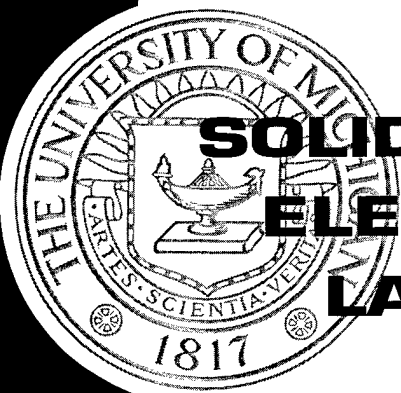
1999

By

Herte Gebretsadik

SOLID-STATE ELECTRONICS LABORATORY

DEPARTMENT OF ELECTRICAL ENGINEERING AND COMPUTER SCIENCE
THE UNIVERSITY OF MICHIGAN, ANN ARBOR

19991022 017

This report has also been submitted as a dissertation in partial fulfillment of the requirements for the degree of Doctor of Philosophy in the University of Michigan, 1999.

TABLE OF CONTENTS

LIST OF FIGURES

LIST OF TABLES

1. INTRODUCTION

1.1 Forward

Since the development of low loss optical fibers over 25 years ago, optical communications has become the system of choice for worldwide communication networks. Some of the many advantages over previous systems include: large transmission bandwidth, immunity to electromagnetic interference, low transmission loss, low weight, low power consumption, and relatively low cost. As multimedia services including the internet, cable television, high definition television (HDTV), and computer links become indispensable in our daily lives, large amounts of data must be transmitted through the information highway. This poses a serious challenge on the current communication network.

The single mode optical fiber widely used in current telecommunication systems have the potential to carry up to 20Tb/s [1-2]. However, it is under-utilized by even the most dense telecommunications networks present today. Unlike traditional time division multiplexing (TDM) techniques, wavelength division multiplexing (WDM) offers a cost-effective utilization of the fiber bandwidth directly in the frequency domain, by allowing multiple optical carriers with slightly different wavelengths to be transmitted on the same fiber[3]. The core of the WDM system is the transmitter, commonly made of a edge-emitting laser diode array. These transmitters must satisfy strict systems

1
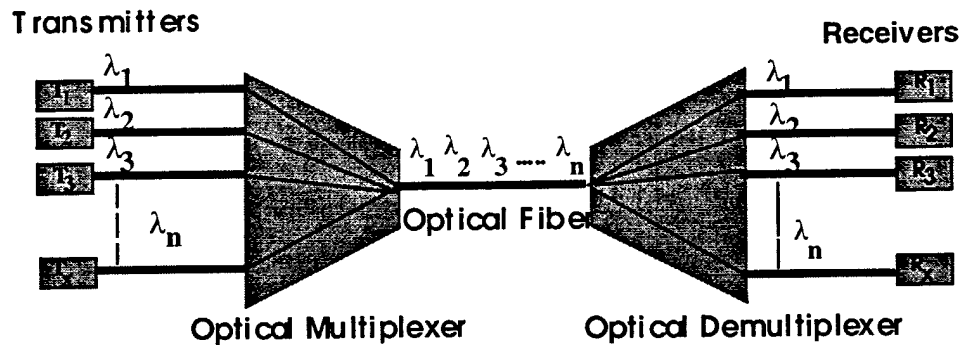
Figure 1.1: Schematic of a typical WDM system

requirements which are based on the size link they serve. These requirements include output powers greater than 1mW, linewidth less than 0.25nm, and threshold current not exceeding 15mA in a 16-Λ WDM link [4]. Additionally, these devices must demonstrate extremely high temperature stability.

1.2 Wavelengths of Interest

Single mode optical fibers have become the most important propagation medium to transmit information in the modern communication systems. Figure 1.2 shows a typical fiber loss curve[5]; while the dispersion spectrum of typical fibers is shown in Fig. 1.3 [6]. It is noted that there are windows at 1.55μm and 1.3μm in which the lowest loss and zero dispersion are located, and hence those are the regions where the highest performance systems operate. In addition, as the erbium-doped fiber amplifier (EDFA) becomes practical [7], pumping lasers at 0.98μm have emerged as important devices. Light sources at these wavelengths also constitute the essential elements in modern optical communication systems.
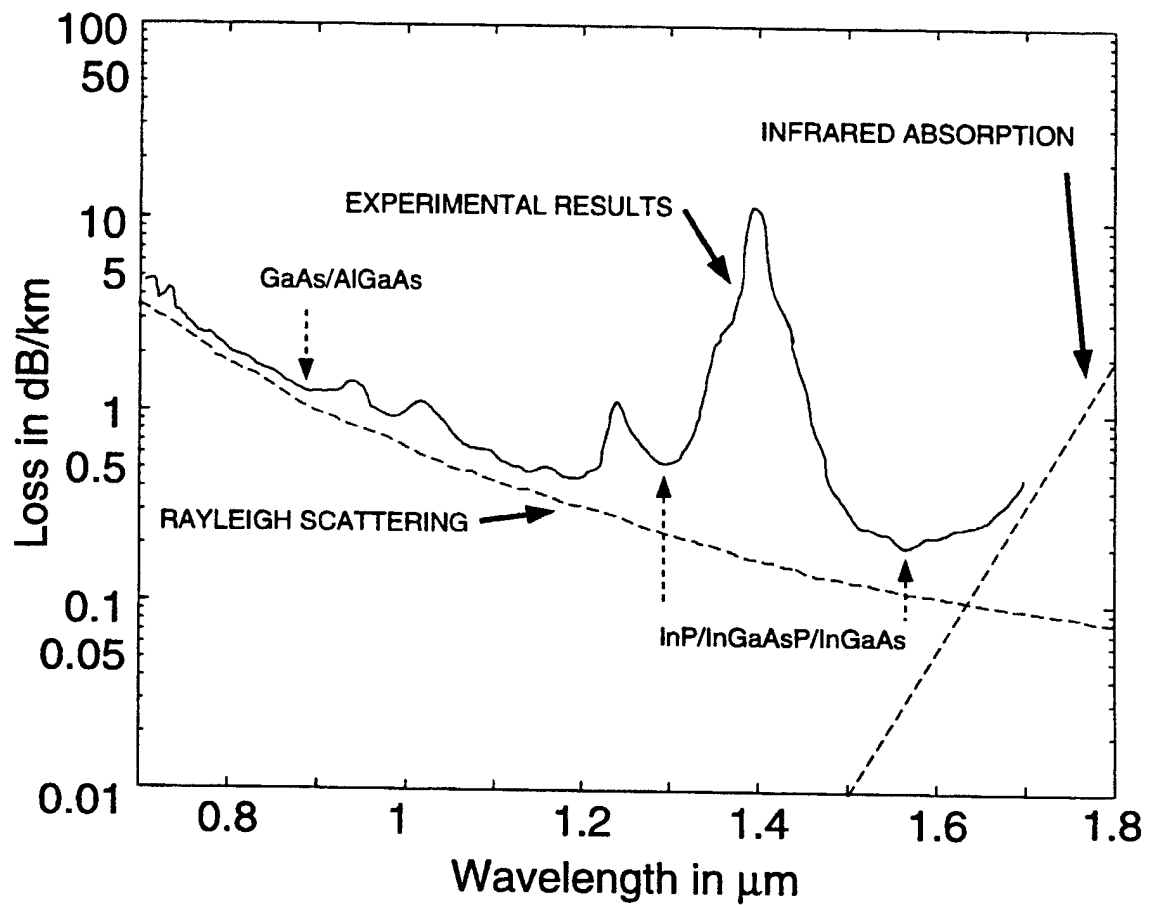
Figure 1.2:   Measured loss spectrum of a typical single-mode silica fiber
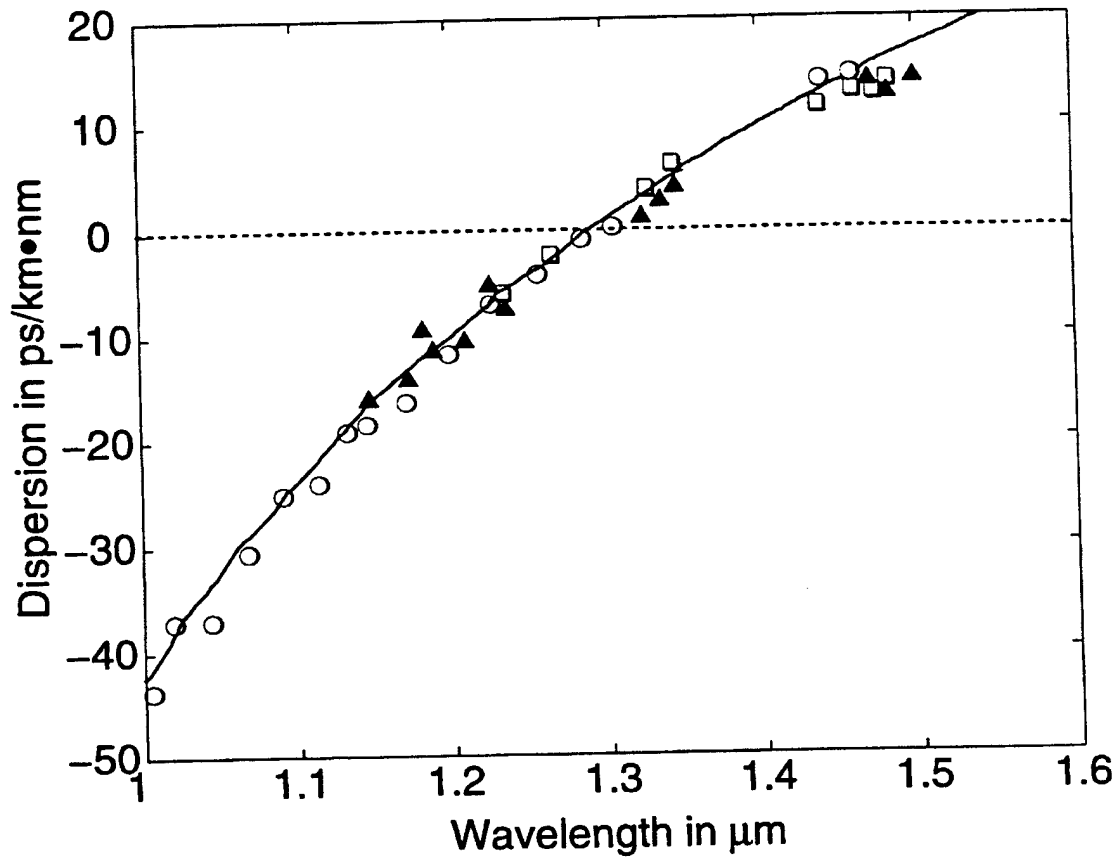
Figure 1.3: Measured material dispersion for typical single-mode silica fibers. Note that at 1~1.3μm, there is a zero cross point.

1.3 Vertical Cavity Surface Emitting Lasers

Vertical cavity surface-emitting lasers (VCSEL) represent an important and major innovation in semiconductor lasers [8]. The first lasing operation of a GaInAsP/InP VCSEL was achieved in 1979 under pulsed conditions at 77K by K. Iga in Japan [9]. In contrast to in-plane lasers (edge-emitting lasers), VCSELs emit light perpendicular to the surface of the semiconductor substrate, as illustrated in Fig. 1.4. This feature allows easy fabrication of 2-dimensional arrays, with beam shapes matching that of single mode fiber. The surface light emission enables wafer level testing which results in far less expensive quality control than for in-plane lasers. In addition to the above mentioned manufacturing issues, VCSELs have ultra-low threshold currents and circular and narrow beam outputs. The short cavity also makes them inherently single longitudinal mode[10]. VCSELs have been most successful at 980 nm wavelength, using compressively strained InGaAs quantum wells (QW) and $Al_xGa_{1-x}As/GaAs$ Distributed Bragg Reflector (DBR) mirrors grown on GaAs substrate [11].
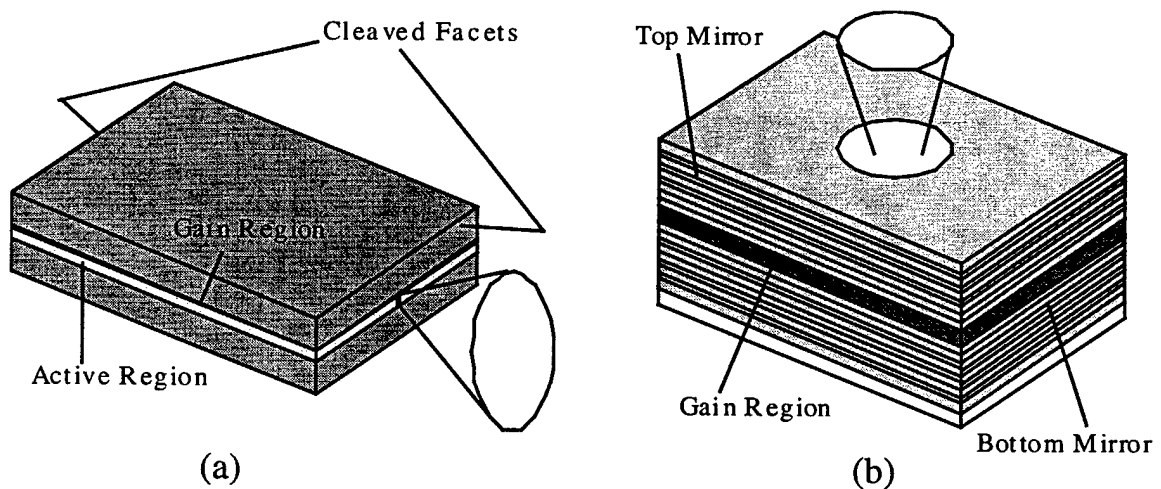
Figure 1.4: Diagrams of conventional semiconductor laser with (a) edge-emission and (b) vertical emission

Recently, GaAs-based VCSELs with wall-plug efficiencies of >50% have been reported, making them comparable to the best in-plane lasers[11].

Optical communications encompasses a broad spectrum of applications to which VCSELs are well suited. Unfortunately, progress in the 1300-1500 nm wavelength regime has been much slower. At these wavelengths, VCSELs would offer an inexpensive replacement for currently-used distributed feedback (DFB) lasers for wavelength division multiplexing (WDM) for long-haul communication applications. WDM is an attractive way to exploit the bandwidth of optical fibers; but such systems have been slow to gain commercial acceptance because of the high cost of WDM components, such as the DFB lasers. 1.55 μm VCSELs could be manufactured inexpensively in WDM arrays.

VCSEL-based optical communication also looks increasingly attractive for short-haul interconnections between buildings, computers, circuit-boards, chips and even devices. Over short distances, the need for extremely low loss and dispersion in fiber is reduced and the need for long wavelength is also eliminated. Thus, short-distance communication applications are also open to near-IR wavelengths or even visible VCSELs.

1.3.1 Status of Long Wavelength VCSELs

Long wavelength VCSELs (LW-VCSELs) have been difficult to develop because epitaxial mirrors are inadequate in the InGaAsP/InP wavelength material system. In the well developed 980 nm VCSELs, the mirrors consist of GaAs and AlGaAs both of which are grown in one epitaxial step as the active region. As can be seen in Figure 1.5, to do the same with 1.55μm and 1.3μm VCSELs, one would use alternate layers of InP and InGaAsP for the mirrors. The refractive index step between InP and InGaAsP for the

mirror is much smaller than that between AlGaAs and GaAs alternating layers. As a result, one needs as many as 45 pairs of InP/InGaAsP layers to achieve the same reflectivity as 25 pairs of AlAs/GaAs as can be seen in Figure 1.6. In addition, the thicker InP/InGaAsP mirror gives a narrower mirror bandwidth and increased sensitivity to absorption, scattering and diffraction losses.

Although an all epitaxial configuration is preferable for most applications for reliability, ease of manufacturing and structural integrity reasons, it is impossible to achieve useful VCSEL operation at 1300/1500nm using epitaxial InP/InGaAsP mirrors alone. Table I describes the available material systems for VCSEL mirror technology with their corresponding refractive indices and normalized thermal conductivities. The normalized thermal resistance of the mirrors giving a fixed reflectivity of 99.9% is used as a figure merit.

(a)   (b)
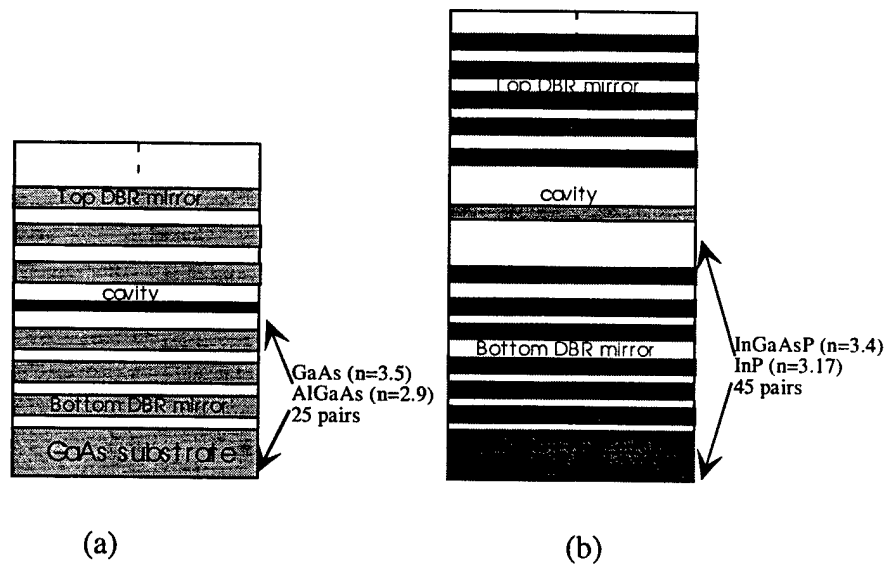
Figure 1.5:   Typical epitaxial grown structure of (a) a GaAs-based 980 nm VCSEL
and, (b) a 155 nm InP-based VCSEL (analogous to 980 nm VCSEL)
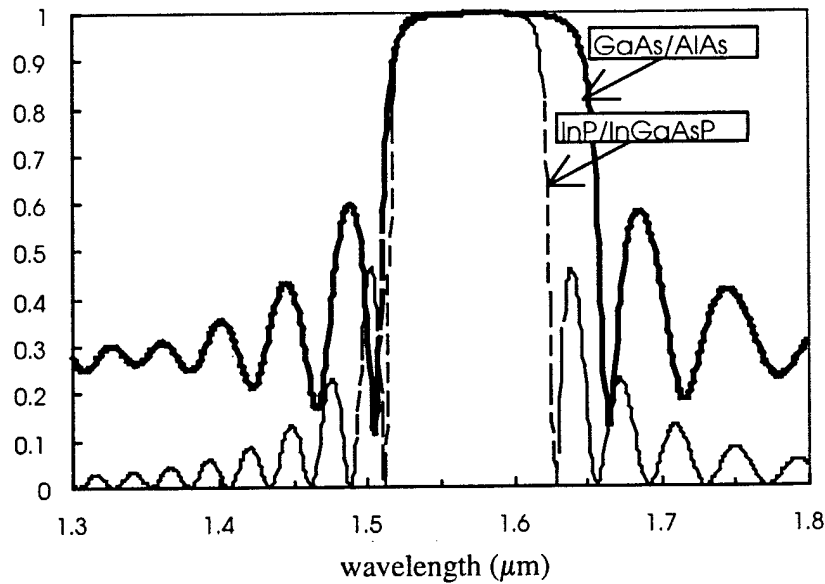
Figure 1.6:   Calculated reflectivities at λ_p=1.55 μm of (a) 45 pairs of InGaAsP/InP
layers and, (b) 25 pairs of GaAs/AlAs layers

The lack of suitable epitaxial mirrors for both sides of the resonator has led to the development of amorphous dielectric mirrors deposited by various low-temperature deposition techniques. These mirrors are high in reflectivity but thermally insulating, and, consequently have kept the InP-based VCSEL's performance at low temperatures and at high threshold for a long time. Much work has been done to develop VCSELs with two dielectric mirrors [12-13], and near-room temperature 1.3 μm operation has been demonstrated. In order to reduce the cavity length, most of the substrate must be removed before the bottom mirror is deposited, which reduces the mechanical stability of the chip and implicates reliability and packaging. One of the most promising VCSELs to date consists of a hybrid structure utilizing one or two GaAs-based mirrors wafer-fused to a InP-based active material[14-15]. These devices benefit from the higher index contrast of GaAs/AlAs and an improved thermal conductivity. The high series resistance of the p-

mirror together with the pronounced intervalence band absorption in p-doped GaAs [16] have been identified as the only limitations for the performance of these lasers. Alternate solutions are the combination of a dielectric p-mirror and wafer fusion of AlGaAs/GaAs [17] or a dielectric/metal hybrid mirror [18]. In both cases, room-temperature (RT) operation at long wavelengths has been demonstrated. However, despite the impressive performance of wafer-fused VCSELs, very little is know on the effect of the fused junctions on the electrical and optical properties or the long-term reliability of the lasers. In addition, the feasibility of wafer fusion on a full wafer scale is still an open issue. Other technologies, which include the growth of metamorphic GaAs-based mirrors on InP VCSEL structures [19], and Sb-based mirrors have also emerged in the past few years[20]. These will be described in detail in upcoming chapters.

Table I: Table showing the high and low refractive indices and the normalized thermal resistances of the various DBR mirror pairs

DBR Mirror Layer Pair	Refractive Index (High/Low)	Normalized Thermal Resistance (R=99.9%) $K\text{-}cm^2/W$
Si/SiO_2	3.61/1.45	36
InGaAsP/InP	3.4/3.2	45
GaAs/AlAs	3.5/2.9	3.9
Si/CaF_2	3.61/1.35	6.4
$GaAs/Al_xO_y$	3.5/1.6	N/A
$ZnSe/CaF_2$	2.54/1.35	N/A

It is therefore worthwhile to investigate all epitaxial 1.55 μm VCSELs, based on a bottom InGaAsP/InP mirror, which can be processed by simple laser fabrication techniques and offer full wafer-fabrication and testing in contrast to the wafer-fused

devices. If realized, such a device would need to be designed for low temperature sensitivity. Additional problems that have been identified in these VCSELs which require consideration include heavy carrier leakage due to Auger recombination, intervalence band absorption (IVBA) (noticeable in the 1.55μm regime), the large valence band offset in InGaAsP/InP and poor thermal conductivities of quaternaries in the InP-based material system .

1.4 The Native Oxide Technology

VCSELs continue to be of interest from both scientific and technological points of view. The DBR mirrors used to provide longitudinal optical confinement have enabled the study of microcavity optical phenomena and are critical to VCSEL performance. In the transverse direction, optical and electrical confinement is commonly achieved using an etched air-post index-guided structures [21] or ion-implanted [22] "gain-guided" devices. Recently, oxides formed from $Al_xGa_{1-x}As$ layers using the selective wet-oxidation technique of Dallessasse and Holonyak [23] have been implemented into both edge-emitting and vertical cavity laser diodes. VCSELs are fabricated using selective oxidation of a buried AlGaAs layer immediately adjacent to the quantum well region to define the lateral extent of the laser cavity, as can be seen in Figure 1.7. This oxidized VCSEL structure minimizes current spreading in the VCSEL, eliminates implantation damage and enables fabrication of ultra-small VCSELs. In GaAs-based VCSELs this technique has led to record-low threshold currents below 40 μA [24], power conversion efficiencies >50% and reduced optical scattering loss [25]. In device sizes below 4 μm, increased spontaneous emission coupling to the lasing mode has also been measured leading to even abrupt drops in threshold. This increased coupling is believed to be due to three-dimensional mode confinement within the spontaneous emission area, resulting

in a narrowing of the far-field due to inhibition of the higher order transverse modes while simultaneously enhancing emission into the lower order Fabry-Perot microcavity quasi-modes [26]. In addition to current and optical confinement, the native oxide technology has been used to form short stack high-contrast DBR mirrors made of selectively oxidized GaAs/AlGaAs mirrors (which form GaAs/Al$_x$O$_y$) which lead to shorter cavity lengths and higher mirror reflectivities [27].

The oxidation technology has also been used to fabricate high density and efficiency two-dimensional VCSEL arrays with record output powers [28]. In contrast to these achievements, advances in the development of InP-based VCSEL have been slower due to the lack of research in the oxidation of Al-bearing compounds lattice-matched to InP.
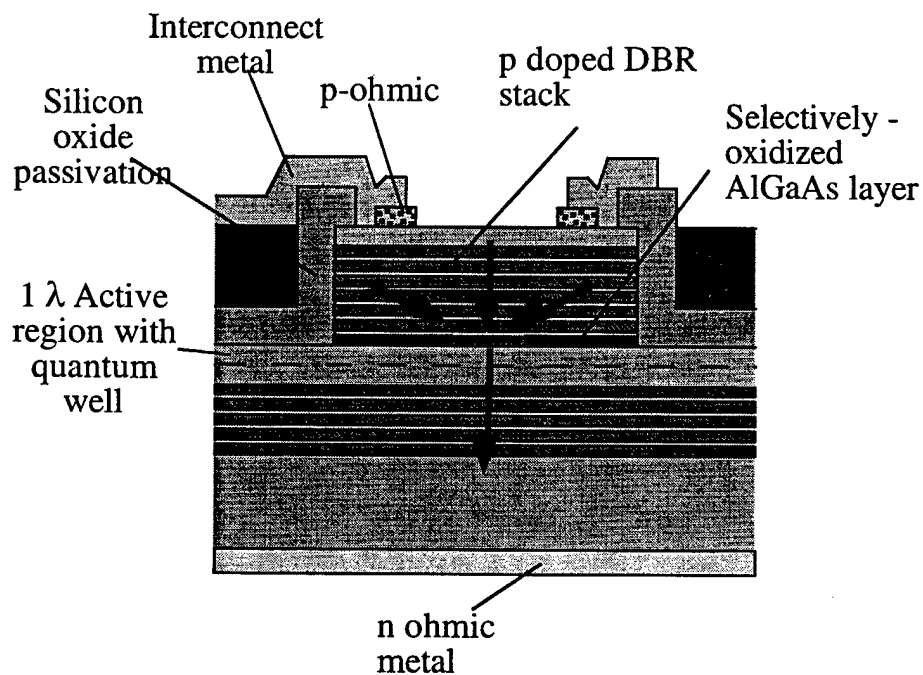
Figure 1.7:   Schematic showing a typical fabricated GaAs-based VCSEL structure with a selectively oxidized high Al-content AlGaAs layer (above the active region)

1.5 Organization of Thesis

This thesis has three specific aims: 1) the design, fabrication and characterization of an all-epitaxial 1.55μm VCSEL suitable for long wavelength optical communication applications; 2) the characterization of the thermal oxidation of InAlAs lattice-matched to InP and its applications to InP-based VCSELs; and 3) the development of a fabrication process and the characterization of selectively-oxidized two-dimensional GaAs-based VCSEL arrays that can be used for high power application.

In the first area, a new type of Distributed Bragg Reflector (DBR) mirror is investigated. A defect-free GaAs-based mirror is directly grown on a patterned InP-based VCSEL heterostructure. The material and optical properties of both the mirror and the VCSEL active layer were studied through a series of photoluminescence experiments, reflectivity measurements and cross-sectional transmission electron microscopy. A brief literature review followed by the growth and characterization of lattice-mismatched mirrors layers on patterned substrates are described in Chapter 2.

In the second area, the lateral wet oxidation of InAlAs is investigated for current and optical confinement in VCSELs. The results of that study and potential applications (including in the 1.55 μm VCSEL with defect-free GaAs-based regrown mirrors) are discussed in Chapter 3. The second part of Chapter 3 describes a study of the recombination characteristicsof minority carriers at the Al_xO_y/gaAs interface by the Light Beam Induced Current Technique (LBIC). This technique yields the surface recombination velocities at the semiconductor/oxide interface formed using GaAs and three different compositions of $Al_xGa_{1-x}As$

Based on the results of Chapters 2 and 3, an all-epitaxial 1.55μm VCSEL is designed. A detailed description of fabrication process integrating both the patterned growth and the selective oxidation of InAlAs and current fabrication results are presented in Chapter 4.

Chapter 5 presents the characterization of the patterned LW-VCSELs and experimental results. These experimental results are analyzed; and performance issues such as thermal stability regarding this device are addressed.

Chapter 6 describes the work done on GaAs-based VCSEL arrays. Although the main focus of this thesis is on LW-VCSELs, GaAs-based VCSEL arrays were also fabricated and characterized for high-power application. The electrical, optical and thermal properties of these arrays are investigated.

Finally, in Chapter 7, the current work is summarized and suggestions are made for future designs, as well as potential application for the continuation of this work.

References

[1] T.P. Lee, et. Al, "Multiwavelength DFB Laser array transmitters for ONTC reconfigurable optical network testbed", *IEEE J. Lightwave Tech.*, Vol. 4(6), pp.967-975, 1996.

[2] S. J. B. Yoo, "Wavelength conversion technologies for WDM network applications," *IEEE J. Lightwave Tech.*, Vol. 14(6), pp.955-966, 1996.

[3] C. A. Brackett, "Dense wavelength divison multiplexing networks: Principles and applications," IEEE Journal of Select. Areas Commun., Vol. 8 pp.948, 1990.

[4] L. S. Lome, "WDM Requirements for High Performance Testbeds," Proceedings of SPIE Vol. 2690 pp. 2-13, 1996.

[5] R. E. Enstrom *et al.*, *Electrochemic. Soc. Ext. Abst.*, Vol.78-1, p.504,1978.

[6] A. Y. Cho, *J. Appl. Phys.*, Vol. 41, p. 2780, 1970.

[7] R. I. Laming et al. "High sensitivity optical pre-amplifier at 10Gbit/s employing a low noise composite EDFA with 46dB gain," post-deadline papers, *Optic. Amplifiers Applic. Topic. Meet. 1992*, Washington D.C., 1992, paper PD 13.

[8] K. Iga, "Surface emitting lasers- materials, ultimate performance, and application', *5th Int. Conf. On InP and Related Materials*, Paris April 1993

[9] H. Soda, K. Iga, C. Kitahara, and Y. Suematsu, "GaInAsP/InP surface emitting lasers", *Jpn. J. of Appl. Phys.*, Vol.18 pp.2329-2330, 1979.

[10] F. Koyama, T. Baba and K. Iga, "Present status and future prospects of long wavelength surface emitting lasers", *European Conf. On Optical Communication*, Firenze, Sept. 1994, pp.TuB4.1.

[11] K. D. Choquette, K. L. Lear, R. P. Schneider, Jr., S. P. Kilcoyne, and K. M. Geib,"Selectively oxidized vertical cavity surface emitting lasers with 50% power conversion efficiencies", *Electron. Lett.*, Vol.31, 208(1995).

[12] T. Baba, Y. Yogo, K. Suzuki, F. Koyama and K. Iga, "Near room temperature continuous wave lasing characteristics of GaInAsP/InP surface emitting laser", *Electron. Lett.*, Vol. 29, 913(1993)

[13] K. Uomi, S. J. Yoo, A. Scherer, R. Bhat, N. C. Andreadakis, C. E. Zah, M. A.Koza, and T. P. Lee, " Low threshold room temperature pulsed operation of a 1.5μm vertical cavity surface emitting laser with an optimized multi-quantum well active layer", *IEEE Photon. Tech. Lett.*, Vol. 6, 317(1994)

[14] J. J. Dudley, D. I. Babic, R,. Mirin, L. Yang, B. I. Miller, R. J. Ram, T. Reynolds, E. L. Lu, and J. E. Bowers, " Low threshold wafer-fused long wavelength vertical cavity lasers", *Appl. Phys. Lett.*, Vol.64, 1463(1994)

[15] D. I Babic, J. J. Dudley, K. Streubel, R. P. Mirin, J. E. Bowers, and E. L. Hu, *Appl. Phys. Lett.*, Vol.66, 1030(1995)

[16] D. Babic, Ph.D. Dissertation, Univ. of California, Santa Barbara, 1995

[17] J. J. Dudley, M. Ishikawa, D. I. Babic, R. Mirin, W. B. Jiang, J. E. Bowers, and E. H. Hu, *Appl. Phys. Lett.*, Vol. 61, 3095(1992)

[18]C. L. Chua, Z. H. Zhu, Y. H. Lo, R. Bhat, and M. Hong, "Low-threshold 1.57- mu m VC-SEL's using strain-compensated quantum wells and oxide/metal backmirror", *IEEE Photon. Tech. Lett*, Vol. 7, 444(1995)

[19] L. Goldstein, C. Fortin. P. Salet, A. Plais, J. Jacquet, A. Rocher and C. Pousson, " Metamorphic GaAs/AlAs Distributed Bragg Reflector Mirrors deposited on InP for $1.3/1.55\mu$m vertical cavity lasers", *IEEE Conference on Indium Phosphide and Related Materials* (IPRM 1997), pp. TuB4

[20] O. Blum, J. F. Klem, K. L. Lear, G. A. Vawter, S. R. Kurtz, "Optically pumped, monolithic, all epitaxial,1.56μm vertical cavity surface emitting laser using Sb-based reflectors", *Electron. Lett.*, Vol. 33(22) pp. 1878-80(1997)

[21] A. Scherer, J. L. Jewell, Y. H. Lee, J. P. Harbison, and L. T. Florez, "fabrication of microlasers and microresonator optical switches", *Appl. Phys. Lett.*, Vol. 55, 2724(1989)

[22] K. Tai, R. J. Fischer, K. W. Wang, S. N. G. Chu, and A.Y. Cho, "Use of implant isolation for fabrication of vertical cavity surface-emitting laser diodes", *Electron. Lett.*, Vol. 25, 1644(1989)

[23] J. M. Dallesasse, N. Holonyak, Jr., A. R. Sugg, T. A. Richard, and N. El-Zein, "Hydrolyzation oxidation of $Al_xGa_{1-x}As$-AlAs-GaAs quantum well heterostructures and superlattices", *Appl. Phys. Lett.*, Vol. 57, 2844(1990).

[24]D. L. Huffaker, L.A. Graham, H. Deng, and D.G. Deppe, "Sub-40μA continuous-wave lasing in an oxidized vertical cavity surface emitting laser", *IEEE Photon. Tech. Lett,*Vol. 8, 974(1996).

[25] B. J. Thibeault, E. R. Hegblom, P. D. Floyd, R. Naone, Y. Akulova and L. A. Coldren, "Reduced optical scattering loss in verticalcavity lasers using a thin (300Å) oxide aperture", IEEE *Photon. Tech. Lett,*Vol.8, 593(1996).

[26] D. L. Huffaker and D. G. Deppe," Spontaneous coupling to planar and index confined quasimodes of Fabry-Perot microcavities", *Appl. Phys. Lett.*, Vol. 67, 2594(1995)

[27]M. H. MacDougal, G. M. Yang, A.E. Bond, C. K. Lin, D. Tishinin and P. D. dapkus,"Electrically-pumped vertical cavity lasers with Al_xO_y/GaAs reflectors", *IEEE Photon. Technol. Lett.*, Vol. 8, pp.310-312, 1996.

[28] D. Francis, H. L. Chen, W. Yuen, G. Li and C. Chang-Hasnain, "Monolithic 2D-VCSEL array with >2W CW and >5W pulsed output power", *Electron. Lett.*, Vol.34(22), 1998.

2. GROWTH OF MISMATCHED MIRROR LAYERS ON InP-BASED PATTERNED HETEROSTRUCTURES

2.1 Motivation

As with many other devices, the development of long wavelength (λ=1.55 μm) InP-based vertical cavity surface emitting lasers (VCSELs) has been less rapid than the GaAs-based devices. Aside from the relative complexities in processing InP-based devices, there are three reasons for this that can be cited: Auger recombination and intervalence band absorption, less applicability of the selective wet oxidation of Al bearing compounds, which has been so effective in 1 μm VCSEL technology, and the difficulty in fabricating high-reflectivity semiconductor Bragg mirrors lattice matched to InP. It is the last factor which poses as the most serious obstacle to the development of InP-based VCSELs. Because of the small refractive index difference between InP and lattice-matched InGaAsP (or InGaAlAs) lattice-matched to it, as many as 45 pairs of λ/4 layers are required to obtain a suitably-high reflectivity [1]. This presents both epitaxy and processing challenges.

The most successful alternate VCSEL designs that have been developed in the past few years are high index contrast dielectric stacks [2-3]and the wafer fusion technology[4]. The former inherently gives rise to current injection problems due to the dielectric materials being poor conductors of heat and electricity. The wafer fusion

technology shown in Figure 2.1(a), in which GaAs/AlAs stacks are fused to both sides of the gain region, does not pose any conductivity problems and looks most promising at the present time. To date, the fusion technology has been the most successful technology. Double-fused VCSEL with $I_{th, min}$ =0.8mA (RT), operating CW up to 64°C (max power 1mW at 15°C) have been reported [5]. However, the reliability of the fusion technique and its application to full size wafers are yet to be ascertained. In addition, multiple substrates are required to complete one wafer and the fusion is limited to small areas. It has also been reported that the fused interface is a major heat source contributing to the total heat generated. In addition, the placement of the current-confining AlGaAs layer, above the fused interface, increases the current spreading distance in the vertical direction [6].

The other two most promising designs in development, (b) an InP-based VCSEL with bulk InGaAs cavity with Sb-based top and bottom mirrors [7] and (c) an InP-based VCSEL with metamorphic GaAs/AlAs DBR mirrors [8] are shown in Fig. 2.1. In (b), the device uses a AlGaAsSb/AlAsSb material system to overcome the small index of refraction change problem (in this case, $\Delta n > 0.52$). The mirror is lattice matched to InP and uses 15 and 20 top and bottom DBR pairs respectively. To date, room temperature operation of this device has not yet been demonstrated. Finally, the design in (c) which uses the metamorphic growth of GaAs/AlAs DBR mirrors on InP-based heterostructures directly by Gas-source MBE eliminates the need for fusion. However, cross-sectional transmission electron microscope images of the overlayers have shown a very high density of threading dislocations in the mirror layers, arising from the strain relaxation due to lattice-mismatched growth [9]. Room temperature pulsed operation of etched post devices has been demonstrated with a very high threshold current density of 509kA/cm^{-2} and peak output power of $4\mu W$. It is also possible that the output power is limited by the high optical loss in the defected mirror layers. In addition, the high density of threading dislocations mayalso lead to rapid degradation of the lasers.

(a)

(b)

(c)
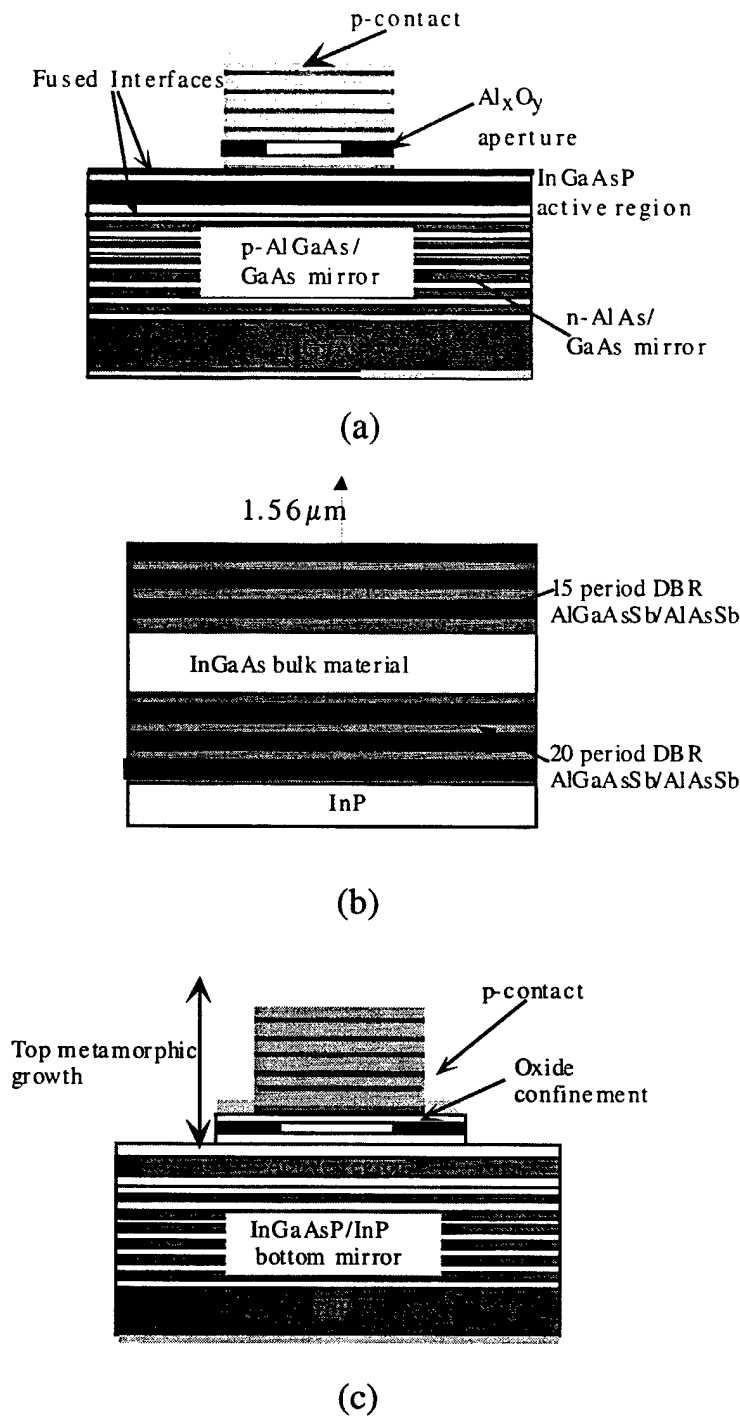
Figure 2.1:   Current InP-based VCSEL technologies: (a) Double-fused InP-
based VCSEL with GaAs-based mirrors: (b) Sb-based VCSEL with
AlGaAsSb/AlAsSb mirrors (c) InP-based VCSEL with metamorphic
GaAs-based mirrors [5,7,8]

Clearly, there is a need for an alternate mirror technology that takes advantage of the intrinsic optical, electrical, and thermal properties of the GaAs/AlGaAs system, which is also compatible with a 2 inch wafer process.

It has been demonstrated that epitaxial growth on *finite* substrates can dramatically reduce the density of threading dislocations from the starting substrate [10] or from the strain relaxation process once the critical thickness is reached during strained layer epitaxy [11], which propagate into the active regions. When the sources of dislocation nucleation at the mesa edge can be minimized, the epitaxial overlayer on the mesa may be relatively defect-free and linear dislocation densities are less than 100 cm^{-1} along one of the <100> directions [10]. Li *et al.* [12], measured the photoresponse of strained $In_xGa_{1-x}As$ ($0.05 \leq x \leq 0.20$) p-i-n photodiodes grown in 30-100 μm grooves of 1 μm depth patterned in (001) GaAs substrates. The thicknesses of the diodes were 1 μm and therefore much larger than the critical thickness. The diodes exhibited enhanced quantum efficiency and temporal response comparable to similar lattice-matched photodiodes on planar substrates.

Since the lateral dimensions of low threshold current VCSELs vary from 2 to 10 μm and the top distributed Bragg reflector (DBR) $\lambda/4$ stack is of similar dimension, it is worthwhile to investigate the possibility of regrowing a GaAs-based DBR directly onto a patterned InP-based VCSEL wafer. In essence the InP-based VCSEL heterostructure would be grown up to the active region; and the wafer would be patterned into mesas, and finally, the GaAs-based mirror heterostructure would be grown on top. The VCSEL would then be fabricated by standard photolithography and metallization techniques.

2.2 Growth on Patterned Substrates

2.2.1 Background: Origin of Strain Induced Misfit Dislocation (MD) and/or Threading Dislocations (TD)

The conventional notion of misfit dislocation (MD) formation is based on thermodynamic ground state energy (or force balance) arguments that equate the strain energy density of an assumed perfect film to the areal energy density associated with a dislocation. The critical thickness h_c, in mismatched epitaxy, given by Mathews and Blakeslee is:

$$h_c = \frac{a_o\left(1 - \frac{v_P}{4}\right)\left[\ln\left(\frac{h_c\sqrt{2}}{a_o}\right) + 1\right]}{2\sqrt{2}\pi a_f(1 + v_P)} \tag{2.1}$$

where a_o is the substrate lattice constant, v_P is the Poisson ratio, h is Planck's constant, c is the velocity of light and a_f is the lattice constant of the epitaxial layer.

Historically, two distinct considerations of strain-induced interface misfit dislocation (MD) formation have been considered. The work of Frank and Van der Merwe [13] relates the occurrence of a MD in strained layers on perfect substrates once a critical thickness is exceeded as described through equilibrium (ground state) considerations. The formation of the MD originates in the nucleation of half-loops at the surface and their expansion under strain (through the glide or climb mechanism) on {111} slip planes for fcc lattices eventually reach the interface and resulting in a strain relieving MD, as can be seen in Figure 2.2. Mathews *et al.* [14] state that the occurrence of a MD arises from pre-existing threading dislocations (TD), or other extrinsic sources such as impurities or pits on the substrate surface. The TD propagates in the grown layer and as the strain builds up, undergoes a lateral motion (through the glide mechanism) because of the shear stress resulting from the misfit on the slip [10].

In both cases, the equilibrium state is taken to be one of a 2-D array of mutually orthogonal misfit dislocations [13]. The extrinsic or intrinsic TDs generated undergo an activated lateral motion with continued growth beyond the critical thickness, until they reach the edges of the mesa. The MD formation provides relaxation of the strain. The conversion of TDs into MDs can be realized to be dependent on substrate size and growth conditions. Therefore, patterning mesas into size comparable to the maximum distance the TD can glide through with continued growth, and under carefully chosen growth conditions, can force the TD to terminate at the mesa edge.

$$A = h < h_c$$
$$B = h > h_c$$

overlayer

substrate
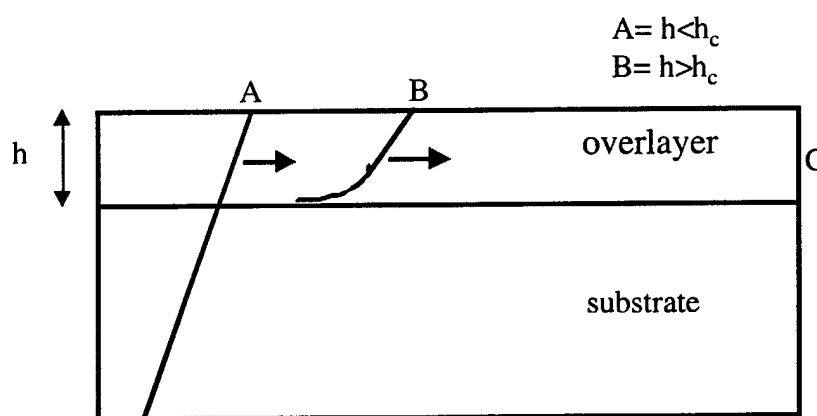
Figure 2.2:   A schematic showing the generation of a misfit dislocation from a threading dislocation. After the critical thickness, the dislocation in the epilayer glides from A to B and C.

Most studies of MD rely on post-regrowth observations; therefore the origin of MD must be deduced from the dislocation structure or the thickness at which the dislocation first forms. The criterion for the critical thickness is vague due to the varying ability of different measurements to detect the onset of MD formation, the metastable nature of pseudomorphic growth from different systems and comparison with incorrect theoretical predictions of the critical thickness, especially in cases when the mismatch is

less than 2%. A consequence of the metastability due to kinetics of MD formation is that the interface dislocation density depends on the size of the growth area.

2.2.2 Reduction of Dislocations

2.2.2.a Reduction in extrinsic sources

The work of Fitzgerald *et al.* [10] demonstrated that growth area is a variable which can be used to study and determine mechanisms of MD nucleation. In doing so, the work suggested that previous theories involving the formation of MD, which focused on the energy (force) balance theory should include the presence of a barrier to MD formation nucleation not included in the critical thickness formula using only strain and dislocation line force energy. Three general categories of MD nucleation were outline: fixed sources, dislocation multiplication and surface half-loop nucleation. The fixed sources are defined as those sources which decrease linearly in number with growth area. Examples of fixed sources are substrate dislocations and surface inhomogeinities. These fixed sources have the lowest activation energies for MD nucleation and are the first to be activated. Once MD sources become active, long MD ensure a high probability of dislocation interaction. One type of dislocation interaction was first described by Hagen and Strunk [15]. In this mechanism, two new MD are produced for every multiplication event and hence, dislocation multiplication is expected to increase the density of MD dramatically. Finally if the overlayer and substrate have a high lattice mismatch, surface nucleation may occur. Homogeneous surface nucleation has a large activation energy and the strain required to activate this mechanism is high.

Therefore, considering growth on small areas and using the existing theory of Mathews *et al.*, the linear interface-dislocation density, n(hkl), along the <hkl> direction was redefined by[10],

$$n = \eta \rho_{ext} \frac{L}{2} \qquad (2.2)$$

where ρ_{ext} is the areal density of extrinsic dislocation sources (ie. existing pits and defects), L is the length of a square mesa and η is the fraction of the extrinsic sources giving rise to the dislocations along the <h k l> direction.
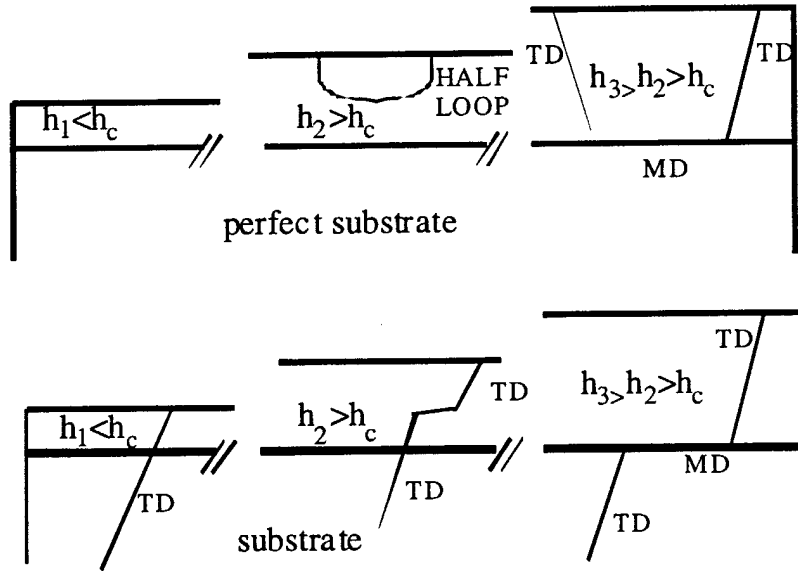
Figure 2.3:   Schematic representation of MD formation models: (a) on defect-free substrates via surface half-loop nucleation and its expansion and (b) on substrates having pre-existing threading dislocations (TD) via perpetuation of the TDs and their subsequent glide.

Thus, the number of low activation energy nucleation sites can be reduced by using high quality substrates and by limiting the size of the growth area. Dislocation interactions are virtually eliminated since the average length of the glide of MDs is small and the probability of dislocation interaction is reduced. Homogenous surface half-loop nucleation will not be affected by the reduction in growth area since it is a function of elastic strain only. Therefore, if the growth area is reduced and the elastic strain is below $\approx 2\%$-6%, very few misfit dislocations will be able to form [10].

2.2.2.b   Reduction in intrinsic sources

(i)   *The thermodynamic argument*:

The influence of a finite size mesa on the behavior of a strained epitaxial layer was also

sought within the same traditional conceptual framework ie. in terms of the behavior of a

fixed number of particles, by seeking their ground state behavior or by examining the

dynamics of an assumed defect. Luryi and Suhir [16] arrived at a less stringent critical

thickness given by :

$$d_{cr} = h_{\infty}(\phi[Ls / 2d_{cr}]f)\qquad(2.3)$$

where h_{∞} is the critical thickness as calculated by the classical formula for growth on an

infinite substrate and, ϕ is a function of the stress field and distance from the interface.

(ii) *The kinetic argument*

This is a fundamentally different concept which considers the kinetic processes intrinsic

to lattice-mismatched growth given a substrate free of pre-existing dislocation sources

(ie. the time dependent evolution of a system with changing number of particles, unlike

the closed system with a fixed number of particles). The central feature of the atomistic

and kinetic approach of defect formation as an integral part of the growth process is the

existence of local strain dependent activation barriers to incorporation of atoms during

growth [17]. The activation barriers for incorporation of atoms at cluster (2D and 3D)

coalescence boundaries and at the edges of large clusters become significant since such

processes demand a correlated displacement of surrounding atoms and are thus high

energy-cost processes. In addition, the activation barriers to atom incorporation are

dependent on the size and shape of the cluster evolution dynamics during growth.

Simulation results based on this evolutionary view of defect formation have revealed that

it is the effective migration length l_m of atoms, under the surface migration rate

(dependent on growth conditions), reactive incorporation rate, and the evaporation rate, in a typical range of strain field, that sets the length scale in the growth of strained systems.

Uncorrelated vacancies at the growing surface that also migrate under the influence of strain with continued growth, and driven by local strain energy gradients, result in defect formation. Madhukar *et al.* [18] investigated the effect of finite mesas and substrate temperature on defect generation probability. The significant drop in defect generation as the mesa size became comparable to the effective migration length was noted. The result showed not only that defect formation is inherently tied to the kinetics of surface migration of atoms and vacancies, but most importantly, revealed the ability of the system to take advantage of strain relief (without extended defect generation) at the free surfaces of the mesa sidewalls.

2.3 Growth and Characterization of Mismatched Mirror Layers

2.3.1 Growth of GaAs-based DBR Mirror on Patterned InP-based Mesa heterostructures

In our study we have investigated the direct growth of GaAs/AlAs DBR mirrors on patterned mesas etched on InP-based multi-quantum well (MQW) heterostructures [19, shown in Figure 2.4. The first structure used, shown in Figure 2.4(a) has four 100Å $In_{0.53}Ga_{0.47}As$ wells separated by 100Å $In_{0.52}Al_{0.48}As$ barriers and is similar to the active region of a 1.55 μm VCSEL and grown on (001) semi-insulating InP substrate. The total thickness of the heterostructure is 0.6 μm. Mesas, varying in diameter from 4-20 μm and 2.5 μm in height were formed using a saturated bromine water (SBW) wet-etch. The patterned wafer undergoes an organic clean and is inserted into the molecular beam epitaxy (MBE) growth chamber for regrowth. The substrate preparation for the regrowth

Figure (a):

x10 — [1186Å GaAs / 1338Å AlAs / 1186Å GaAs]

200Å InGaAs
1000Å InAlAs

x4 — [90Å InAlAs / 100Å InGaAs / 10Å InAlAs]

2000Å InAlAs buffer
2000Å InGaAs buffer

InP Substrate

(a)

Figure (b):

x10 or 25 — [1146Å GaAs / 1336Å AlAs]

x5 — [1100Å InGaAsP λ=1.45 / 1220Å InP]

3330Å InGaAsP λ=1.45
1220Å InP
1174Å InAlAs
1188Å InP
546Å InGaAsP λ=1.42
1200Å strained InGaAsP active layer
546Å InGaAsP λ=1.42
1188Å InP
2196Å InGaAs etch stop

InP n+ substrate

(b)

Figure 2.4: Schematic cross sections and SEM micrographs of regrown GaAs/AlAs Bragg mirrors on (a) InGaAs/InAlAs MQW heterostructure, and (b) InP/InGaAsP MQW VCSEL heterostructure patterned into mesas of sizes ranging 10-40 μm.

consists of 5 minutes oxygen plasma etch followed by a sacrificial layer etch. A thin sacrificial InP layer is usually used and etched in a $HCl:H_2O(1 : 10$ ratio) solution prior to regrowth to avoid contamination due to previous processing steps and to ensure a good growth surface. A 20 seconds $HF:H_2O$ (1:5 ratio) oxide etch is performed prior to loading. A DBR mirror consisting of 10.5 periods of (1186Å)GaAs/(1338Å)AlAs layers, designed for 1.6 μm wavelength, is grown at a substrate temperature of 500°C. The total thickness is 2.7μm. The arsenic to gallium flux ratio was 5. The growth rates were 0.72 μm/hr for GaAs and 0.54 μm/hr for AlAs and the substrate temperature was 510°C. Also shown in the inset of Figure 2.4(a) is the scanning electron micrograph (SEM) of the regrown DBR on the patterned mesa heterostructure. It may be remembered that the Mathews-Blakeslee equilibrium critical thickness, for GaAs on InP is less than 100Å. The second MQW structure shown in Figure 2.4(b), grown by metal-organic vapor phase epitaxy (MOVPE), at 650°C, is a 1.55 μm VCSEL without semiconductor bottom mirrors. Again, mesas of 15-40 μm in diameter and 7 μm in height are delineated and 25 periods of (1146Å) GaAs/(1336Å)AlAs Bragg mirror are regrown by MBE.

2.3.2 Characterization of Regrown Mirror and Active Region

Marked differences are observed in the morphological, optical and structural characteristics of the complete heterostructures in the mesa and off-mesa regions. The surface morphology of the regrown mirrors is featureless on top of the mesas, while distinct cross-hatch pattern is seen in the off-mesa regions. The calculated and measured DBR reflectivities of the 25 periods Bragg mirror on the VCSEL heterostructure (structure 2) are shown in Fig. 2.6. The measurement was done over the largest mesas. The agreement is good.

Following regrowth, PL data from the sample show a strong bound-exciton related peak originating from the bulk GaAs material in the DBR on top of a 20μm mesa

which indicates that the highly mismatched mirrors are of excellent optical quality. Shown in figure 2.5 is the low temperature PL data of the GaAs-based mirror taken on and outside the mesa regions. A PL peak corresponding to the bandgap energy of GaAs is observed on the mesa region, confirming that the optical quality of the regrown mirror grown on mesa is better than on infinite substrate. No peak was detected on the infinite growth area.

In making VCSELs, it is imperative to ascertain that threading dislocations at the GaAs-InGaAs layer, if generated, do not propagate downward and
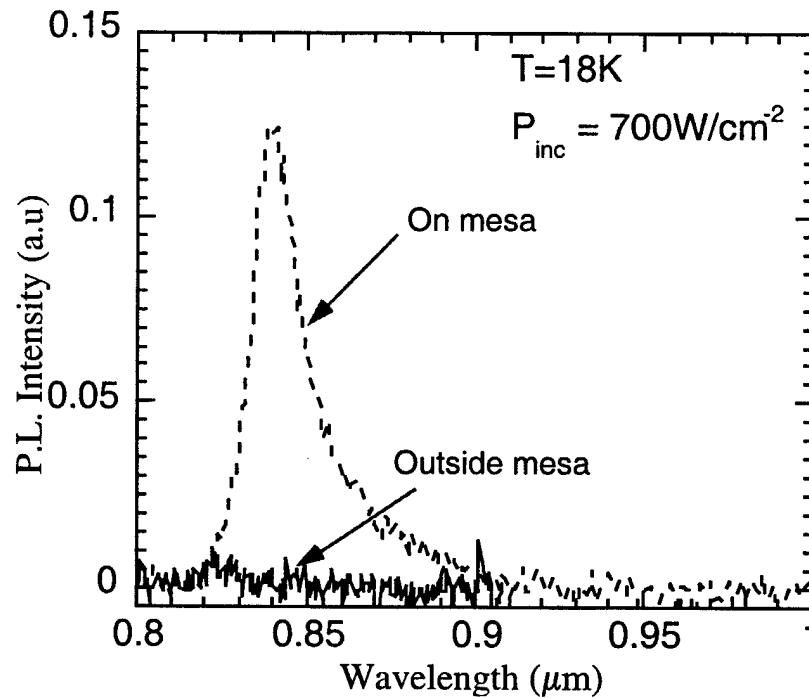
Figure 2.5: Low temperature photoluminescence spectra of the regrown GaAs/AlAs mirror on the etched mesa (dotted) and outside the mesa regions (solid).

(a)

(b)
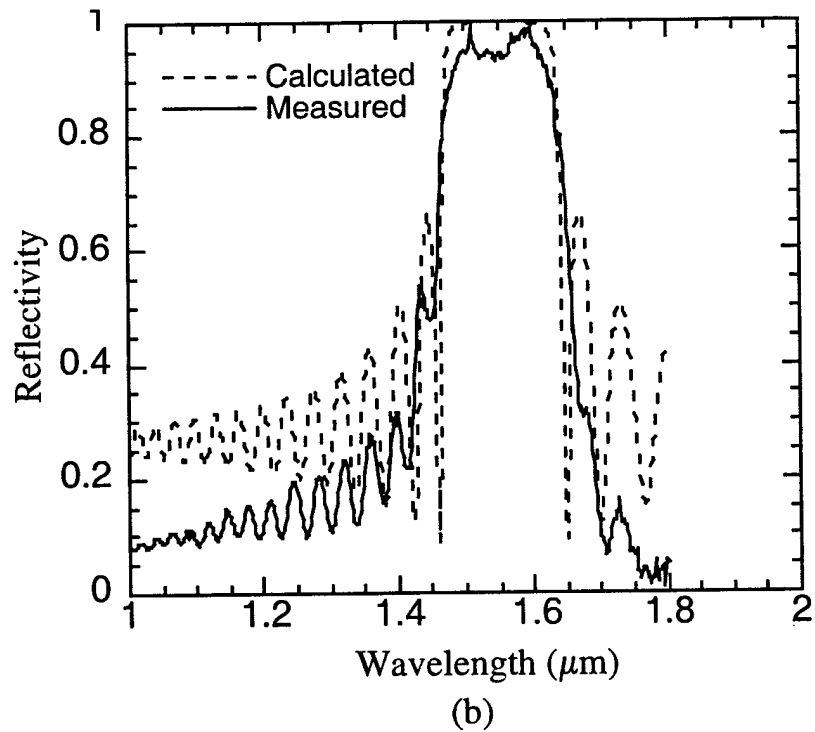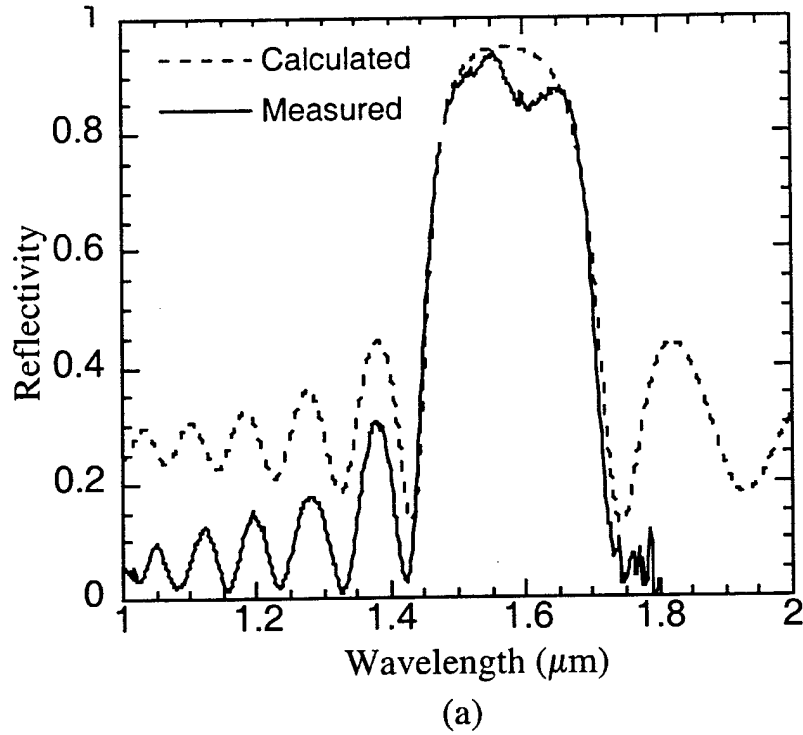
Figure 2.6: Measured and calculated reflectivities of (a) 10 periods on structure 1 and (b) 25 period GaAs/AlAs Bragg mirror for λ_p=1.55 μm grown on structure 2.

deteriorate the optical properties of the active region. Low temperature (18K) photoluminescence (PL) of the InGaAs/ InAlAs quantum wells (structure1) in the different regions and in the different stages of growth and processing were measured with a He-Ne (6328Å) laser, 1 meter spectrometer, a liquid nitrogen cooled Ge detector and lock-in amplification. The low temperature PL of the as-grown quantum well is characterized by a single bound exciton peak at 1.45 μm with a linewidth (FWHM) of 16 meV. Partial removal of the mirror layers by reactive ion etching enabled PL measurement of the MQW region. Shown in Figs. 2.7(a) and (b) are the PL spectra from top of mesas of size 20 μm and 15 μm, respectively. Photoluminescence data from the same mesa prior to regrowth are superimposed for comparison. The PL peak position remains unchanged. A slight decrease in peak intensity for the etched mesa before regrowth, compared to the as-grown sample, is due to the relative PL excitation spot size (30 μm) becoming larger than the mesa size. Additional decrease in PL intensity after regrowth is observed due to absorption of excitation light in the remaining (unetched) GaAs-based mirror layers. The PL linewidth actually decreases with the reduction in mesa size. These characteristics strongly indicate that VCSELs can be fabricated with the regrown heterostructure.

Finally cross-sectional transmission electron microscopy (XTEM), using a JEOL 2000FX microscope, was done on a 40 μm diameter mesa VCSEL (structure 2) sample to examine the possible propagation of defects in the InGaAsP quantum wells and the GaAs/AlAs mirror region. The objective was to study these in a patterned region, for which sample preparation is extremely difficult. Bright-field XTEM images are shown in Fig. 2.8(a) and (b). The two most encouraging features are that the MQW region as well as the DBR region directly above it, are free of defects. In comparison, a XTEM image of the regrown 10 periods DBR on unpatterned structure 1 (InP substrate), shows the generation and propagation of dislocations (see Fig. 2.8(c)), as expected.

2.4 Conclusion

It is evident that growth of GaAs/AlAs Bragg mirrors on patterned 1.55 μm VCSEL structure is feasible. This fabrication technique will allow use of GaAs/Al$_x$O$_y$ mirrors, made by selective wet oxidation of the AlAs layers. From the practical point of view, one might wonder about also replacing the lower epitaxial Bragg mirror. If necessary, this can be done with dielectric multilayers, a combination of metal and dielectric multilayers, or with InP/InGaAsP multilayers[20-21]. In conclusion, it is demonstrated that high quality GaAs/AlAs Bragg mirrors can be grown directly on small mesas patterned on a 1.55 μm InP based VCSEL structure without generating a large defect density and without deterioration of the active region.
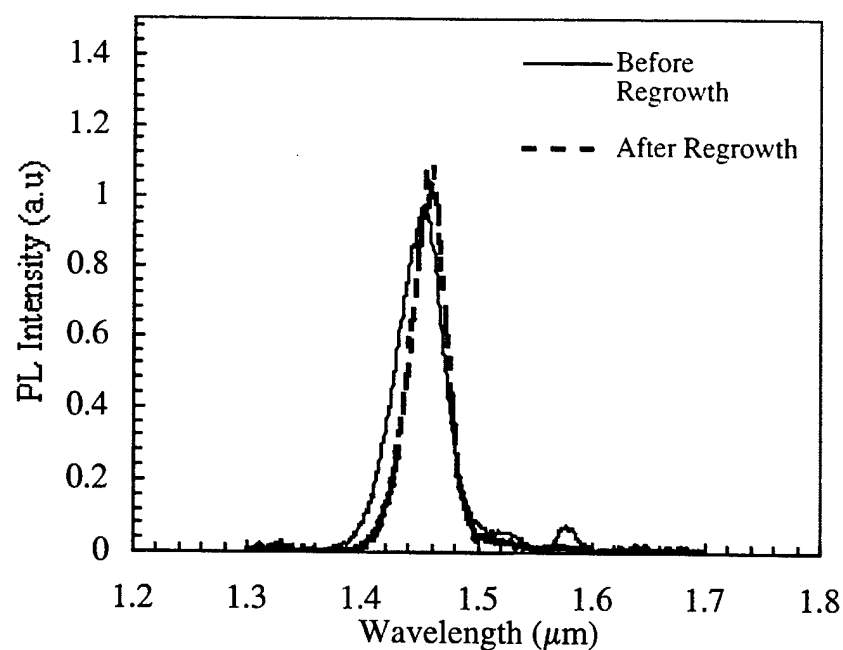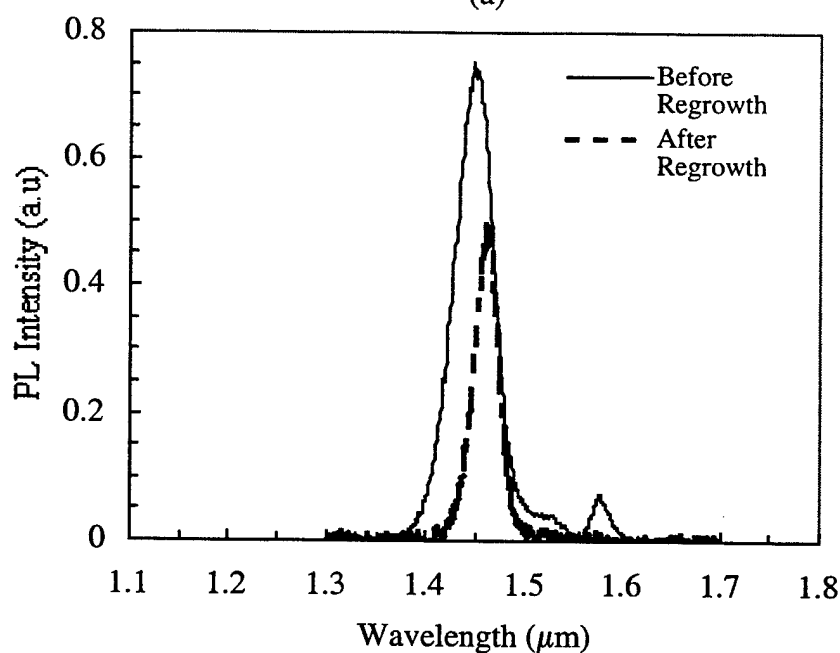
Figure 2.7: Low temperature (17K, P_{inc}= 700W/cm^{-2}) photoluminescence spectra of InGaAs/InAlAs MQW (structure 1) after patterning of mesa compared with spectra after regrowth of 10 periods of GaAs/AlAs DBR for (a)20 μm diameter mesa, and (b)15 μm diameter mesa. The DBRs were partially removed by etching after regrowth to observe the luminescence.

(a)

(b)

(c)
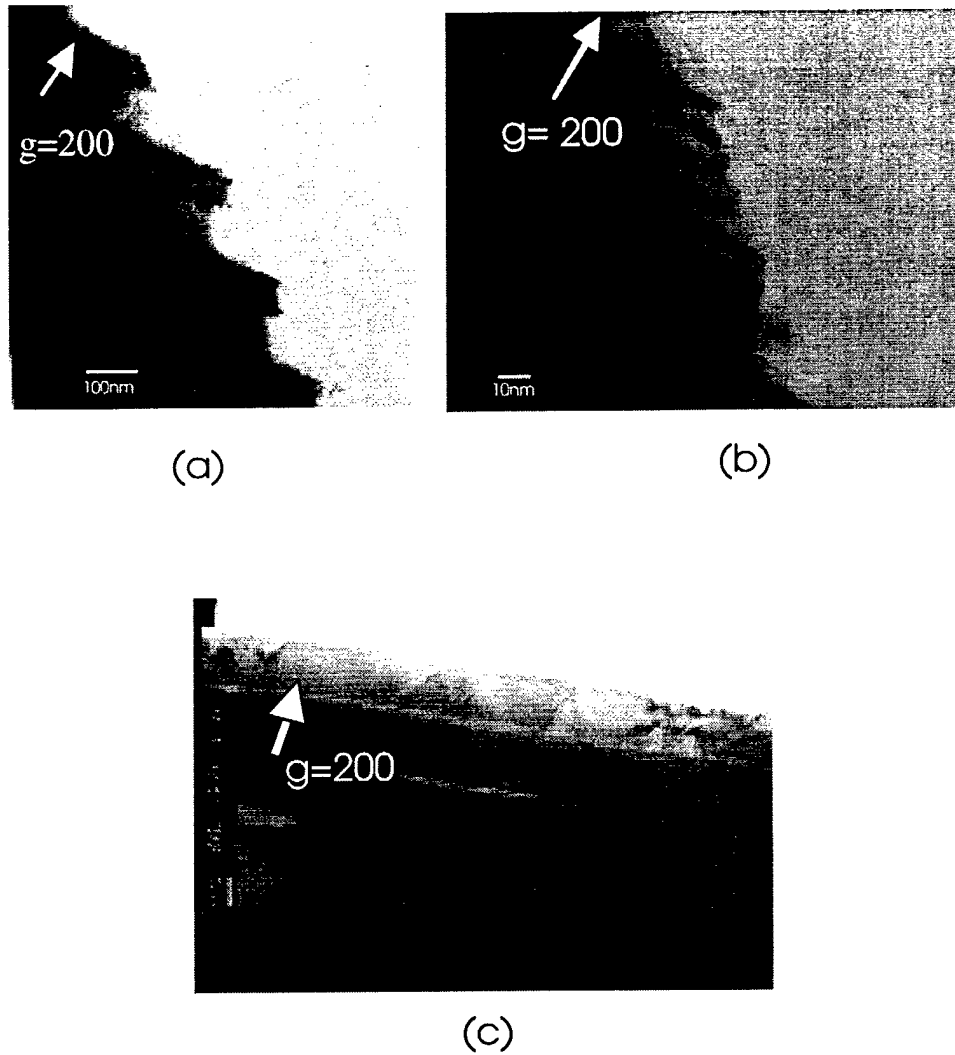
Figure 2.8:   Cross-sectional transmission electron microscopy micrograph of different regions, after regrowth of GaAs/AlAs DBR: (a) regrown DBR layers on mesa (b)quantum well region in VCSEL structure and, (b) regrown DBR layers on "infinite" InP substrate.(TEM by K. Linder, 1997)

References

[1] T. P. Lee, *Current Trends in Vertical Cavity Surface Emitting Lasers*, World Scientific Press, Singapore, 1995.

[2] K. Uomi, S. J. Yoo, A. Scherer, R. Bhat, N. C. Andreakakis, C. E. Zah, M. A. Koza, and T. P. Lee, "Low threshold room temperature pulsed operation of 1.5μm Vertical cavity Surface Emitting Lasers with an optimized multi-quantum well active layer, " *IEEE Photon. Technol. Letters*, vol 6, pp317-319, 1994

[3] T. Baba, K. Suzuki, Y. Yogo, K. Iga, and F. Koyama, "Low threshold room temperature pulsed and –57°C CW operations of a 1.3μm GaInAsP/InP circular planar buried heterstructure surface emitting lasers", *IEEE Photon. Technol. Letters*, Vol. 5, pp.744-746, 1993

[4] D. I. Babic, J. J. Dudley, K. Streubel, R. P. Mirin, J. E. Bowers, and E. L. Hu, " Double fused 1.52μm vertical cavity lasers," *Appl. Phys. Lett.*, Vol. 66, pp.1030-1032

[5] N. M. Margalit, J. Piprek, S. Zhang, D. I. Babic, K. Streubel, R. P. Mirin, J. R. wesselman, J. E. Bowers, E. L. Hu, "64°C continuos wave operation of a 1.5μm vertical cavity laser," *IEEE Journal of Sel. Topics in Quantum Electronics*, vol. 3, pp. 359-365, 1997.

[6] J. Piprek, D. I. Babic, J. E. Bowers, " Simulation and analysis of a 1.55μm double-fused vertical cavity lasers," *J. Appl. Phys.*, Vol. 81(8), pp-3382-3390, 1997.

[7] O. Blum, J. F. Klem, K. L. Lear, G. A. Vawter, S. R. Kurtz, "Optically pumped, monolithic, all epitaxial,1.56μm vertical cavity surface emitting laser using Sb-based reflectors," *Electron. Lett.*, Vol. 33(22) pp. 1878-80(1997)

[8] L. Goldstein, C. Fortin, C. Starck, A. Plai, J. Jacquet, J. Poucart, A. Rocher, C. Poussou, "AlGaAs/GaAs metamorphic Bragg mirror for long wavelength VCSELs," *Electron. Lett.* Vol34(3) pp.268-70,1998.

[9] C. Starck, A. Plais, E. Derouin, A. Pinquier, F. Gaborit, C. Fortin. L. Goldstein, J. Boucart, P. salet, D. Carpentier, J. Jacquet, " Fabrication of 1.55μm oxidized VCSELs with top metamorphic GaAs/AlGaAs and bottom InP/InGaAsP bragg Reflectors, 998 *Proceedings of the International Conference on Indium Phosphide and Related Materials Tsukuba, Jpn.*, May 1998, pp.369-372

[10] E. A. Fitzgerald, G. P. Watson, R. E. Watson, R. E. Proano, and D. G. Ast, P. D. Kirchner, G. D. Pettit, and J. M. woodall" Nucleation mechanisms and the elimination of misfit dislocations at mismatched interfaces by reduction in growth area," *J. Appl. Phys.*, vol 65(6), pp-2220-2237,1989.

[11] S. V. Ghaisas and A. madhukar, "Kinetic aspects of growth front morphology and defect formation during moilecular-beam epitaxy growth of strained thin films," *J. Vac. Sci. Technol.* Vol. B7(2), pp.264-268, 1989.

[12] W.Q.Li, P. K. Bhattacharya, R. L. Tober, "Improved efficiency of strained InGaAs/GaAs photodiodes grown on patterned GaAs substrates by molecular beam epitaxy," *Appl. Phys. Lett.* Vol. 58, 1991.

[13] J. H. Van Der Merwe, *J. Appl. Phys.* Vol 34 pp. 117-123, 1963.

[14] J. W. Matthews, S. Mader and T. B. Light, "Accomodation of misfit across the interface between crystals of semiconductor elements or compounds", J. Appl. Phys. Vol 41, pp.3800, 1970.

[15] W. Hagen and H. Strunk, "New type of source generating misfit dislocations", *Appl. Phys. Lett*, vol17, pp.85, 1978.

[16] S. Luryi and E. Suhir, *Appl Phys. Lett*, vol 49, pp.140, 1986.

[17] S. V. Ghaisas and A. Madhukar, *J. Vac. Sci. Technol.* Vol B7, pp.264, 1989.

[18] A. Madhukar, "Growth of semiconductor heterostructures on patterned substrates: defect reduction and nanostructures," *Thin Film Solids*, vol. 231, 1993.

[19] H. Gebretsadik, K. Kamath, K. K. Linder, X. Zhang, P. K. Bhattacharya, C. Caneau, R. Bhat, "Growth of high quality GaAs/AlAs Bragg mirrors on patterned InP-based quantum well mesa structures," *Appl Phys. Lett.*,vol. 71(5), pp.581-583, 1997.

[20] M. A. Fisher, Y-Z. Huang, A. J. Dann, D. J. Eleton, M. J. Harlow, S. D. Perrin, J. Reed, I. Reid, and M. J. Adams, "Pulsed Electrical Operation of 1.5μm vertical cavity surface emitting lasers," *IEEE Photon. Electron. Lett.*, vol 7(6), pp. 608-610, 1995.

[21] T. Baba, Y. Yogo, K. Suzuki, F. Koyama, and K. Iga, "Continuous-wave GaInAsP/InP surface emitting lasers with a thermally conductive MgO/Si mirror", *Jpn. J. Appl. Phys*,vol 33, pp.1905-1909, 1994

3. WET-OXIDATION OF $In_{0.48}Al_{0.52}As$ AND $Al_xGa_{1-x}As$ FOR VCSEL APPLICATIONS

The study of the wet-oxidation of Al-bearing III-V compounds, specifically $Al_xGa_{1-x}As$ (lattice-matched to GaAs) and $In_{0.52}Al_{0.48}As$ (lattice-matched to InP) for the fabrication of high performance vertical cavity surface emitting lasers, is described in this chapter. First, the requirements for high performance of a vertical cavity surface emitting lasers and the benefits of a native oxide technology will be outlined. A brief description of the applications of the native oxide technology, as well as emerging oxide-based technologies will be presented; and the need for a native oxide technology for InP-based optoelectronic devices will be discussed.

The wet-oxidation of InAlAs for use in InP-based VCSELs was studied. In the area of $Al_xGa_{1-x}As$ oxidation, where the oxidation process as well as the oxide chemistry and microstructure are well understood [1], the recombination characteristics of minority carriers at the Al_xO_y/GaAs interface were studied.

3.1 Dielectrically Apertured VCSELs

Figure 3.1 gives schematics of several different types of VCSELs that have been investigated in recent years. The vertical structure is generally the same with an active region sandwiched between two quarter-wave stack mirrors. Epitaxial mirrors are generally used in the GaAs/AlAs system, but higher index contrast deposited dielectric

37

stacks have also been used with good success. The structures differ in how the current, the carriers in the active region, and the optical mode are confined laterally. The etched mesa in Fig. 3.1(a) provides good current confinement (with a current aperture above the active region) and excellent mode confinement but the optical losses have been shown to be high due to sidewall roughness. No lateral confinement of carriers exists in the active layer. If the mesa is etched through the active region, much of the driving current will also be lost to surface recombination current. Although the proton-implanted structure in Fig. 3.1(b), is the most popular industrial choice due to its planar configuration, it suffers from poor current confinement and its index-guiding is limited to thermal lensing. In addition, the proton-implanted structure does not provide lateral carrier confinement. Fig. 3.1(c) shows a typical buried heterostructure which provides suitable lateral optical confinement with the regrown lower index material; however it suffers from lateral current leakage. Finally, one type of dielectrically apertured VCSEL, which employs intracavity contact (also referred as a double-mesa structure) is shown in Fig. 3.1(d). The key attribute of this design is that the current is apertured and optical confinement is achieved with relatively low losses due to the lens-like action of a dielectric aperture.

As devices are scaled down, it has been found that optical losses limit the performance of the devices in some of the configurations shown in Fig. 3.1. The dependence of de-embedded internal optical loss (a figure of merit) on the type of confinement used, is shown in the graph of Fig. 3.2 for several VCSEL configurations. It is evident in Fig. 3.2 that the etched mesa structures (C,A, B, C2) have the higher losses (Note that the losses are not due to diffraction since the deeper etches C, give the highest losses). The air gap
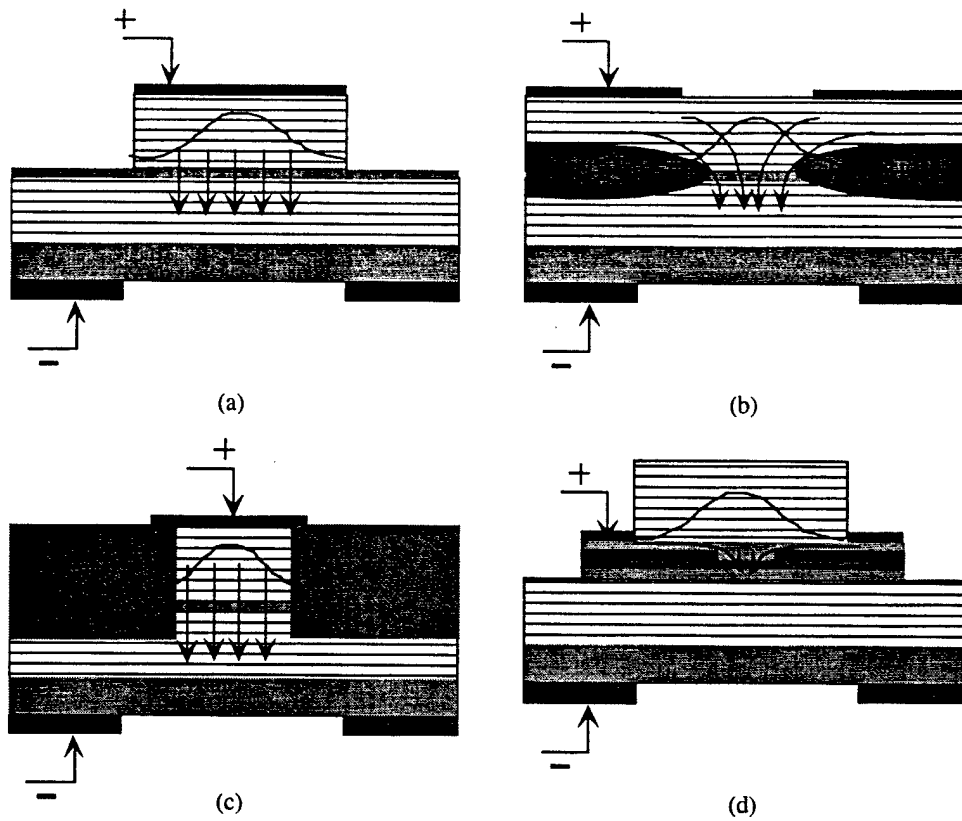
Figure 3.1:   Schematics of VCSEL structures

(D) and oxide apertures (E,G) have similar losses. The lowest losses are for thin oxide-apertured structure (F) which have the weakest optical confinement. The optical losses of dielectric-aperture VCSELs have also been predicted by considering the per-pass scattering losses in an unfolded cavity model for the VCSEL. The numerical model [2] predicts that thin and tapered apertures should have considerable lower scattering losses. The parabolically tapered aperture has the lowest possible losses, since it models an ideal lens which completely removes the effects of optical diffraction on each pass.

Therefore, the leading results use the oxidized dielectric aperture for current and optical confinement, especially for the smaller sizes where under-etched air gaps cannot be used due to their mechanical instability.
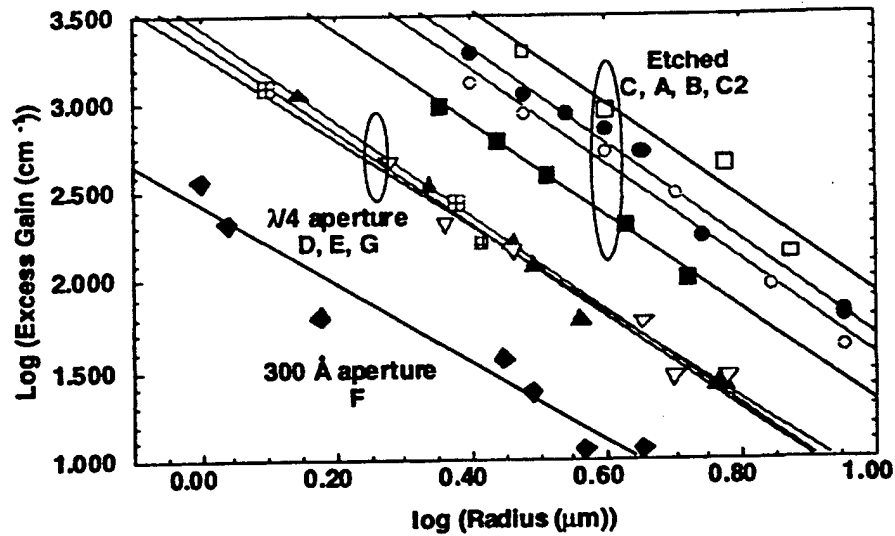
Figure 3.2:　De-embedded one-pass optical losses as a function of VCSEL radius (results compiled in article in [3])

3.2　The Wet-Oxidation Technique

The oxidation system is illustrated in Fig. 3.3. The basic principle is to expose high Al-content layers to water vapor transported in an inert gas within an elevated temperature (350°C-500°C). However establishing a stable and reproducible oxidation process requires careful control of process parameters. The set-up consists of a temperature controlled horizontal quartz tube. Water vapor is supplied to the tube by nitrogen gas passing through a flask of de-ionized water and is regulated by a flow-meter. The de-ionized water is heated to 90-95°C. A wet ambient is maintained this way for the oxidation. The stringent control of gas flow, bubbler water temperature and level, as well as furnace temperature enables a stable and reproducible oxidation process. In our experiments, the nitrogen flow and water vapor temperature were fixed for consistency.
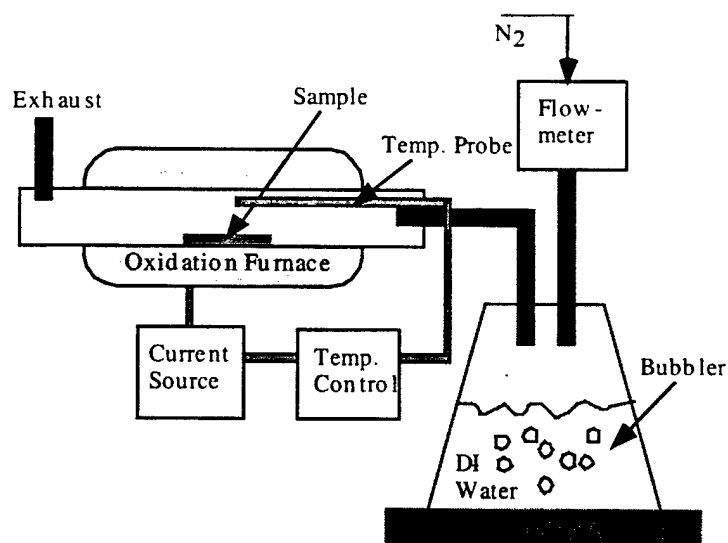
Figure 3.3:   Apparatus for reproducible wet-oxidation of AlGaAs alloys and InAlAs that employs gas flow meters, a constant temperature water bubbler and a open tube furnace.

The oxidation samples are usually composed of one or more oxidizing layers, which are grown by either molecular beam epitaxy (MBE) or metal-organic vapor phase epitaxy (MOVPE). In studying oxidation rates, mesas of various geometries and sizes are defined by reactive ion etching (RIE) followed by short wet-etch. The wet-etch insures a clean and uniform sidewall surface. The samples are typically etched immediately before the oxidation. Note that delays between etching and oxidation have not influenced the oxidation rates of AlGaAs. The oxidation furnace is allowed to equilibrate with carrier gas and flowing steam prior to each oxidation run. The samples are placed on a pre-heated platen which is inserted into the furnace. The water vapor and oxidation by-products are constantly pushed through the furnace out into the exhaust. Figure 3.4 shows a schematic of the oxidation mechanism which starts at the exposed sidewalls and proceeds inwards. Exchange of reactants is believed to take place along the interface. Although a great deal of experiments have studied the kinetics of thermal

oxidation of AlAs and high-Al AlGaAs in water vapor [4-5], few have focused on the oxidation of InAlAs lattice matched to InP.
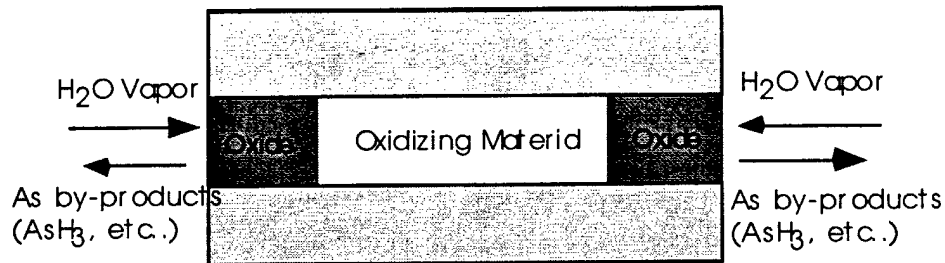
Figure 3.4:   Lateral oxidation of a buried layer.

3.3 Wet-Oxidation Technology for InP-based VCSELs

3.3.1 Background

Recent advances in the wet oxidation of $Al_xGa_{1-x}As$ layers [6] in GaAs-based heterostructures have led to the dramatic improvements in vertical cavity surface emitting laser (VCSEL) performance. Uses of this native oxide as a dielectric aperture for optical and current confinement have enabled ultra-low threshold currents [7-8] and high-output power efficiencies exceeding 50% [9] in GaAs-based VCSELs. In contrast, advances in the selective oxidation of $In_{0.52}Al_{0.48}As$ lattice-matched to InP have been slower. This native oxide has been employed in gain-guided long wavelength InAlAs-InP-InGaAsP quantum well laser diodes [10], and as a gate insulator in a InAlAs/InGaAs metal-oxide-semiconductor field effect transistor (MOSFET) [11]. Recently, a high-contrast and high reflectivity Distributed Bragg Reflector (DBR) mirror was obtained using alternating layers of InP and this oxide [12].

The low Al content in InAlAs lattice-matched to InP has resulted in very slow lateral oxidation rates as compared to the rate of oxidation of high Al content AlGaAs. To speed up this process, the oxidation must be performed at very high temperatures [13] making it difficult to selectively oxidize laser structures. So far, no study has focused on the selective oxidation of a InAlAs layer in a VCSEL heterostructure with the intent to use it as a dielectric aperture. Much of the current effort is concentrated on characterizing the wet oxidation of AlAsSb lattice-matched to InP, which has an Al mole fraction of 1.0 and which can be performed at lower temperatures [14]. With the oxidation of AlAsSb, an additional layer of residual elemental Sb forms above the oxidizing layer, deforming the surrounding layer and possibly posing limitations on its use in optoelectronic devices. The successful growth of high reflectivity defect-free GaAs/AlAs Distributed Bragg Reflector (DBR) mirrors on patterned InP-based heterostructures was demonstrated in the previous chapter. The feasibility of monolithic VCSELs utilizing such mirrors was shown through a series of measurements [15]. Another option is to fabricate a hybrid VCSEL with double-fused AlAs/GaAs mirrors [16]. In either case, the successful oxidation of InAlAs in a VCSEL structure is a key step towards the realization of low-threshold long-wavelength VCSELs. In addition, understanding the chemistry, microstructure, and processing of buried oxides converted from InAlAs is essential for the development of a robust fabrication technology.

3.3.2 Lateral Wet-Oxidation of $In_{0.52}Al_{0.48}As$

Two types of p-i-n structures were used in this experiment. The first structure was grown by molecular beam epitaxy (MBE). It consisted of a 1200Å thick InAlAs grown between two layers of InGaAs (3000Å), lattice-matched to InP. The second structure, grown by metal-organic vapor phase epitaxy (MOVPE), was a VCSEL structure with a strain-compensated InGaAsP λ–cavity active region designed for 1.55

μm operation. The structures are schematically shown in Fig. 3.5. The InAlAs layer is 1197Å thick and is directly above the InP spacer and, below a $\lambda/4$ InP layer. This structure was initially designed for the fabrication of a hybrid VCSEL structure utilizing regrown epitaxial top mirror with a multilayer dielectric stack bottom mirror.

To prepare the samples for this study, a 3000 Å layer of SiO_2, to act as a capping layer for the high temperature oxidation, was deposited by plasma-enhanced chemical vapor deposition (PEVCD). Following this deposition, the samples were patterned into 40-105 μm stripes. The oxide was dry-etched, and ridges of width 90-110 μm were formed using a saturated bromine water (SBW) solution, to expose the edges of the InAlAs layer. A section of the VCSEL structure was also patterned into mesas, in diameters ranging from 20 to 40 μm in order to investigate how the perimeter geometry of the oxidation front affects the oxidation rate. In addition, a section of the InGaAs/InAlAs structure was left uncapped and oxidized for different times. The

Structure 1   Structure 2
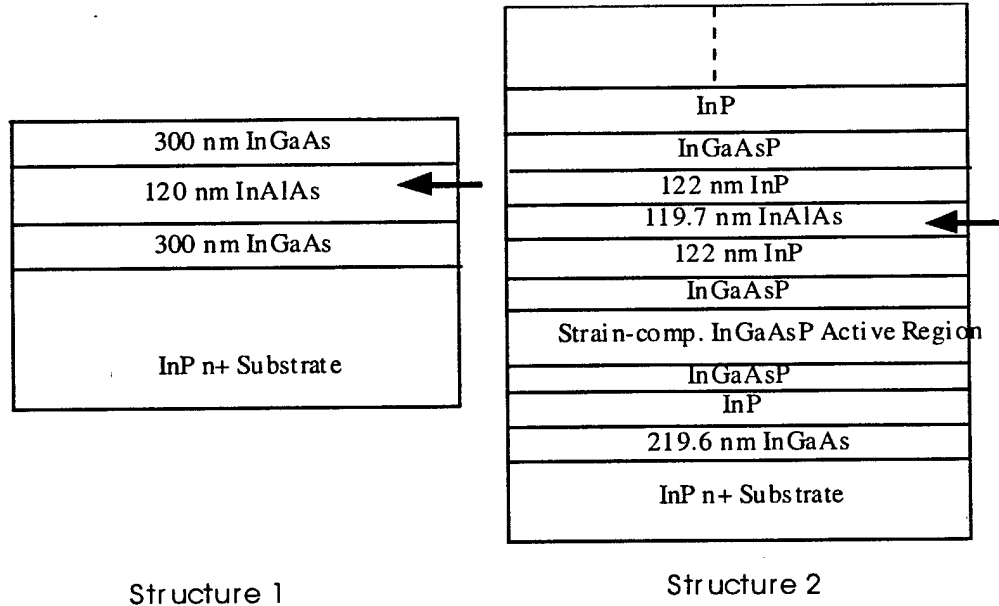
Figure 3.5: Structures used in this study: an InGaAs/InAlAs/InGaAs multilayer (structure 1) and, a VCSEL heterostructure (structure 2). The arrow points to the selectively oxidized layer.

samples were all solvent - cleaned and placed on InP substrates prior to oxidation, to avoid damaging the InP substrate [12]. The oxidation was carried out in the horizontal quartz furnace fed by 75sccm nitrogen gas passed through a water bubbler maintained at 95°C. Because the amount of water fed into the furnace is dependent on the water level in the bubbler, it is necessary to start each oxidation run with the same water level.

3.3.3 Results and Discussion

The lateral oxidation depths of the various ridge samples measured from cross-sectional scanning electron microscope (SEM) photographs, are shown in Fig. 3.6. The lateral extent of the oxide is thus measured from the edge of the mesas, averaging in both directions to minimize error. The average error in the measurement is $\pm 1 \mu m$. The depth of lateral oxidation of InAlAs in the VCSEL structure was measured as a function of time and temperature and the data are plotted and fitted (dashed line) in Fig. 3.7. The depth of oxide formation as a function of oxidation time is a best fit to a square root function which is in agreement with already published work on the wet-oxidation of
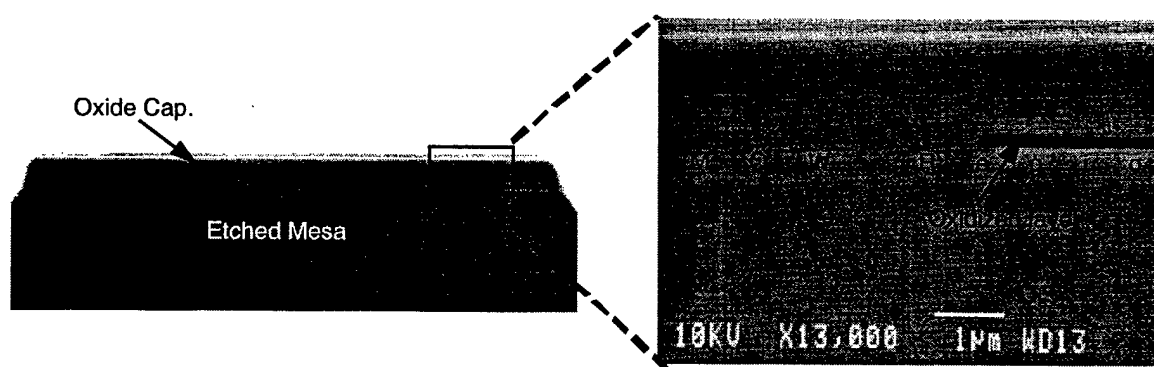
Figure 3.6:   Scanning electron micrographs (SEM) of the lateral oxidation of InAlAs in the VCSEL heterostructure, showing: (a) formation of a dielectric current aperture and (b) the oxide terminus

InAlAs. This confirms that oxidant diffusion is the rate limiting mechanism in this case. As illustrated in Fig. 3.8, it was also observed that the rate of lateral oxidation in the VCSEL structure under identical conditions is faster than that in the InGaAs/InAlAs/InGaAs structure [15]. It is our belief that the As rich layers in the InGaAs/InAlAs structure inhibit the desorption of As. At elevated temperatures, the loss of As from both layers may create an overpressure above the oxidizing region and suppress further loss.
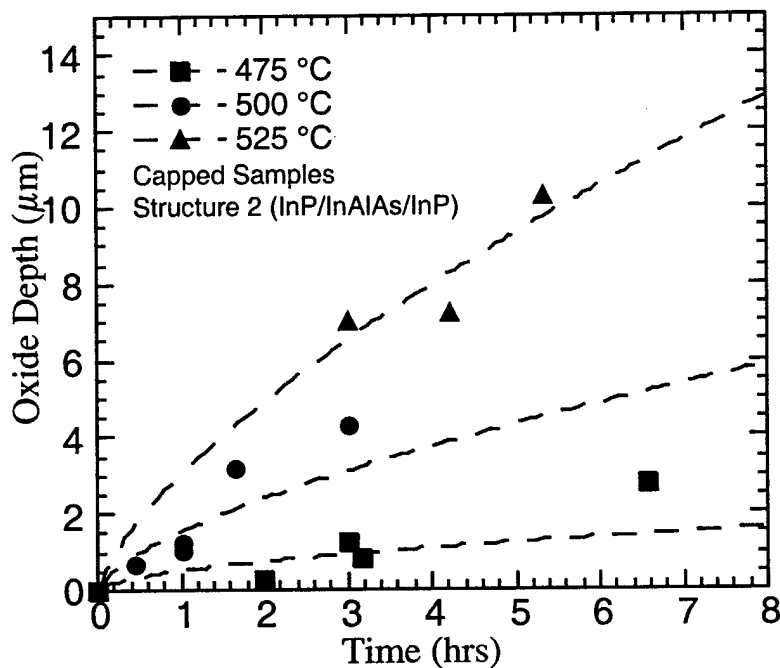
Figure 3.7: Temporal dependence of the lateral oxidation depth of InAlAs as a function of temperature. (Error ± 1μm)
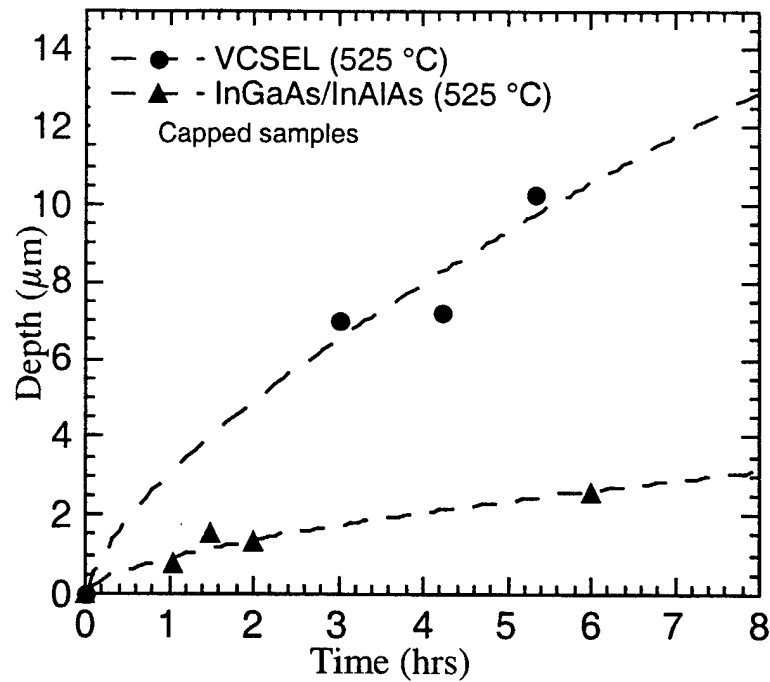
Figure 3.8: Temporal dependence of the lateral oxidation depth of InAlAs in the InGaAs/InAlAs/InGaAs (structure 1)and VCSEL (structure 2) at 525°C (Error ± 1μm)
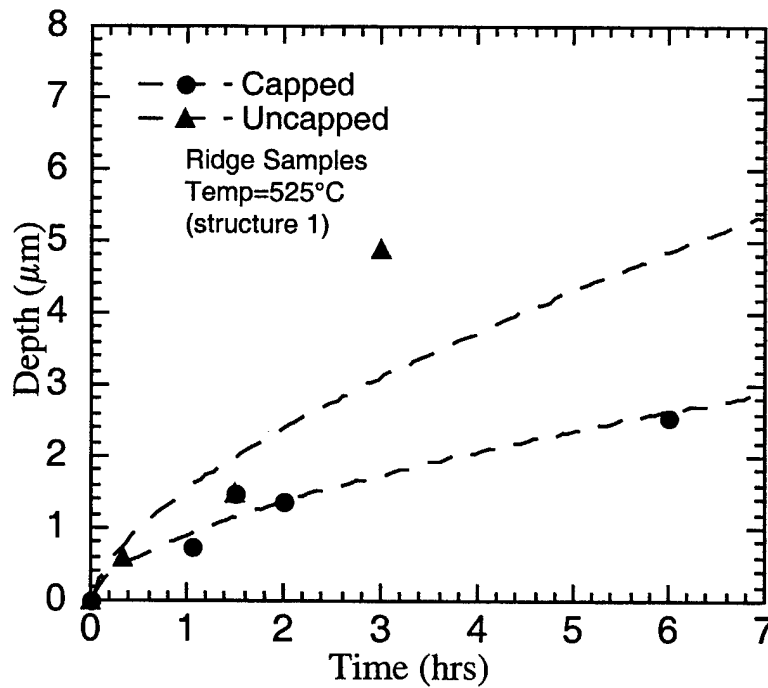
Figure 3.9: Temporal dependence of the lateral oxidation depth of InAlAs in the InGaAs/InAlAs/InGaAs with and without the use of a dielectric capping layer (Error ± 1μm)
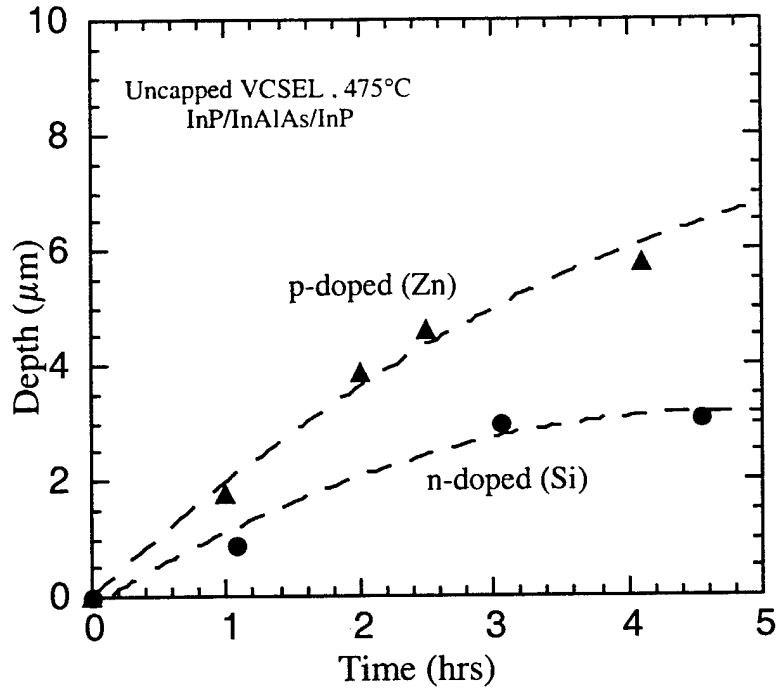
Figure 3.10:   Temporal dependence of the lateral oxidation depth of InAlAs in the InP/InAlAs/InP as a function of dopant type (Error ± 1μm)
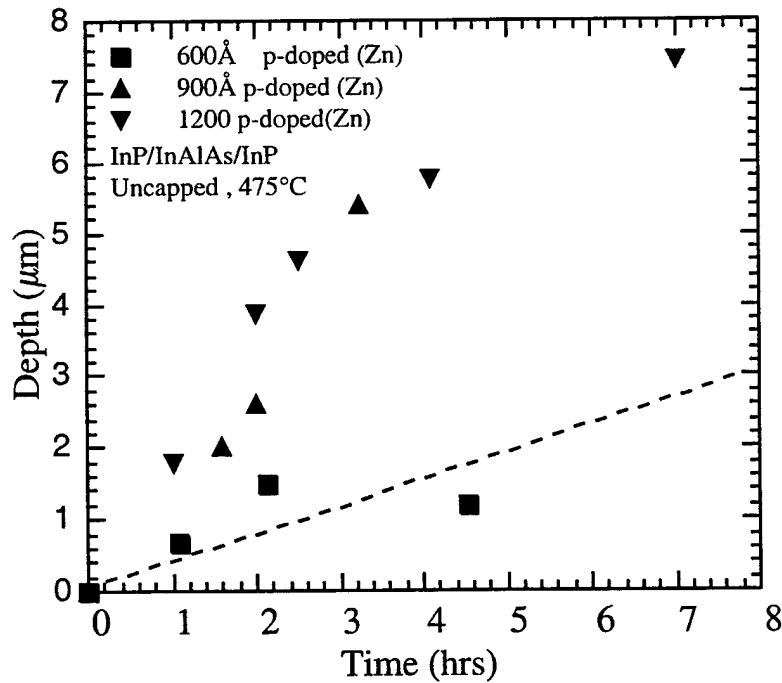
Figure 3.11:   Temporal dependence of the lateral oxidation depth of InAlAs in the InP/InAlAs/InP as a function of layer thickness (Error ± 1μm)

Figure 3.8 shows the dependence of the lateral oxidation depth on capping. In the absence of a capping layer, the oxidation was found to be faster but very non-uniform. This result is plotted in Fig. 3.9. We also showed the oxidation of n-doped InAlAs at 475°C. This is useful in designs that utilize two oxide apertures on both sides of the cavity. The n-doped layer oxidizes at half the rate of the p-doped layer. It has been shown that the thickness of the oxidized layer will also influence the oxidation rate[17]. Figure 3.11 shows the oxidation rate of InAlAs layers (surrounded by InP) with thickness varying from 600Å to 1200Å. The oxidation rate is at least 5 times slower for the 1200Å. Unlike the oxidation rate of AlGaAs which is linear (reaction-limited), the oxidation rate of InAlAs follows a square-root function and thus is oxidant-diffusion limited. For AlGaAs oxidation, specifically AlAs, the oxidation rate for 10nm thick AlAs is reduced by almost 2 orders of magnitude compared to a 100nm layer. In addition, the oxidation rate remains linear even in the thinner layers, thereby confirming that reactant transport is not the limiting factor in the process. Our results show that for thinner layers, the oxidation rate is also linear and may therefore become reaction limited. As the layer thickness gets smaller, variations of the surface energy at the oxide terminus or changes of strain with thickness will influence the oxidation rate.

3.4 Summary

The oxidation of InAlAs was characterized in the temperature range of 475°C-525°C. It was found that InAlAs oxidizes at 475°C with no damage to the substrate. The InAlAs oxidation rate was found to be almost 5 times faster when InP was used as the adjacent layer. This dependence on adjacent layer composition (resulting in a faster rate), is especially important when making oxide-confined InP-based VCSELs. The lateral oxidation of InAlAs was also characterized as a function of thickness and doping. It was

shown that the oxidation rate of InAlAs drops significantly when the layer is 600Å. This may be an indication that the oxidation mechanism becomes reaction-limited.

3.5 Recombination Characteristics of the Al $_x$O $_y$/GaAs Interface

3.5.1 Background

It has been shown that the thermal oxidation of high Al content AlGaAs layers in water vapor at elevated temperatures forms a stable oxide suitable for most optoelectronic and electronic device applications. An advantage of this wet-oxidation process is that AlGaAs layer may be selectively oxidized thereby making it possible to "bury" the oxidized layers using lateral diffusion in multilayer systems. This process has been effectively used not only in VCSELs, but also in electronic devices including, as a gate insulator in AlGaAs/GaAs field effect transistors (FETs) [18] and as a buffer insulator [19] in the on-going GaAs on insulator (GOI) effort.

Significant differences between buried oxides converted from AlGaAs alloys versus AlAs using selective wet oxidation have been reported. These oxides are now commonly used in edge-emitting lasers, optical waveguides, metal -semiconductor transistors and most importantly, in VCSELs. The oxides have been commonly formed from AlAs layers, presumably due to the ease of growth of the binary compound. However reports using AlAs layers in VCSELs described operating lifetimes of only several minutes. On the other hand, more robust VCSELs have been achieved using AlGaAs layers with 0.92<x<1.0 [20]. Still, AlAs continues to be considered the primary candidate for making oxide current apertures and high contrast DBR mirrors in VCSELs.

The electrical properties of these devices are affected by generation and recombination at the oxide/semiconductor interface. In VCSELs, it is imperative to

understand how carrier injection into the active region is altered by recombination centers at the oxide aperture. Much study has been done on the structural and mechanical stability of devices utilizing this oxide [21], and it has been determined that VCSELs with current apertures formed by the partial lateral oxidation of AlGaAs are far more robust and reliable than those using AlAs. The electronic and structural properties of the selectively oxidized AlAs/GaAs interface have also been examined in detail by other groups, using time-resolved photoluminescence measurements on multi-layer structures and transmission electron diffraction [22]. It is now common knowledge that oxides formed from $Al_xGa_{1-x}As$ (x<1) are superior in terms of oxidation isotropy, mechanical stability, and lack of strain. To date, no direct comparison of the oxidized AlAs/GaAs and $Al_xGa_{1-x}As$/GaAs (for x<1) interface recombination properties has been made. In this work, we quantitatively compared these systems by measuring the lifetime of minority carriers in the vicinity of the oxide/semiconductor interface. We also estimated the surface recombination velocities near the GaAs/ $Al_xGa_{1-x}As$ interface for x=1, 0.98 and 0.96, using the light beam induced current technique (LBIC) [23-24].

3.5.2 The Light Beam Induced Current Technique (LBIC)

3.5.2.1 Experimental Set-up

To perform the LBIC measurement, Au Schottky barriers were fabricated and a row of Schottky diodes were angle-lapped for the experiment. Light from a helium-neon laser (λ= 6328Å) was chopped and, focused by a 50X microscope objective to a spot, approximately 5 μm in diameter, onto the diode surface of the diode. Since the beam spot is approximately the same magnitude as the diffusion length expected in n-GaAs and a factor of 10 dimensional advantage is obtained by using a beveled device structure[25-

26]. Therefore, for a bevel angle of 5°, as in these cases, the thickness (vertical) of the layer changes only one-tenth of the distance (horizontal) through which the scanning spot moves. For the measurement, the diodes were reverse-biased and mounted on a 3-axis micro-manipulator. The resulting photocurrent response was amplified using a lock-in amplifier and current readings were collected at 1 μm intervals along the beveled surface, as illustrated in Fig. 3.13.

To perform this study, we have grown three layer structures as shown in Fig. 3.12 (a-c), by molecular beam epitaxy (MBE). Structure A consists of a 1μm n-GaAs ($5 \times 10^{16} cm^{-3}$) layer, followed by a 500Å AlAs and a 1μm n-GaAs, grown on n+ GaAs substrate. Structures B and C consist of 1 μm n-GaAs, followed by a 500 Å $Al_xGa_{1-x}As$ (x= 0.98 and 0.95) and a 2 μm n-GaAs layer. Note that the thickness of the oxide is kept low in order to avoid delamination of the diodes during lapping and polishing. The grown layers were mesa-etched prior to the partial lateral oxidation of the AlGaAs layer. The samples were then placed in the oxidation furnace tube at 450°C. Water vapor was supplied to the tube by flowing nitrogen at 75 sccm through water heated at 90°C. The lateral oxidation depths were determined using SEM images. Kinetics of this wet-oxidation have been previously studied and published. Gold Schottky barriers were fabricated and, a row of Schottky diodes were angle-lapped for this experiment.

1 µm n-GaAs (5 x 10^{16}cm^{-3})	2 µm n-GaAs (5 x 10^{16}cm^{-3})	2 µm n-GaAs (5 x 10^{16}cm^{-3})
0.05µm AlAs	0.05µm Al$_{0.98}$Ga$_{0.02}$As	0.05µm Al$_{0.95}$Ga$_{0.05}$As
1 µm n-GaAs (5 x 10^{16}cm^{-3})	1 µm n-GaAs (5 x 10^{16}cm^{-3})	1 µm n-GaAs (5 x 10^{16}cm^{-3})
n+ GaAs substrate	n+ GaAs substrate	n+ GaAs substrate
(a)	(b)	(c)

Figure 3.12: Schematic cross-sections of the grown structures (a) structure A, (b) structure B, and (c) structure C.

3.5.2.2 Theory

For an estimation of the recombination velocity near the semiconductor/oxide interface, the models of Watanabe et al.[24] and Hu et al.[27] were used. The total number of excess holes $\overline{\nabla p}$ in a semiconductor is given by, assuming a steady-state point excitation:

$$\overline{\nabla p} = G\tau\left\{1 - \frac{S}{1+S}\exp\left(-\frac{\xi}{L_b}\right)\right\}$$

(3.1)

where G is the excitation , ξ is the excitation depth and τ is the bulk lifetime. S is the reduced surface recombination velocity given by:

$$S = \frac{s\tau}{L_b}$$

(3.2)

where s is the surface recombination velocity and L_b is the diffusion length of the excess holes in the bulk. It is apparent that most of the excess carriers are within the distance L_b from the excitation point and thus, for excitation depths in the order of L_b, one can assume that the change in the number of excess carriers generated is due only to surface

recombination. G_{eff} incorporates this additional recombination rate introduced by recombination at the surface and is as follows:

$$G_{eff} = G\left\{1 - \frac{S}{1+S}\exp\left(-\frac{\xi}{L_b}\right)\right\} \tag{3.3}$$

The change in G_{eff} with respect to excitation depth (for shallow excitation) is given by:

$$\frac{\partial}{\partial \xi}G_{eff} = \frac{G}{L_b}\frac{S}{1+S}\exp\left(-\frac{\xi}{L_b}\right) \tag{3.4}$$

Therefore, for surface excitation, it can be shown that:
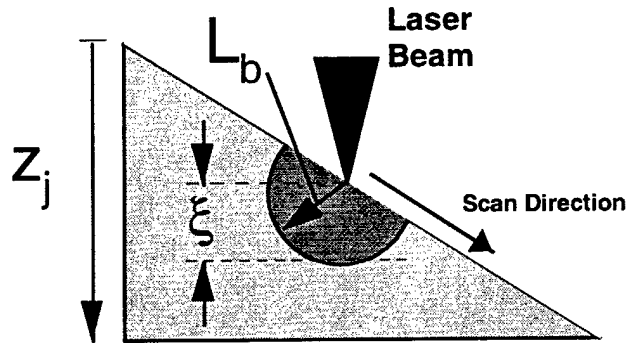
Figure 3.13:   Schematic showing device geometry

$$\frac{\partial}{\partial \xi}G_{eff}\big|_{\xi=0} = \frac{s}{D} \tag{3.5}$$

where D is the diffusion coefficient of the excess holes. The excess carriers excited by the light beam diffuse to the Schottky junction where the electron and holes are separated and a current is generated. The light beam induced current I, a function of both ξ and z_j, is proportional to the excitation strength and decays exponentially with distance from the junction:

$$I\left(\xi, z_j\right) \;\propto\; G\left\{1 - \frac{S}{1+S}\exp\left(\frac{-\xi}{L_b}\right)\right\}\exp\left(-\frac{z}{L_b}\right) \qquad (3.6)$$

where z_j is defined as the perpendicular distance from the junction. Note that the current change can therefore also be taken as:

$$\frac{\partial}{\partial \xi}I(\xi, z_j)|_{\xi=0} = \frac{s}{D} \qquad (3.7)$$

The exact current equation for the geometry of the device in Figure 3.13, although complex, has been solved and shown to satisfy equation (3.7). It is clear from the above equations that a two-dimensional profile of the surface recombination velocity can be obtained by differentiating the current with respect to excitation depth and solving for equation (3.7).

3.5.3   Results and Discussion

Laser scans for diodes with as-grown and oxidized layers are plotted in Figs. 3.14(a-c). Additional scans were performed on samples that underwent rapid thermal annealing (RTA) at 750°C for 8s. To avoid error, the diffusion length in the bulk is calculated at least a diffusion length away from the Schottky junction in structures B and C. It is in agreement with previously measured values for the bulk material [23]. A reasonable value for the diffusion coefficient was taken as 5cm^2/s. The diffusion lengths near the oxide-semiconductor interface are calculated in the regions marked with the vertical dashed lines. They are calculated and tabulated in Table II along with their corresponding recombination velocities.
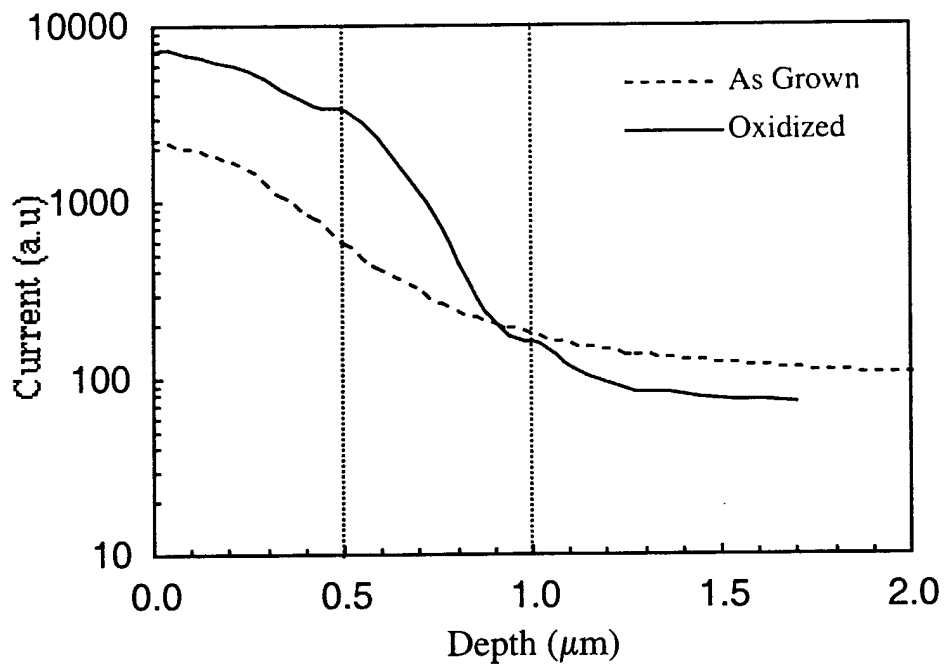
(a)
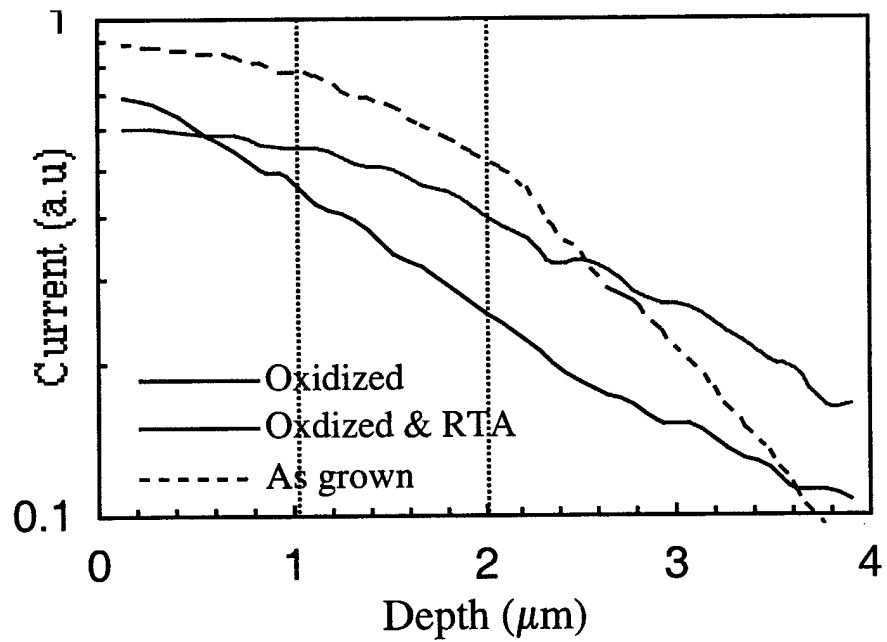
(b)
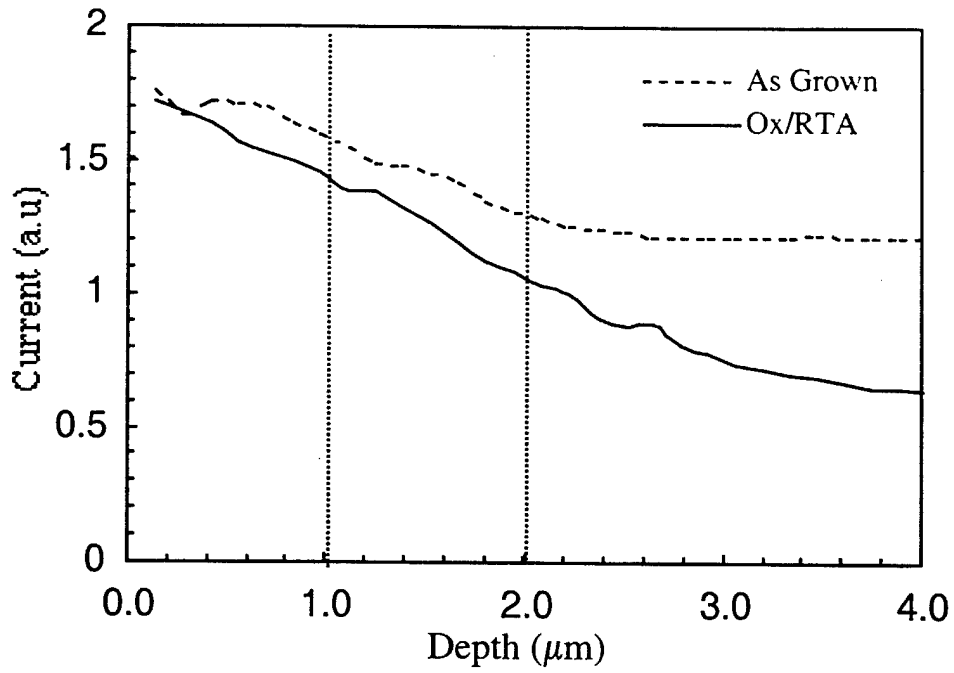
(c)

Figure 3.14:   Typical LBIC scans for (a) structure A, (b) structure B and (c) structure C.
The vertical dashed lines mark the region near the interface.

Table II: Calculated minority carriers diffusion lengths   and interface recombination velocities

Structure	L_{bulk} (μm)	L_{int} (μm)		s (cm/s)	
		Before Oxidation	After Oxidation	Before Oxidation	After Oxidation
A	--	0.36	0.16	1.38×10^5	3.13×10^5
B	3.2	2.28	1.49	1.32×10^4	1.90×10^4
		--	2.24 (RTA)		
C	4.2	3.8	2.63 (RTA)	2.19×10^4	3.36×10^4

Although there is a large interface states density at these interfaces even in the as-

grown case, the reduction in diffusion lengths of the minority carriers due to oxidation is

significantly larger for the case of oxidized AlAs. The interface recombination velocity was found to be 1.38×10^5 cm/s in that MBE-grown structure and was more than doubled after oxidation. On the other hand, the interface recombination velocities for structures B and C were found to be one order of magnitude lower and changed less after oxidation.

These results did not come as a surprise. The improvement in structural properties and minority carrier lifetimes near the interface, with the addition of a small amount of Ga to the AlAs, has been observed before. The lateral oxidation process itself proceeds more isotropically with the presence of a small amount of gallium. It is believed that some porosity and As precipitates develop at the $GaAs/Al_xO_y$ interface. In addition, stresses resulting from volume shrinkage during oxidation also appear to contribute to the formation to strain fields and/or defects near to the interface [28]. Also, published TEM images have shown the presence of small As precipitates near the interface, which could also lead to defect formation. At this point we can only speculate that the interface trap density, possibly resulting from the porosity and/or the strain fields, is reduced with the addition of gallium, resulting in a smaller interface recombination velocity.

The data correlate with previously presented work on the interface properties of the wet-oxidized AlAs. In addition to their structural and mechanical stability, multi-layer structures with laterally oxidized Al-rich $Al_xGa_{1-x}As$ exhibit improved recombination characteristics[29]. Once again, this result is especially important when studying small aperture selectively-oxidized VCSELs where leakage currents due to non-radiative recombination in and around the active region can be a limiting factor in device

performance. This result is also important for GaAs-based VCSEL arrays where the threshold current must be minimized for maximum external efficiency.

References

[1] R. D. Twesten, D. M. Follstaedt, and K. D. Choquette, "Microstructure and interface properties of laterally oxidized $Al_xGa_{1-x}As$", *Proceedings of SPIE*, Vol 3003, pp. 55-62,1997

[2] B. J. Thibeault, E. R. Hegblom, P. D. Floyd, R. Naone, Y. Akulova, and L. A. Coldren, "Reduced optical scattering loss in vertical cavity surface emitting lasers using a thin (300A) oxide aperture", *IEEE Photon. Tech. Lett.*, Vol.8, pp.593-595, 1996

[3] L. A. Coldren, E. Hegblom, E. Strzelecka, J. Ko, Y. Akulova, and B. Thibeault, "Recent advances and important issues in vertical cavity lasers", *Proceeding sof the SPIE*, Vol. 3003, pp.2-13, 1997

[4] M. Ochiai, G. E. Giudice, H. Temkin, J. W Scott and T. M. Cockerill, "Kinetics of thermal oxidation of AlAs in water vapor", *Appl. Phys. Lett.*, Vol. 68, pp.1898(1996).

[5] H. Nickel, "A detailed experimental study of the wet oxidation kinetics of $Al_xGa_{1-x}As$ layers", *J. Appl. Phys.*, Vol. 78(8), pp.5201-5203 (1995)

[6] R. S. Burton, T.E Schlesinger, "Wet thermal oxidation of $Al_xGa_{1-x}As$ compounds", *J. Appl. Phys.*, Vol. 76(9), pp.5503-5507(1994)

[7] Y. Hayashi, T. Mukaihara, N. Natori, N. Ohnoki, A. Matsutani, F. Koyama, and K. Iga, *Electron. Lett.*, Vol. 31, p.550(1995)

[8] D. L. Huffaker, J. Shin, and D. G. Deppe, *Appl. Phys. Lett.*, Vol. 65, p.97(1994)

[9] K. D. Choquette, K. L. Lear, R. P. Schneider, Jr., S. P. Kilcoyne, and K. M. Geib, *Electron. Lett.*, Vol.31, 208(1995)

[10] S. J. Caracci, M. R. Krames, and N. Holonyak, "Long wavelength native oxide defined InAlAs-InP-InGaAsP quantum well heterostructures laser diodes", *J. Appl. Phys.*, Vol. 75, 2706(1994)

[11] P.A. Grudowski, R. V. Chelakara and R. D. Dupuis, "An InAlAs/InGaAs metal-oxide semiconductor field effect transistor using the native oxide of InAlAs as a gate insulator", *Appl. Phys. Lett.*, Vol. 69, 388(1994)

[12] H. Takenouchi, T. Kagawa, Y. Ohiso, T. Tadokoro and T. Kurokawa, "Laterally oxidized InAlAs-oxide/InP Distributed Bragg reflectors", *Electron. Lett.*, Vol.32, 1671(1996)

[13] K. Uomi, S. J. Yoo, A. Scherer, R. Bhat, N. C. Andreadakis, C. E. Zah, M. A. Koza, and T. P. Lee, "Low threshold room temperature pulsed operation of 1.5µm vertical cavity surface emitting lasers with an optimized multi quantum well active layer", *IEEE Photon. Tech. Lett.*, Vol. 6, 317(1994)

[14] O. Blum, K. M.Geib, M. J. Hafich, J. F. Klem, and C. I. H. Ashby, " Wet thermal oxidation of AlAsSb lattice matched to InP for optoelectronic application", *Appl. Phys. Lett.*, Vol. 68, 3129(1996)

[15] H. Gebretsadik, K. Kamath, K. K. Linder, X. Zhang, P. Bhattacharya, C. Caneau and R. Bhat, "Growth of high-quality GaAs/AlAs Bragg mirrors on patterned InP-based quantum well mesa structures", *Appl. Phys. Lett.*, Vol. 71, 581(1997)

[16] J. J. Dudley, D. I. Babic, R,. Mirin, L. Yang, B. I. Miller, R. J. Ram, T. Reynolds, E. L. Lu, and J. E. Bowers, " Low threshold wafer fused long wavelength VCSELs", *Appl. Phys. Lett.*, Vol. 64, 1463(1994)

[17] P. Legay, P. Petit, J. P. Debray, A. Kohl, G. Patriarche, G. Leroux, M. Juhel, M. Quillet, "Wet thermal oxidation of AlInAs and AlAsSb alloys lattice-matched to InP", *Proceedings of IEEE IPRM conference*, pp.586, (1997).

[18] E. I. Chen, N. Holonyak Jr., S. A. Maranowski, "$Al_xGa_{1-x}As$-GaAs metal-oxide semiconductor field effect transistors formed by lateral water vapor oxidation of AlAs", *Appl. Phys. Lett.*, Vol. 66(20), pp. 2688-2690 (1995).

[19] P. Parikh, P. Chavarkar, U. Mishra,"First demonstration of GaAs on Insulator (GOI) technology", 1996 *Proceedings of the DRC*, pp.134 (1996)

[20] K. D. Choquette, K. L. Lear, R. P. Schneider, K. M. Geib, J. J. Fiegl, and R. Hull, " fabrication and performance of selectively oxidized vertical-cavity lasers", IEEE *Photon. Tech. Lett,* Vol. 7, p. 1237(1995)

[21] K. D. Choquette, K. M. Geib, R. Hull, H. Q. Hou, K. L. Lear, H. C. Chui, B. E. Hammons and J. A. Nevers, "Wet-oxidation of AlGaAs vs AlAs: A little gallium is good", *Proceedings of the 1996 9th Annual Meeting of IEEE lasers and Electro-optics Society*, Part 1,390(1996)

[22] Z. Liliental-Weber, M. Li, G. S. Li, C. Chang-Hasnain, and E. R. Weber, "Transmission electron microscopy of Al-rich III-V oxides", *IEEE Conf. on Semiconducting and Insulating Materials,* 159(1996)

[23] K.L. Ashley, J. R. Biard, "Optical microprobe response of GaAs Diodes", *IEEE Trans. Electron. Devices*, ED-14, 429(1967)

[24] M. Watanabe, G. Actor, and H. C. Gatos, "Determination of minority carrier lifetime and surface recombination velocity with high spatial resolution", *IEEE Trans. Electron. Devices*, ED-24, 1172(1977)

[25] D. Zook, *Appl. Phys. Lett.* Vol. 37, p.223(1980)

[26] C. H. Seager, " The determination of grain-boundary recombination rates by scanned spot excitation methods", *J. Appl. Phys.*, Vol. 53, p.5968(1982)

[27] C. Hu, C. Drowley, " Determination of diffusion length and surface recombination velocity by light excitation", *Solid-State Electronics*, Vol. 21, p.965(1978)

[28] S. Guha, F. Agahi, B. Pezeshki, J. A. Kash, D. W. Kisher, and N. A. Bojarczuk, "Microstructure of AlGaAs-oxide heterolayers formed by wet-oxidation", *Appl. Phys. Lett.,* Vol.68, p.908(1996)

[29] R. D. Twesten, D. M. Follstaedt, K. D. Choquette and R. P. Schneider, "Microstructure of laterally oxidized $Al_xGa_{1-x}As$ layers in vertical cavity lasers", *Appl. Phys. Lett.,* Vol.69, p.19(1996)

4. DESIGN AND FABRICATION OF A 1.55 μM PATTERNED VCSEL WITH LATTICE-MISMATCHED MIRROR LAYERS

4.1 Background and Motivation

In chapter 1, we have shown that it is possible to grow defect-free strained layers on patterned substrates (mesas or grooves) up to thicknesses far exceeding the critical thickness. Defect nucleation and propagation are inhibited in such growth. Based on this concept, we proposed a novel InP-based 1.55μm vertical cavity surface emitting lasers (VCSELs). Photoluminescence and TEM studies confirmed that there are no propagating defects in the MQW region of the $GaAs/Al_xGa_{1-x}As$ DBR grown on the patterned InP-based heterostructures.

Long-wavelength $(1.3-1.55\mu$m) vertical cavity surface emitting lasers (VCSEL) are the most promising low-cost light sources for local-area and long-haul fiber-based optical communication systems and optical inter-connection. Due to their low-diffraction beam output, VCSELs are best suited for wafer-scale production and testing, 2-D array fabrication and optical coupling to fibers. In addition, it has also been shown that the small modal volume and high photon density in a VCSEL can lead to high modulation bandwidth at lower currents [1]. VCSELs require highly reflective Distributed Bragg

Reflector (DBR) mirrors and low thermal resistance, presenting researchers with a tough challenge.

Despite the poor thermal properties of InP and InP-related materials and the small index difference between InP and InGaAsP, which necessitates up to 50 periods in the DBR, considerable progress has been made in the last few years in the performance of 1.3-1.55 μm VCSELs with InP-based active regions. Still, much of the research effort is concentrated on finding the appropriate material system (including hybrid systems involving a combination of dielectric and semiconductor materials) for fabricating high performance long wavelength VCSELs reliably and cost-effectively. As mentioned earlier, the most successful design is the 1.54μm VCSEL that employs two fused GaAs/AlGaAs DBR mirrors and a InP-based active region with strain–compensated InGaAsP active region, has achieved continuous-wave (CW) operation above room-temperature [2]. Further improvement in the performance of this device was observed by adding a current confining layer using the technique of selective lateral oxidation [3]-[4]. This structure overcomes the mirror problem but is still limited by the fact that the precise control of the resonant cavity wavelength is determined by the thickness of the spacer layer, the active region, and the separate DBR mirror layers. In addition, as already mentioned, this technology requires multiple substrates and is difficult to achieve on a full wafer. Also recently, the first 1300nm VCSEL (also utilizing fusion and internal photopumping) operating CW up to 80°C and compatible with commercial datacom performance requirements has been reported [5].

In this chapter, we describe the design of a new concept: an all-epitaxial 1.5μm VCSEL structure with InGaAsP/InP bottom mirror and a *defect-free* GaAs-based top

Oxidized
InAlAs
confinement
layer

5-period Al$_x$ O $_y$ /
GaAs top mirror

PtTiAu p-ohmic

InGaAsP MQW active region

InGaAsP/InP (45.5 periods)

n+ InP substrate

NiGeAu n-ohmic
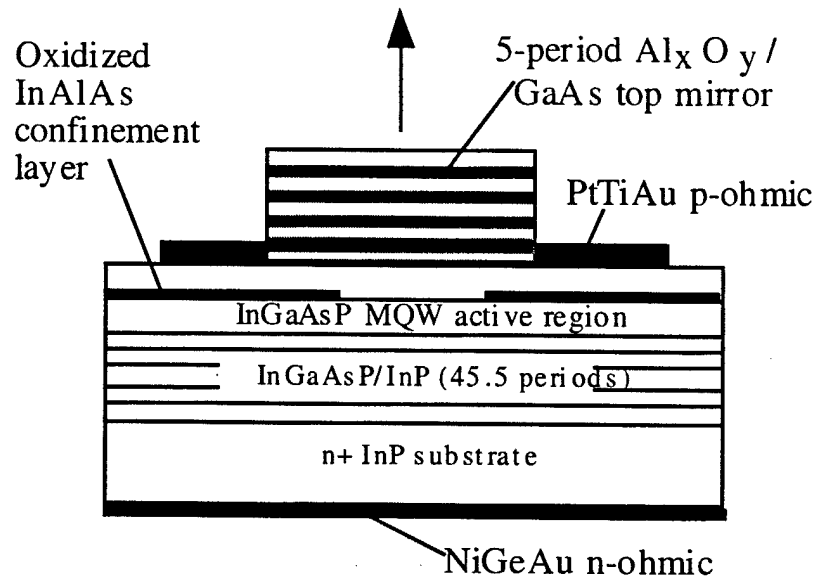
Figure 4.1:   Schematic of the fabricated top-emitting double-mesa VCSEL structure.
The p-ohmic ring and the bottom n-ohmic contacts are shown.

DBR mirror, as shown in Fig 4.1. The growth of high quality (defect-free) GaAs/AlAs mirror layers on InP-based mesa heterostructures has been previously described. In addition to the design of the high reflectivity DBR mirrors, key characteristics such as modal properties, expected wall plug efficiency and high speed modulation properties of the laser are studied. The fabrication process of the 1.55 μm VCSEL is also detailed. We proceed to show that the wet-oxidation technique is successfully applied to laterally oxidize In$_{0.52}$Al$_{48}$As for current confinement and to convert the regrown mirror to a short stack high-contrast DBR composed of oxidized AlGaAs and GaAs. We describe the process in full detail. SEM images were taken at several stages of the processing.

4.2 Design and Growth of the 1.55μm VCSEL

4.2.1 High Reflectivity Distributed Bragg Reflectors (DBR's)

The inherent advantages of a VCSEL come with a price. The significant reduction in the gain length must be compensated by a high-Q cavity, which places considerable demand on resonator mirror quality. In a VCSEL, typically two epitaxial DBRs provide longitudinal confinement of the laser field. Usually a DBR has several periods, where each period contains a high refractive index layer adjacent to a low refractive index layer. For constructive interference of the reflected waves from the interfaces, each layer should be λ/4 thick, where λ is the wavelength of the light in the respective layers. The choice of materials for the layers is based on maximizing index contrast, and maintaining transparency of the laser light. The layers may also be made of dielectric materials, where a larger difference in refractive index between layers is possible [for example, n(ZnSe)-n(CaF$_2$)= 1.7] so that one obtains high reflectivity with a small number of DBR periods. For our device, we have used InP/InGaAsP bottom mirrors because they can be epitaxially grown and enable current injection through the mirrors. Substrate removal and back-hole etching for deposition of dielectric mirrors may also be avoided, thereby reducing process complexity (difficulties in handling wafer) which may ultimately increase overall yield per wafer through a more robust process. However, the index difference (Δn=0.3) is very small and more than 40 periods are needed to achieve a high reflectivity, posing serious challenges in the epitaxial growth.

It is difficult to form a VCSEL with InGaAsP/ InP reflector on both sides because the total cavity thickness will exceed 10μm and processing using standard photolithography is almost impossible. Therefore, much as we have done, most research has concentrated on developing a top mirror technology [6]-[7].

4.2.1.a   Growth of the InP/InGaAsP Bottom Mirror and Cavity

The laser is first grown by metal-organic vapor phase epitaxy (MOVPE) up to the active region. 45.5 periods of n-doped InGaAsP ($5 \times 10^{18} \text{cm}^{-3}$)/InP DBR mirror were initially grown on an n+ InP substrate. This extra step was only necessary since the MOVPE reactor used at *Corning Inc.*, was not equipped with *in-situ* reflectometry equipment. After checking the reflectivity, the extra pair was etched off and the active region containing 8 InGaAsP strain-compensated multiple quantum wells was grown. The thickness of the barriers and wells are 70Å (0.9% tensile strain) and 80Å (1% compressive strain) respectively. Two undoped InGaAsP spacer layers sandwich the multi-quantum well region and form the λ-cavity. Quarter-wave layers (including the InAlAs current confinement layer) are grown on top of the cavity which consist of a p-doped $\lambda/4$ InP, ($2 \times 10^{18} \text{cm}^{-3}$), a p-doped $\lambda/4$ InAlAs layer, another $\lambda/4$ InP layer and a $\lambda/4$ highly doped InGaAsP ($\lambda=1.2 \mu$m) contact layer as shown in the layer structure of Fig. 4.2.

Table III: Refractive Indices of layers in VCSEL structure

Layer	Index of Refraction ($\lambda=1.58\mu$m)
i-InGaAsP ($\lambda=1.2\mu$m)	3.317
n-InGaAsP ($\lambda=1.45\mu$m)	3.417
InAlAs	3.3
InP	3.07
Al$_x$O$_y$	1.56
InGaAsP (barrier)	3.4
InGaAsP(QW)	3.5
GaAs (undoped)	3.38

The growths of all the InP-based heterostructure were done on 2 inch wafer in a vertical MOVPE reactor . Background pressure was kept at 150 mTorr. Trimethyl-indium (TMI), triethyl-gallium (TEG), arsine (AsH$_3$) and phosphine (PH$_3$) were the source materials. Dimethyl Zinc (DMZ) and hydrogen sulphide (H$_2$S) were the dopant sources. The growth temperature was fixed at 650°C, except for growth of InAlAs, when it was raised to 675°C. The doping levels of both p- and n-type layers are given in Fig. 4.2. Prior to growing the whole cavity structure, both the MQW and the DBR were separately grown and calibrated. The cavity was designed for emission at λ= 1.58μm. The refractive indices used for the design are given in Table III.
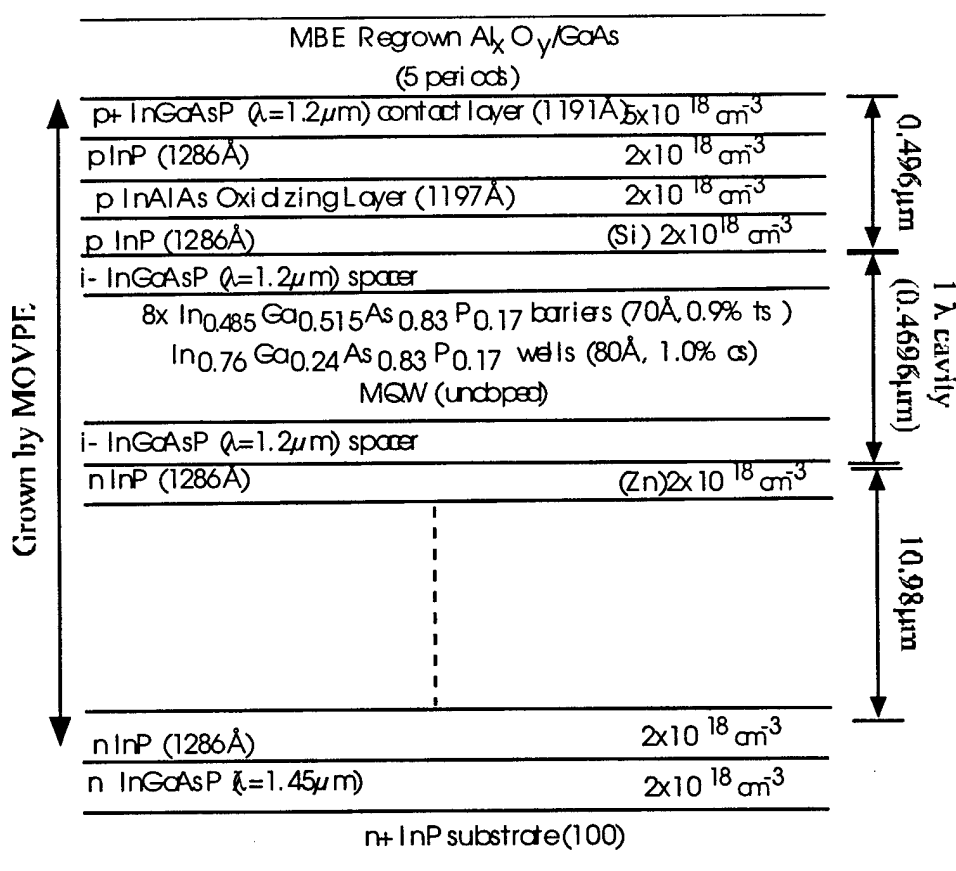
Figure 4.2:   Detailed layer structure of the 1.55μm VCSEL with regrown GaAs-based top DBR mirror
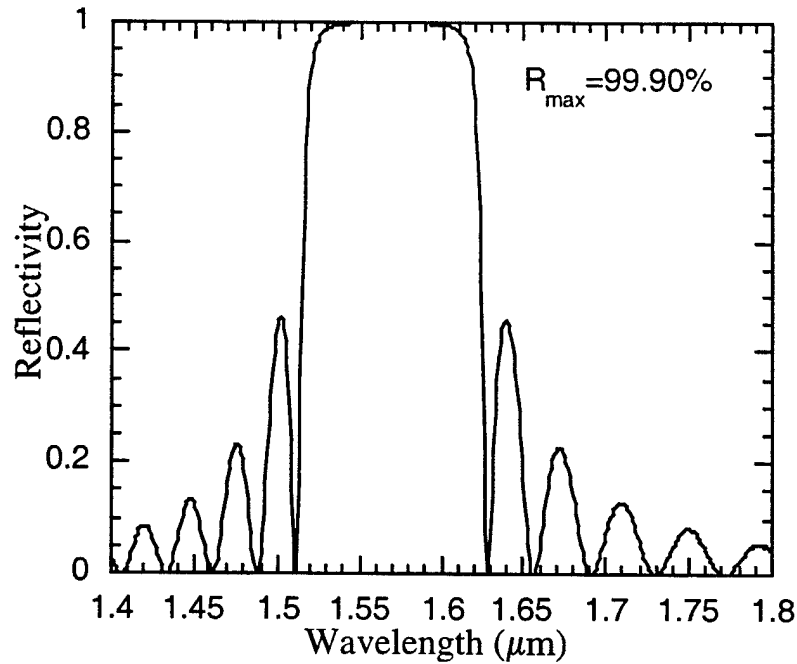
Figure 4.3:   Reflectivity of 45 pairs InGaAsP/InP layers. The maximum reflectivity is 99.9%.

Figure 4.4 shows the relative reflectivity spectrum of the InP-based VCSEL structure grown by MOVPE. Although the reflectivity is not absolute, valuable information regarding the resonant wavelength can be obtained. The valley wavelength, in Fig. 4.4(b), corresponds to the resonant cavity wavelength, $\lambda=1.58\mu$m. Typically, one can also estimate the thickness deviation from such a spectrum; and may in fact, adjust or correct the growth times for the next run (ie. adjust the tuned wavelength). Figure 4.5 is the room-temperature photoluminescence data obtained on a test VCSEL structure. The observed multiple peaks are due to non-uniformity in the well and/or barrier widths. The broad peak centered corresponding to bulk InGaAsP ($\lambda=1.45\mu$m) originates in the bottom mirror layers.
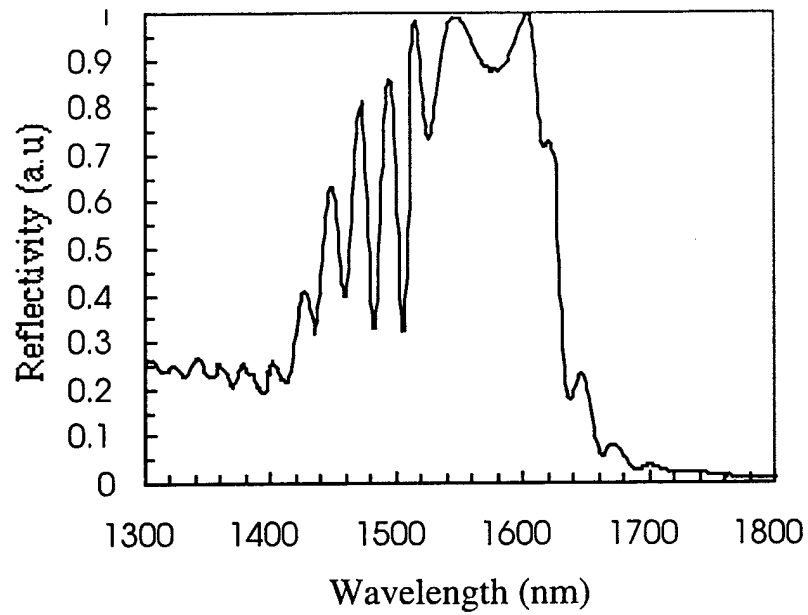
(a)
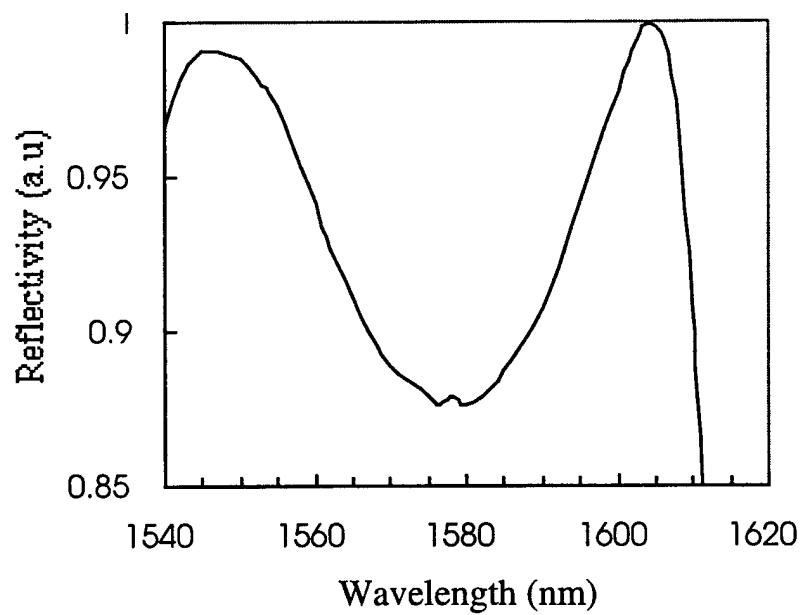
(b)

Figure 4.4: Reflection spectra of the as-grown InP-based vertical cavity structure (a) whole spectrum after growth of cavity prior to regrowth and, (b) its magnification around the valley minimum.
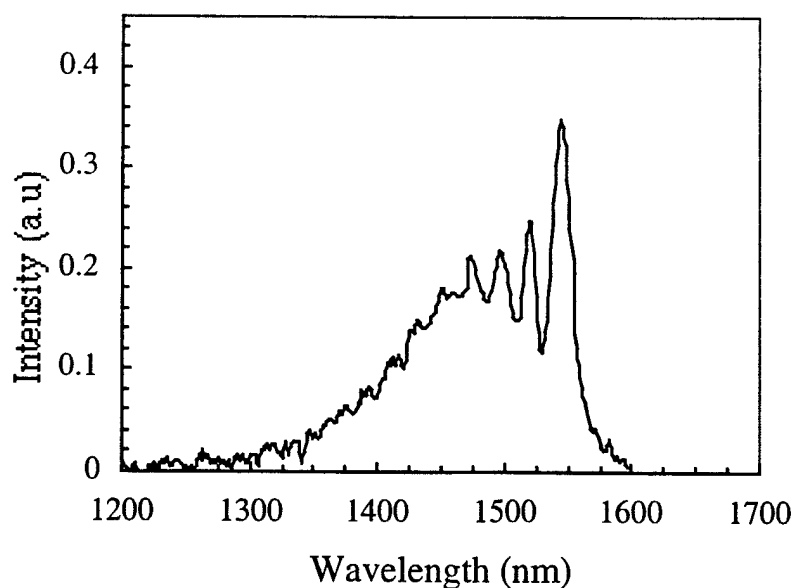
Figure 4.5:   Room-temperature photoluminescence measurement of the MQW active region (after removing contact layers)

4.2.1.b   High Contrast Al$_x$O$_y$/GaAs Mirror

In the previous chapter, we showed that we can directly grow GaAs/AlGaAs DBRs on patterned InP-based heterostructures. Since the index of refraction of this system is also small, the same stringent requirements on layer precision ($\pm$1%) apply to ensure cavity resonance is aligned with the gain peak. Usually, single-wafer, in-situ thickness measurement techniques are used to achieve the high degree of control needed to reproducibly grow such structures. In contrast to semiconductor DBR's, dielectric mirrors have a high index difference and a wide stop band, and high reflectivity using relatively few layers. As a result, the alignment of the cavity resonance with the gain peak is not as difficult as in semiconductor DBRs [8].

It has also been suggested that the use of high contrast mirrors on both sides of the active region in a VCSEL can reduce the fundamental lateral spread of the cavity mode and can result in very low threshold currents [9]. We take advantage of these favorable

properties of each type of DBR by directly growing a 5 pair undoped AlGaAs/GaAs DBR, with a much higher index contrast and a wide stop band.

A short-stack Al_xO_y (2394Å)/GaAs (1169Å) 5 pair DBR mirror is designed to complete the laser structure, as was illustrated in Fig. 4.2. $Al_xGa_{1-x}As$ layers with $x \geq 0.95$ can be used for the formation of the Al_xO_y. We assumed an oxide layer shrinkage of 5%. The mirror has a peak reflectivity of 99.87% (calculated) and a stop band >500nm. The output power of the device will be limited by the very high reflectivity of these mirrors but the original intent of this study was to demonstrate that the top reflectivity obtained using a native oxide based DBR was sufficient to obtain lasing in such a vertical cavity. The dependence of the external efficiency (or the ouput power) on mirror reflectivity is investigated in a later section.
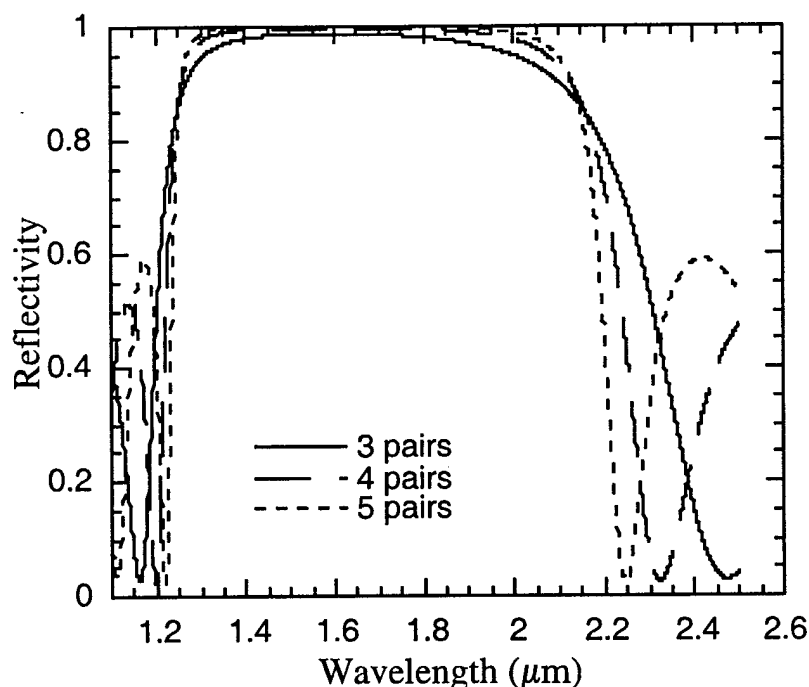
Figure 4.6:   Simulated reflectivity of 3,4,5 pairs Al_xO_y/GaAs DBR pairs.
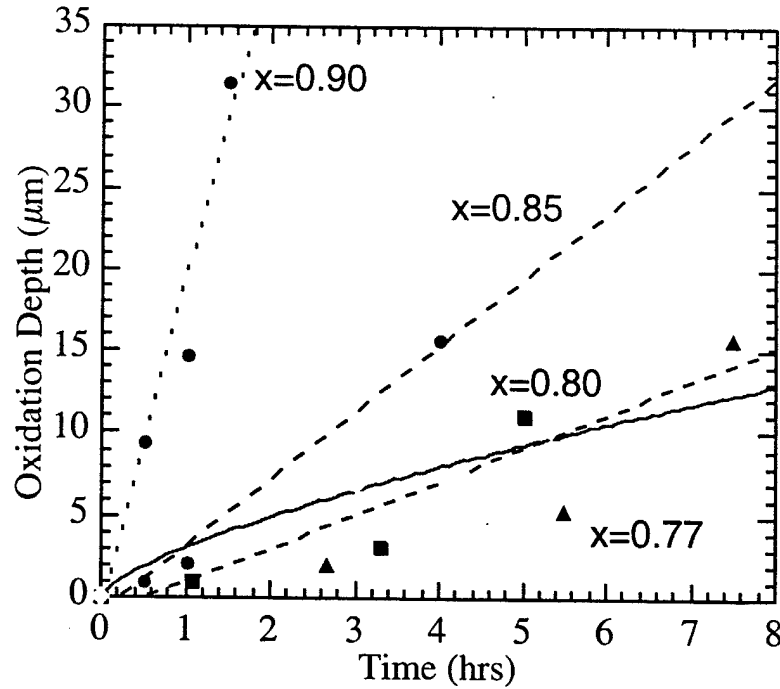
Figure 4.7:   Temporal dependence of the lateral oxidation depth of AlGaAs (x>0.77). at 475°C. The solid line shows the corresponding dependence for $In_{0.48}Al_{0.52}As$.

We also investigated the possibility of simultaneously oxidizing both the InAlAs lattice-matched to InP and the regrown mirror. We found that $Al_xGa_{1-x}As$ layers with Al composition as low as 0.77 can be selectively oxidized at 475°C, under the conditions described in Chapter 3. Although the rate of oxidation quickly became similar to the rates obtained for InAlAs, the index of refraction of the oxide (as measured by a He-Ne ellipsometer) varied between 1.5 and 1.6, for x < 0.9. In addition, the mirror quality was degraded. This is possibly due to the increased residual gallium in the oxidized layers. Figure 4.7 shows the oxidation rates obtained for varying AlGaAs compositions.

4.2.2 Emission Wavelength Control

In addition to ease of growth, one of the advantages of using a high contrast $Al_xO_y/GaAs$ top mirror is that the alignment of the cavity resonance with the gain peak is

not as difficult as in semiconductor DBR's. Due to the short cavity length in surface emitting lasers, only one mode is allowed within the cavity, which must satisfy the round trip phase relation given by [10]:

$$\Phi_{top} + \frac{2L_c n}{\lambda} \cdot 2\pi + \Phi_{bot} = m \cdot 2\pi \qquad (4.1)$$

where ϕ_{top} and ϕ_{bot} are the phases of mirror reflections associated with the top and bottom mirror, respectively. L_c and n are the actual mirror separation distance and the average refractive index, m is an integer and λ is the resonant-cavity wavelength. When the mirrors are made of epitaxial semiconductors that have a low Δn, the resonant wavelength considerably depends on ϕ_{top} and ϕ_{bot}, due to the large penetration depths of the optical wave into the mirrors. Figure 4.8 shows the resonant cavity wavelength
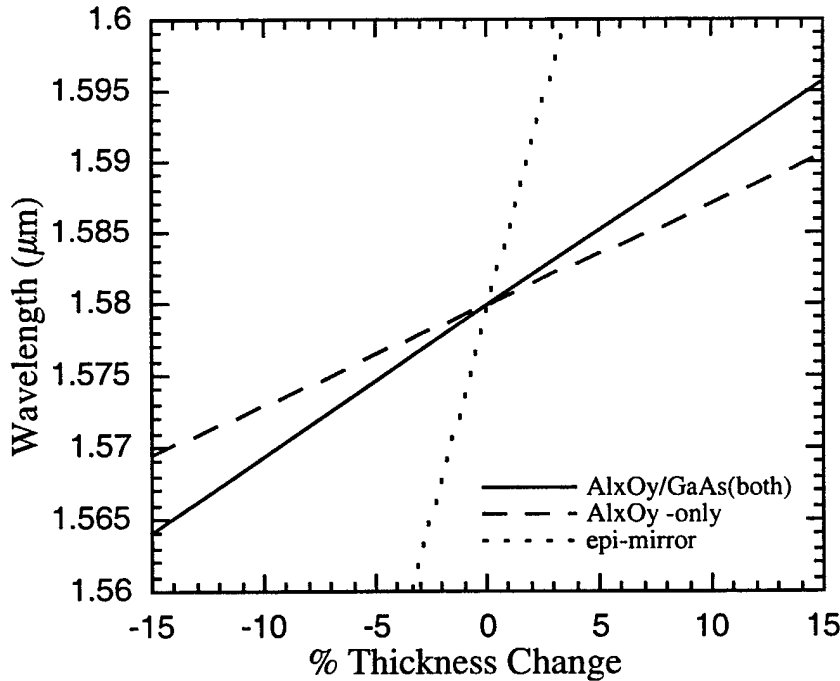
Figure 4.8:   Dependence of resonant cavity wavelength on the % thickness fluctuation of an epitaxial AlAs/GaAs (growth-related) , Al$_x$O$_y$ /GaAs mirror (growth-related) and Al$_x$O$_y$/GaAs (due to possible oxide shrinkage). The bottom mirror reflectivity remains constant in all three cases.

(which we denote as λ_e) dependence on mirror thickness fluctuations. The reflectivity of the InGaAsP/InP bottom mirror is kept fixed in this calculation and the top mirror layers are made to fluctuate. For a top mirror using 25 pairs of AlAs/GaAs (for example, as in the fused mirror case), a shift in DBR thickness of 1% can cause the emission wavelength to shift by 5nm; whereas in the AlxOy/GaAs case, the same shift only results in a shift of ~1nm. In addition, sometimes the shrinkage of the oxide layers may vary by as much $\pm$ 5% if oxidation conditions are not controlled carefully. The effect of the deviations of the oxide thickness from expected value are also plotted. Again, the effect is small.

4.3   Expected Device Performance

4.3.1   Modal Properties of 1.55μm VCSEL

The modal properties of the VCSEL are studied using the vectorial transform matrix approach as formulated in [11], where mode coupling and radiation field effects are ignored. This approximation is accurate for this structure. A plot of the refractive index profile of the cavity region, together with the longitudinal electric field standing wave calculated by this method, are shown in Figure 4.9. The longitudinal optical confinement factor is calculated from the field distribution and is found to be 4.5% in our device.

The oxidized VCSEL's radial field intensity profiles for the fundamental hybrid mode (HE_{11}) and higher order modes (TE_{01} andTE_{02}) are also calculated using the same transform matrix approach [12]. Figure 4.10 shows these for the case of a 12 μm radius oxide –confined VCSEL.
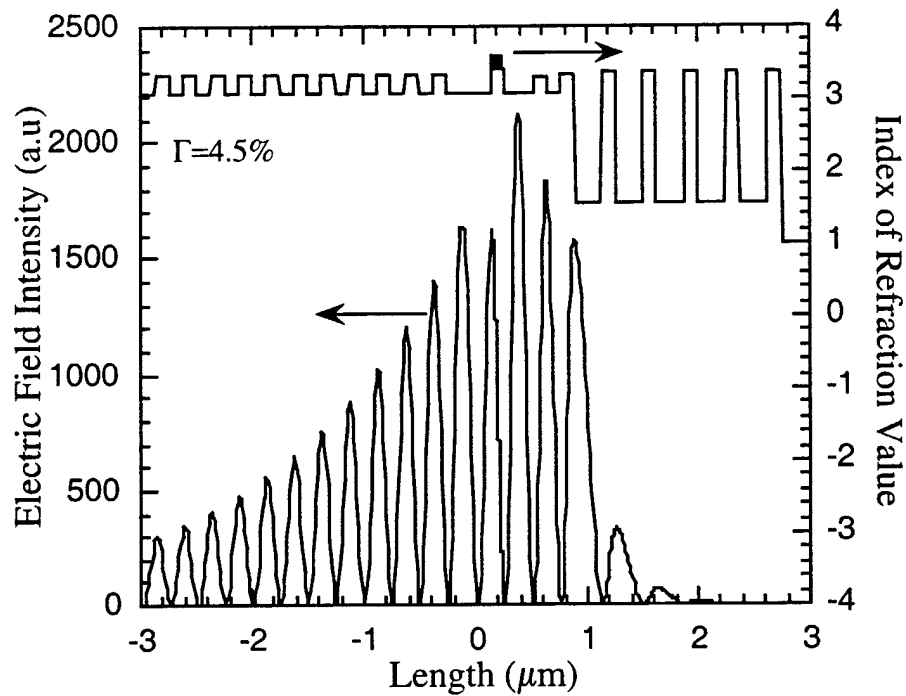
Figure 4.9: Refractive index profile of the multi-layers of the VCSEL structure, around the cavity showing the standing wave intensity variation relative to the multi-quantum wells and DBRs
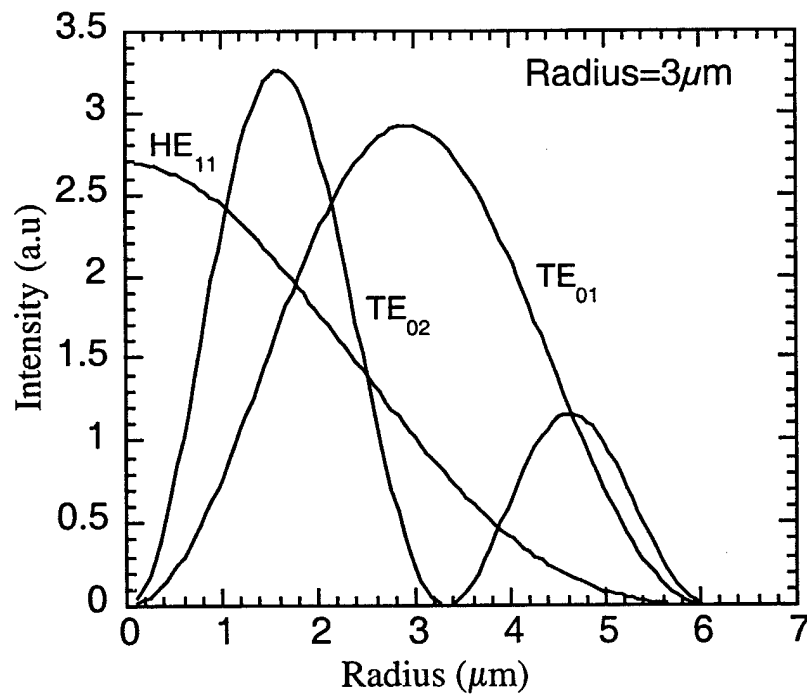
Figure 4.10: Transverse mode profile for a VCSEL (radius=6μm) for (a) HE_{11}, (b)TE_{01}, and (c)TE_{02}

4.3.1.a   External Efficiency and Optimal Reflectivity

One of the figures of merit of a VCSEL is the external (or wall-plug) efficiency, which represents the total conversion of electrical to optical power. VCSELs, more commonly InP-based VCSELs with InP/InGaAsP bottom DBR mirrors, are usually dominated by a fairly large series resistance R_s and thus the external efficiency η_{ext} is defined by:

$$\eta_{ext} = \frac{P_0}{I^2 R_s + I V_{jcn}} \tag{4.2}$$

where I is the laser current, V_{jcn} is the voltage drop across the laser junction and P_o is the laser output given by the expression :

$$P_o = A \frac{h\nu}{q} (J - J_{th}) \eta_e \bigg/ \left[1 + \frac{\alpha L}{\ln(1/R)} \right] \tag{4.3}$$

where J and J_{th} are the supplied and threshold current densities respectively, A is the laser junction area, η_e is the electrical confinement factor, α is the scattering loss per unit length and L is the effective length of the laser cavity. As described in [13], a useful technique in designing laser performance for practical applications is to determine a variable parameter x, at the optimum operating point above threshold defined by $I = I_{th} + x I_{th}$ which allows the current to be expressed in terms of the threshold value. Substituting for both and I and V_{jcn} (a function of I) in η_{ext} leads to the expression of η_{ext} given in terms of x and I_{th} below:

$$\eta_{ext} = \frac{\left(h\nu/q \right) x \eta_e \bigg/ \left[1 + \alpha L/\ln(1/R) \right]}{(1+x)^2 I_{th} R_s + (1+x) V_j} \tag{4.4}$$

An expression for x, obtained by taking the derivative of Eqn. (4.2) is extracted and is given by:

$$x_m = \sqrt{1 + \frac{V_j}{I_{th}R_s}} \qquad (4.5)$$

It is then possible to determine an optimal η_{ext}, while varying the parameter x, assuming the threshold has been established by the overall reflectivity. It should be noted that the threshold is not assumed to be independent of other parameters such as temperature; indeed I can be expressed in terms of x and a value of I_{th} that includes self-heating and a leakage current component [13]. For our device, $V_{jcn}= 1.3$V, $I_{th}=6$mA so that the optimum operating point is around 2 times threshold. The result is shown in Figure 4.11 for our device, using the parameters shown in Table IV. It shows the external
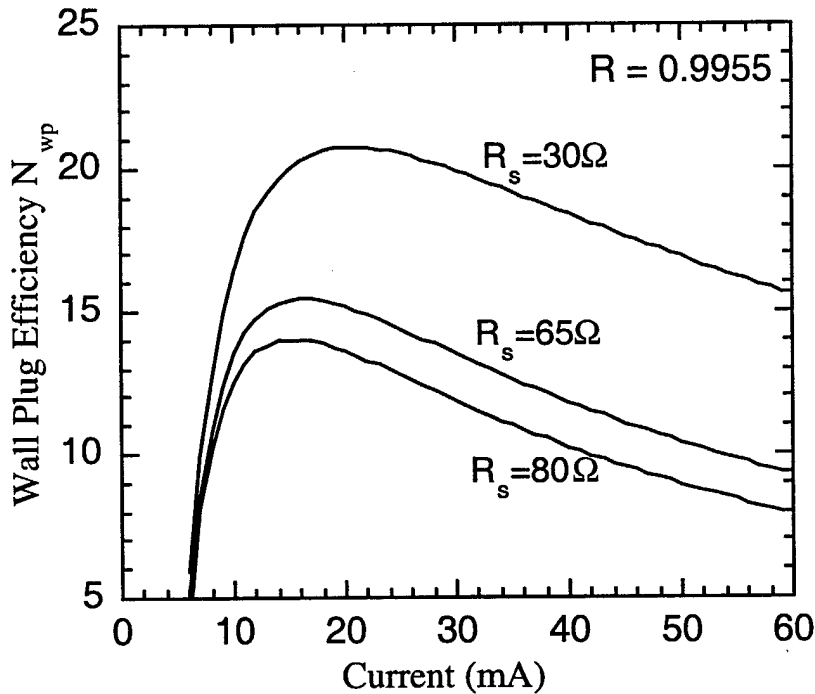
Figure 4.11: Calculated variation of the external efficiency η_{ext} for the strain-compensated MQW VCSEL using the series resistance as a parameter. (The laser parameters are shown in Table IV)

Table IV: VCSEL model parameters used in the theoretical calculations

Parameter	Value
Γ_m	0.045
α	30 cm^{-1}
d	12 μm
L_z	80Å
τ_o	0.5ns
τ_s	15ps
τ_{cp}	200ps
dg_m/dN	10^{-15} cm^2
η_e	0.8
I_{th}	6 mA
V_{jcn}	1.3V
τ_p	3ps
$\overline{B}_i$	10^{-10}m ^{6}/s^{-1}
D_{np}	1.65×10^{73} m^{-4} J^{-2}
λ	1.58μm
L	0.47μm

efficiency for several different values of the resistance R_s. From a design point of view, this helps us determine the operating conditions that would maximize η_{ext}, while also predicting the external efficiency if the series resistance of the device is pre-determined. This also shows that the series resistance should be minimized if maximum wall plug efficiency is to be achieved.

Another issue of concern in designing our laser for optimal operation is determining the overall mirror reflectivity. This amounts to choosing the reflectivity of the top-emitting mirror, R_t (the reflectivity of the bottom mirror remains fixed and can be assumed to be unity). From Eqn. (4.2), it can be seen that the output power will be maximized at almost the same current as η_{ext}, provided that the variation in V_{jcn} is small.
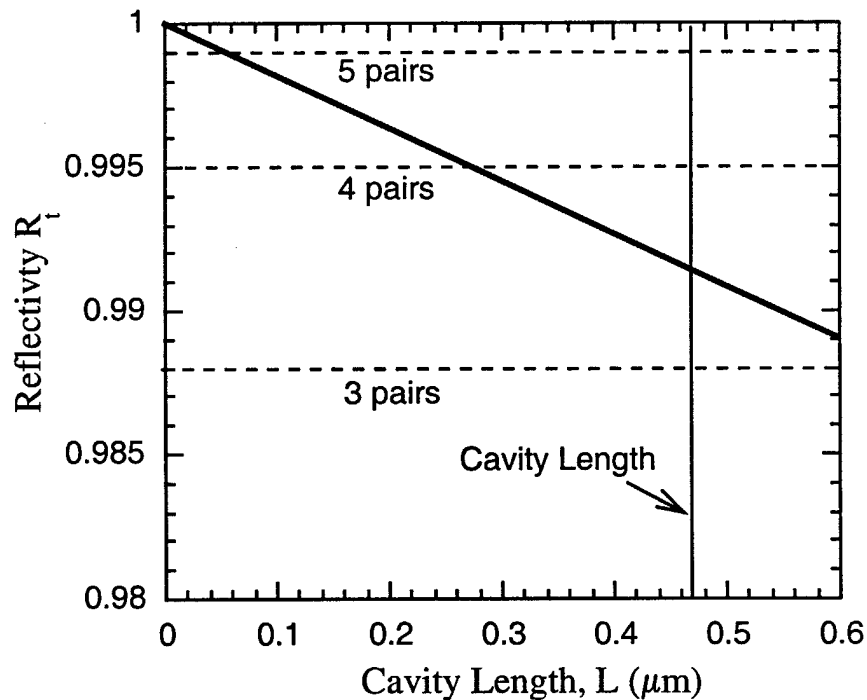
Figure 4.12: Variation of the optimum reflectivity R_t for the strain-compensated MQW VCSEL as a function of cavity length. (The horizontal dashed lines correspond to the reflectivities of the Al_xO_y/GaAs DBR for the case of 3, 4 and 5 pairs)

The analytical model derived in [13], again provides a simple and expeditious prediction of the value R_t , for use in laser design and such that one is interested in its variation over the practical range of which is typically $0.988 < R_t < 0.999$. Over this range, the following simplified equation can be used:

$$1 - R_t = \left[\left(\frac{\alpha}{\sqrt{K * \left[(1 + 1 / x)(1 - \eta_e) + 1 / x \right]}} \right)^{2/3} - \alpha \right] L \quad (4.6)$$

in which K* is defined by:

$$K* = \frac{L_z^2 v_g}{2 \Gamma_m h D_{np} k T \overline{B}_i} \quad (4.7)$$

where L_z is the quantum well width, Γ_m is the optical confinement factor for m wells, D_{np} is the densities of states product for the quantum well, h is the Planck constant, k is the Boltzmann constant and $\overline{B}_i$ is the modified Einstein coefficient for the mode. In this way R_t may be determined for a chosen design of cavity length. In Fig. 4.12, R_t is plotted as a function of cavity length. The dashed lines represent the fixed reflectivities for 3, 4 and 5 pairs of Al_xO_y/GaAs ($\Delta n=1.8$), which constrain the design. The optimal reflectivity can be used to calculate the differential quantum efficiency η_d , the threshold current density J_{th} and the electrical confinement factor η_e. Ideally, the maximum external efficiency can be expected for this reflectivity.

4.3.1.b   Modulation Properties

For application in high-speed optical communication systems, VCSELs should be characterized by a large modulation bandwidth. Due to their small cavity size, VCSELs are expected to have high relaxation oscillation frequencies (ROF) and modulation

bandwidths. In fact, the modulation bandwidth of VCSELs is limited by the relaxation oscillation frequency under direct modulation. In fact, the relaxation oscillation frequency is a function of many parameters including the photon density, differential gain, and optical confinement factor. With an oxide aperture and a high reflectivity Al_xO_y/GaAs DBR, the VCSEL were characterized by an enhanced modulation response.

The small signal modulation response of the VCSEL was studied using a simple rate equations model with the inclusion of carrier transport to calculate the influence of device dimension [14]. The current model (neglecting self-heating and spatial hole burning) is:

$$\frac{dS(t)}{dt} = [Go + \Delta Go]S(t) + R_{sp} \tag{4.8}$$

$$\frac{dN}{dt} = \frac{M}{\tau_s} - \frac{N}{\tau_o} - \frac{N}{\tau_{cp}} - S(t)v_g\Gamma g_m|\psi|^2 \tag{4.9}$$

$$\frac{dM}{dt} = \frac{J}{qL_wN_w} - \frac{M}{\tau_o} - \frac{M}{\tau_s} - \frac{N}{\tau_{cp}} \tag{4.10}$$

where,

$$Go = v_g[\Gamma g_{mo}(z) - \alpha_o] \tag{4.11}$$

$$\Delta Go = v_g \int_{cavity} (\Delta N\frac{\partial}{\partial N} + \Delta S\frac{\partial}{\partial N})[g_m(z) - \alpha(z,V)]\psi^2(z)dz \tag{4.12}$$

where, S is the photon density, N is the carrier concentration in the active region, M is the carrier concentration in the spacer layer, Γ is the optical confinement factor, R_{sp} is the spontaneous emission rate, g_m is the gain, α_o is the loss in the cavity, ψ normalized field distribution, τ_o is the carrier lifetime, τ_s is the carrier transport time in the spacer layer, τ_{cp} is the thermionic capture/emission time, L is the QW width, and N_w is the number of quantum wells.

(a)

J/J_{th} (Normalized Current Density)
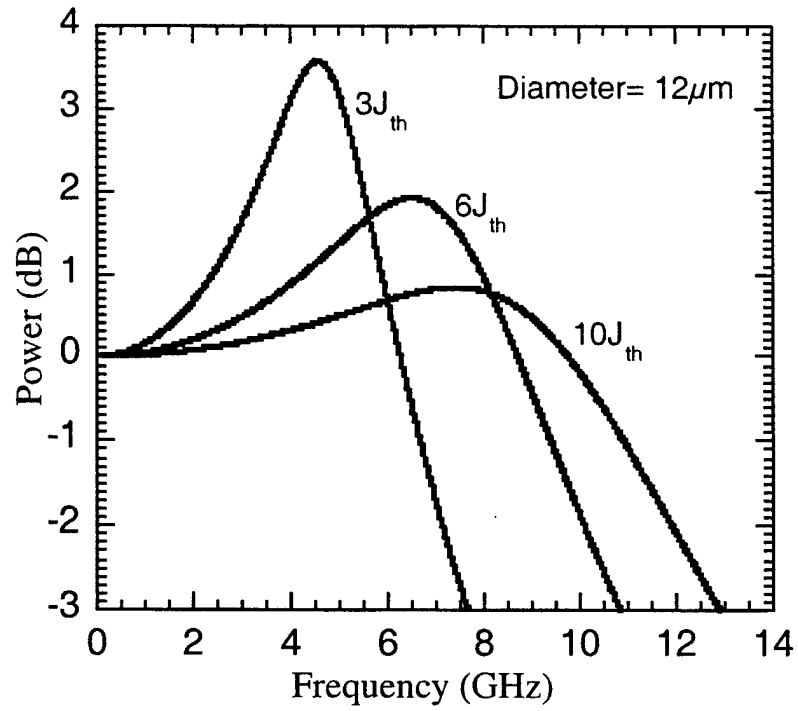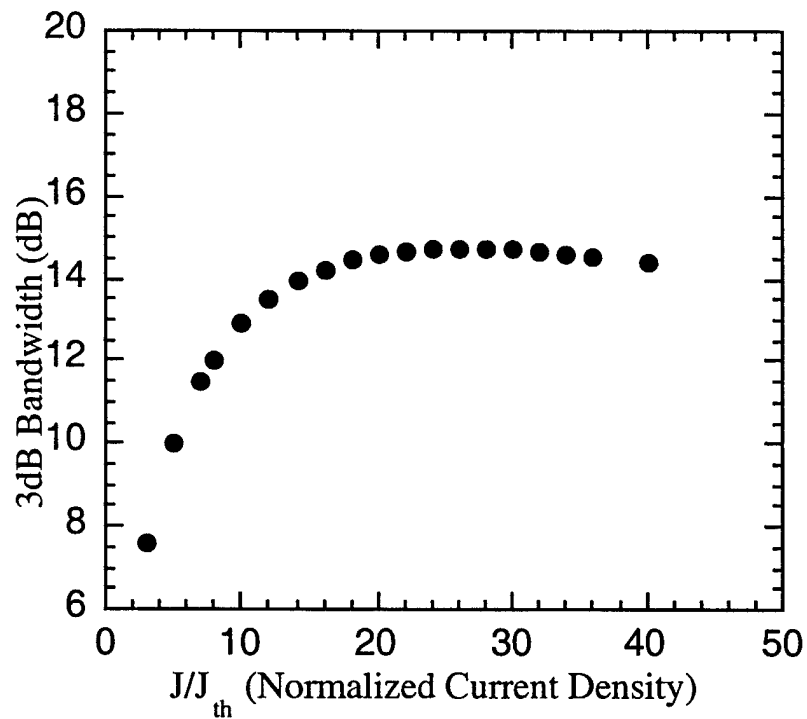
Figure 4.13:   (a) Calculated modulation response as a function of current density, and
(b) 3dB bandwidth as a function of current density for the VCSEL (diameter=12μm)

The rate equations were solved for the designed structure and geometry. The parameters used in these calculations are also shown in Table IV. The frequency response of a 12μmVCSEL is shown in Figure 4.13(a), for different current densities. The 3dB bandwidth of the device at $10J_{th}$ is 13GHz. Figure 4.13(b)shows the 3dB bandwidth as a function of current density. As can be seen from it, the modulation bandwidth of the device is saturated when the current density approaches $20J_{th}$. This is mainly due to the gain saturation effect. From these calculations, it is obvious that the patterned VCSEL can achieve modulation bandwidths as high as 14GHz. However, the modulation bandwidth of VCSELs can also be limited by the RC time constant of the device and the optical confinement factor. The high series resistance is largely due to the length of the bottom mirror and may be minimized, by using intra-cavity contacts in the next generation devices. In such cases, the high series resistance associated with the bottom InGaAsP/InP mirror stack will be eliminated. Additionally, optimizing the cavity design of the VCSEL would increase the optical confinement factor, while optimizing the layout would minimize the parasitic capacitance.

4.4 Fabrication of Lasers

The results from the lateral oxidation rate of InAlAs in the VCSEL heterostructure (InP/InAlAs/InP) as a function of thickness were used for the laser structure [15]. The selective oxidation of InAlAs was characterized for this structure and was found to be controllable within 2 μm. Directly above the laser cavity in the laser heterostructure, is the $In_{0.52}Al_{0.48}As$ layer which is partially oxidized to form a dielectric aperture. The fabrication sequence is illustrated in Fig. 4.14. The sample is patterned into 2μm high and 20-40μm diameter mesas in saturated bromine water (SBW).

InP-based
heterostructure

Oxidized InAlAs
layer

1. Pattern InP-based heterostructure into mesas of varying diameter

2. Selectively oxidize the exposed InAlAs layer (set current aperture size)

GaAs-based
Regrown mirror

Etched mirror

3. AlGaAs-GaAs DBR mirror regrowth (short stack)

4. Etch regrown DBR mirror by reactive ion etching (RIE) and wet chemical etching. Oxidize mirror.

p-ohmic ring   Polyimide

Interconnect

n-ohmic

5. Evaporate/lift-off p-ohmic ring and planarize with photosensitive polyimide.

6. Evaporate/lift-off interconnect metal. Evaporate n-ohmic contact. Anneal.

Figure 4.14:   Fabrication sequence of the 1.55μm VCSEL process

The patterned substrate was then oxidized in the furnace at 475°C in a water vapor ambient. The exposed InAlAs layer is laterally oxidized to form the desired active area size. The laser heterostructures were selectively oxidized at 475°C for 6 hrs. Lateral oxidation depths of 7-8 μm are repeatedly obtained, producing apertures ranging from 4μm- 26μm. In this laser structure, no oxide capping layer was necessary. Figure 4.15 shows the extent of the oxidation.

The sample was then removed from the furnace and was immediately prepared for
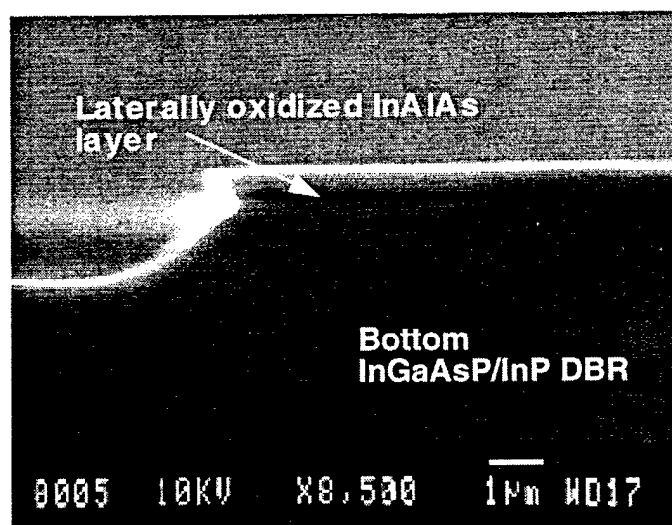
Figure 4.15:   SEM micrograph of etched mesa heterostructure showing selectively oxidized InAlAs layer and, no damage to substrate.

regrowth. The 500Å InP capping layer was etched following this selective oxidation, prior to regrowth. The patterned substrate undergoes cleaning with an oxygen plasma, followed by a wet-etch in a HCl:$H_2$0 (1:10) solution and a short HF/H_2O (1:5) dip prior to loading. A short 5 period stack of $Al_{0.95}Ga_{0.04}As$/GaAs bilayers, calibrated for the lasing wavelength, are grown on the patterned substrate by MBE.

The regrown mirror was etched by reactive ion etching (RIE) into a double-mesa structure, using a combination of BCl_3 and Ar gases, followed by a 30 sec etch in H_3PO_4:H_2O_2:H_2O (1:1:10) to remove any RIE damage. The top DBR mirror was selectively oxidized at 425°C for 45 minutes using the same wet-oxidation technique. A stable high contrast Al_xO_y/GaAs was formed using $Al_{0.95}Ga_{0.05}As$. No delamination of the top DBR, nor the InAlAs-oxide occurred. Figure 4.16 shows a SEM micrograph of the double mesa structure prior to metallization.
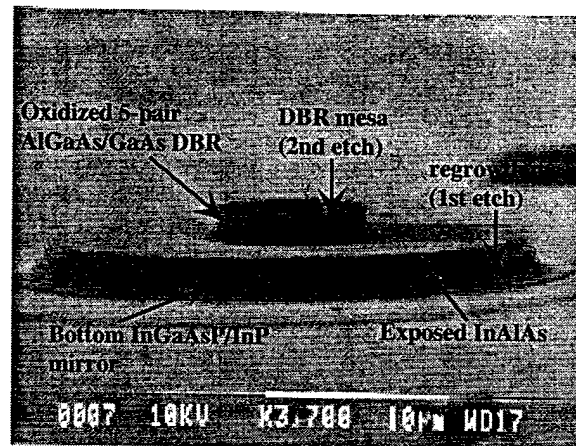
Figure 4.16: SEM micrograph showing the double mesa structure, after the final mirror oxidation step.

The p-contact ring (Pt/Ti/Pt/Au) was made on top of the first mesa, using standard photolithography and lift-off techniques. Planarization, using polyimide, enabled deposition of an interconnect metal. Au/Ge/Ni n-contact was evaporated on the backside of the substrate, which was subsequently annealed at 400°C for 40 seconds. Figure 4.17 shows the device prior to and after planarization. It is clear that this process is planar and can potentially be integrated with optoelectronic circuits (OEIC).
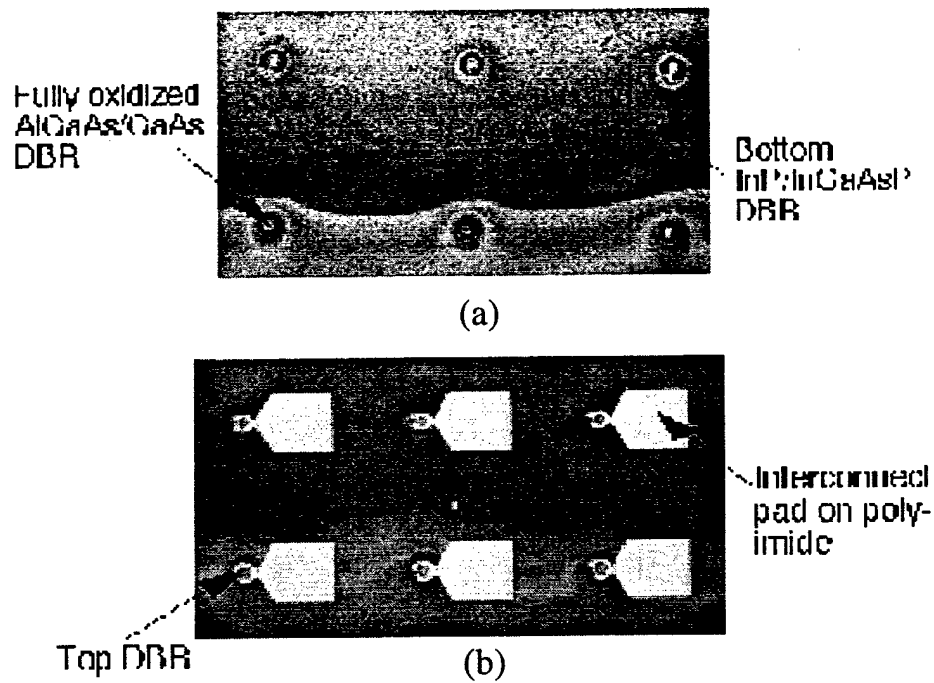
Figure 4.17: Optical micrographs of the devices (a) prior to metallization and planarization and, (b) after polyimide planarization and metallization, ready for probing.

References

[1] T. G. Dziura, Y. J. Yang, R. Fernandez, T. Bardin, and S. C. Wang, "High speed modulation characteristics of Helium implanted Zinc-diffused vertical cavity surface emitting lasers", *IEEE Photon. Technol. Lett.*, Vol. 5, pp. 1270-1292, 1993.

[2] D. I. Babic, K. Streubel, R. P. Mirin, N. M. Margalit, J. E. Bowers, E. L. Hu, D. E. Mars, L. Yang, and K. Carey, "Room-temperature continuous-wave operation of a 1.54 μm vertical-cavity lasers", *IEEE Photon. Technol. Lett.*, Vol. 7, pp. 1225-1227, 1995.

[3] N. M. Margalit, J. Piprek, S. Zhang, D. I. Babic, K. Streubel, R. P. Mirin, J. R. Wesselmann, J. E. Bowers, E. L. Hu, "64°C continuous-wave operation of a 1.5μm vertical cavity laser", *IEEE J. of Sel. Topics in Quantum Electron.*, Vol. 3, pp. 359-365, 1997.

[4] J. M. Dallesasse, N. Holonyak, Jr., A. R. Sugg, T. A. Richard, and N. El-Zein, "Hydrolyzation oxidation of $Al_xGa_{1-x}As$-AlAs-GaAs quantum well heterostructures and superlattices," *Appl. Phys. Lett.*, Vol. 57, 2844(1990).

[5] V. Jayaraman, J.C. Geske, M. H. MacDougal, F. H. Peters, T. D. Lowes, T. T. Char, "Uniform threshold current, continuous-wave, singlemode 1300 nm vertical cavity lasers from 0 to 70 degree C", *Electron. Lett.*, Vol. 34(14) pp.1405-1407, 1998.

[6] Y. Qian, Z. H. Zhu, Y. H. Lo, D. L. Huffaker, D. G. Deppe, H. Q. Hou, B. E. Hammons, W. Lin, and Y. K. Tu, " Low-threshold proton implanted 1.3μm vertical cavity surface emitting lasers with dielectric and wafer bonded GaAs-AlAs Bragg Mirrors", *IEEE Photon. Technol. Lett.*, Vol. 9(7), July 1997.

[7] S. Uchiyama, N. Yokouchi, T. Ninomiya, "Continuous-wave operation up to 36 degree C of 1.3μm GaInAsP-InP vertical-cavity surface-emitting lasers", *IEEE Photon. Technol.* Lett. Vol.9, pp.141(1997).

[8] C. Amano, Y. Itoh, Y. Ohiso, H. Takenouchi, T. Tadokoro, T. Kurokawa, "MOVPE growth of InGaAsP/InP based vertical cavity structures for wafer-fused VCSELs", *J. of Crystal Growth*, Vol.187, pp.35-41(1998)

[9] G. M. Yang, M. H. MacDougal, and P. D. Dapkus," Ultralow threshold current vertical cavity surface emitting lasers obtained with selective oxidation", *Electron. Lett.*, Vol. 31, pp.886-888, (1995)

[10] T. E. Sale, *Vertical Cavity Surface Emitting Lasers*, Research Studies Press, Somerset, England, p.36

[11] D. Burak and R. Binder,"Cold cavity eigen modes f VCSELs", *IEEE J. of Quantum Electron.*, Vol. 33,1997

[12] R. Michalzik, K. Ebeling, "Generalized BV diagrams for higher order transverse modes in planar vertical cavity laser diodes",*IEEE J. of Quantum Elect.*, Vol. 31, pp.1371(1995)

[13] G. W. Taylor and Q. Yang, "Optimization of the operating point of a vertical cavity surface emitting laser," *IEEE J. of Quantum Electron.*, Vol. 32(8)pp. 1441-1449, 1996

[14] S. F. Yu, W. N. Wong, P. Shum and E. H. Li, "Theoretical analysis of modulation response and second-order harmonic distortion in vertical cavity surface emitting lasers", *IEEE J. of Quantum Electron.*, Vol. 32(12)pp. 2139-2147, 1996

[15] H. Gebretsadik, K. K. Kamath, W-D. Zhou, P. K. Bhattacharya, C. Caneau, R. Bhat, "Lateral oxidation of InAlAs for in InP-based heterostructures for long wavelength vertical cavity surface emitting laser applications", *Appl. Phys. Lett.*, Vol. 72, pp.135-137, 1997

5. CHARACTERISTICS OF PATTERNED 1.55μM VCSELS

5.1 Introduction

In the previous chapter, a patterned 1.55μm VCSEL was designed and fabricated. The fabrication process successfully integrated the two oxidation steps. InAlAs (lattice-matched to InP) was selectively oxidized to form current apertures (with diameter sizes varying from 6-26μm) below the regrown mirror. This feature is expected to lead to reduced loss by eliminating lateral current spreading in the doped layers above the MQW region, and increasing uniformity of carrier injection below the oxidized mirror. In addition, scattering loss at the rough pillar sidewall (which is prevalent in the double-fused VCSEL design) is also eliminated. The mirror was also selectively oxidized to form a high contrast wide-band Al$_x$O$_y$/GaAs DBR mirror.

For this device, an InP/InGaAsP bottom mirror was chosen. This allows for full wafer fabrication and testing. We believe that sufficient reflectivity can be obtained from the bottom mirror for lasing; but there will be a performance penalty arising from the ohmic heating and poor thermal dissipation in the bottom mirror. Under pulsed bias conditions, these will have a weak effect. Therefore one can expect good room temperature performance from such a device provided matching of the cavity resonance to the material gain peak is good.

5.2 DC Characteristics

5.2.1 Experimental procedure

The basic experimental set-ups for measurement of an L-I curve under (a) DC and (b) pulsed conditions are described below. For DC measurements, the device is driven with a laser diode current driver (for example, the Newport 505 laser Diode Driver) and the light is coupled into a Ge photodiode. The two types of detectors used for our measurements are the integrated Newport Power Meter (Model 1815C) with the infra-red head, or the EG&G Hudsons Electronics Germanium photodiode, PN R03M-HS. The integrated power meter, once calibrated to the wavelength of the light being measured, reads power directly. The germanium photodiode is reverse-biased to about 10V, and the photodiode current as a function of laser current is measured. The current is converted to output light through the manufacturer's specified conversion efficiency.

The devices are also measured in pulsed mode, to reduce the effect of carrier heating. The device is driven with a pulsed source (HP8112A Pulse Generator), and the current to the device is measured with an AC current probe (Tektronix P6022). The light is measured with a photodiode reverse-biased in a high speed configuration. Typically, the pulse on cycle is $1\mu s$ every $100\mu s$ (1% duty cycle).

To acquire data, the boxcar averager (Stanford Research Systems SRS250) is used to average the current pulse and light pulse amplitude over the on-cycle time. The pulse output trigger of the pulse generator is used as the general trigger for the boxcar averager, and the average window is adjusted with the width and delay knobs. The scale is adjusted to give convenient numbers with the scale knob, and the output is nulled when the current is disabled with the output offset knob. For automated measurement, a labview program is used to step the voltage source up in voltage and collect the measured

current and the light output for each voltage step. The GPIB cable is connected to the back of the boxcar averager. The lasers' spectra were characterized using an optical spectrum analyzer (HP-OSA-70952B). The light from the laser is coupled directly to a fiber, which in turn is connected to the OSA. A labview program is used to collect data directly from the OSA as well.

5.2.2 Laser Performance

5.2.2.a   Light-current characteristics

Fig. 5.1(a) shows the room-temperature pulsed light-current and voltage-current characteristics for a 26μm device. In this case, the devices were tested with no heat sinking other than contact with the metal stage. Threshold currents as low as 12 mA were observed for 26μm devices. The emission wavelength was 1.542μm as can be seen from the optical spectrum as shown in Fig. 5.1(b), obtained from a 10μm device with an optical spectrum analyzer. The linewidth of the laser is 0.6nm. The slight broadening in the laser linewidth is due to self heating during the pulse (frequency chirping).

Large variations in threshold current, were observed due to thickness non-uniformities (varying growth rates) across the wafer causing the peak reflectivity wavelength of the bottom reflector band to vary. This is especially true with MOVPE grown wafers [1]. We mentioned previously that because the emission wavelength is determined by the peak reflectivity wavelength of the bottom InP-based mirror, accurate control of DBR layer thickness (within ±1% of designed value), as well as precise adjustment of the strain-compensated InGaAsP MQW PL peak , are required. Hence, for

this run, the best devices occurred when the MQW emission wavelength and the cavity resonance wavelength were closest to one another.

To overcome the possible gain/cavity detuning (or gain offset), other devices were mounted on a Peltier stage and characterized at lower temperatures. Additional L-I curves were collected from devices of varying size. Figure 5.2(a) shows the threshold current dependence on diameter for devices tested under a pulsed bias source at 15°C. The dashed line is a linear fit of the measured data. With smaller oxidized apertures, sub-milliamp threshold currents can be achieved. The LI-characteristic of an 8μm device, as a function of temperature is shown in Figure 5.2(b). The observed temperature sensitivity further shows the influence of the bottom mirror reflectivity on the device characteristics. The lack of a proper heat sink and poor thermal dissipation overall did not permit CW operation from these devices.

Figure 5.3 shows the 5°C polarization resolved L-I characteristic for a 10μm device with a 20mA threshold current . Polarization resolved pulsed light-intensity vs injection current (LI) were made by positioning a linear polarizer in front of the calibrated Ge detector in the standard L-I set-up. The two linear orthogonal eigen polarizations of the lasing emission are found to be aligned along the <110> crystal axes. The dominant eigen polarization, however, is always along one particular <100>crystal - parallel to either the [011] or the [01$\bar{1}$] - denoted // for the laser tested. Strain-compensated InGaAsP VCSELs often exhibit very different polarization properties compared to infrared GaAs-based VCSELs. For instance, in some lasers tested, simultaneous lasing in both orthogonal polarizations was observed with strong temperature sensitivity. This phenomenon known as "dual polarization" in VCSELs with

engineered compressive and tensile-strained InGaAsP multi-quantum well active regions, has been investigated and reported in the literature [2]. The electron to heavy hole transitions provide most of the TE gain; and the electron to light hole transitions provide all of the TM and a part of the TE gain. In our case, a predetermined and fixed polarization over a wide-temperature range and lasing modes may prove more valuable for polarization-sensitive applications.
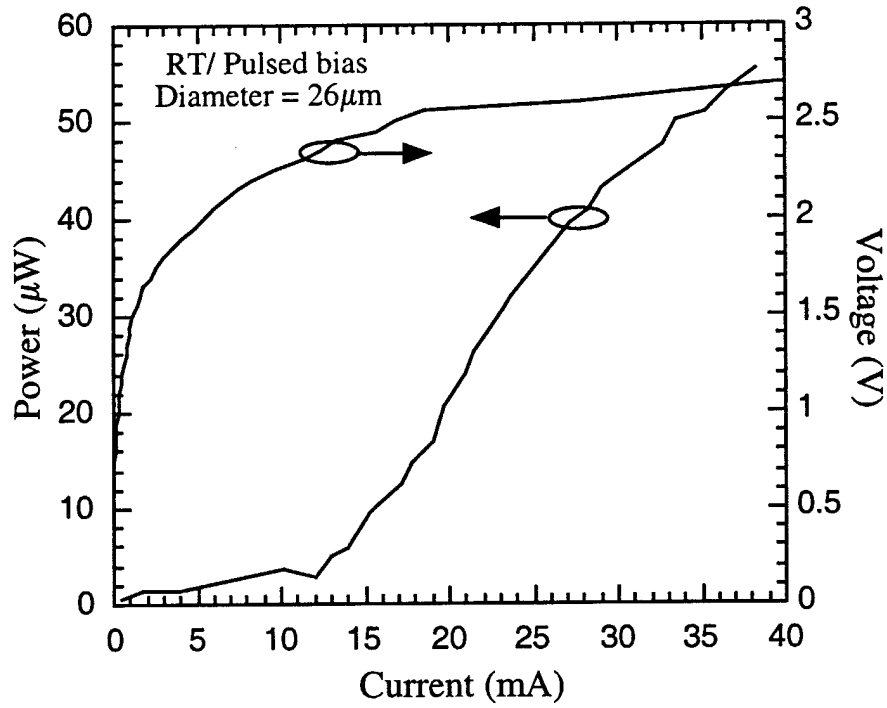
(a)
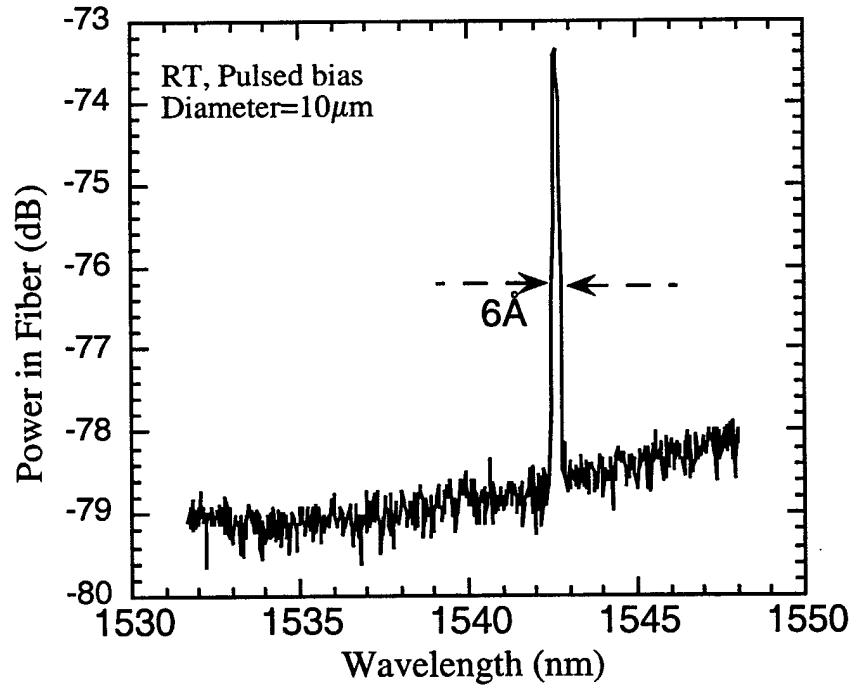
(b)

Figure 5.1: (a) Light vs current characteristics of 26μm devices operating at room temperature (pulsed) and, (b) optical spectrum of 10μm device (V_a=6V, I>I_{th})
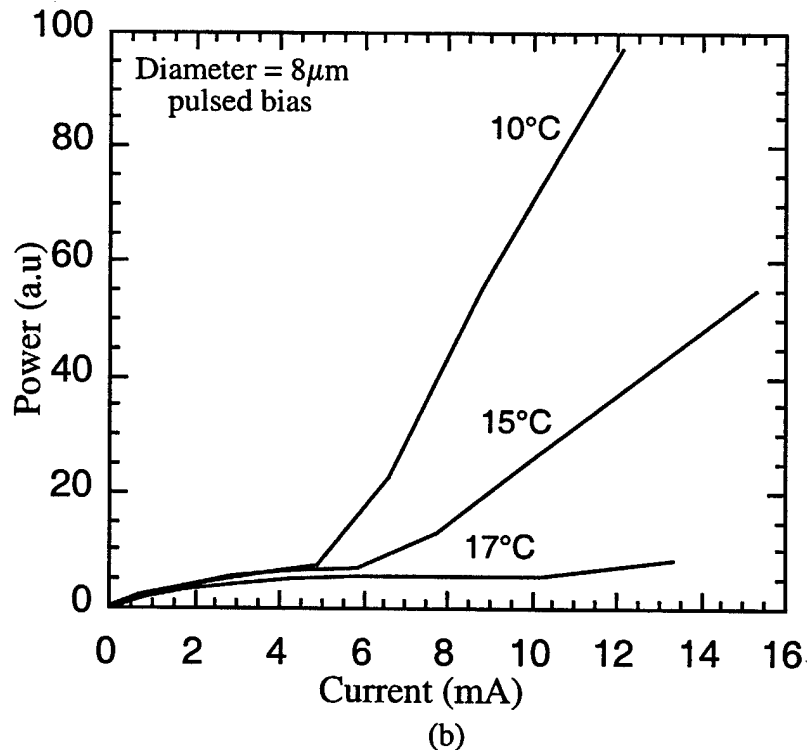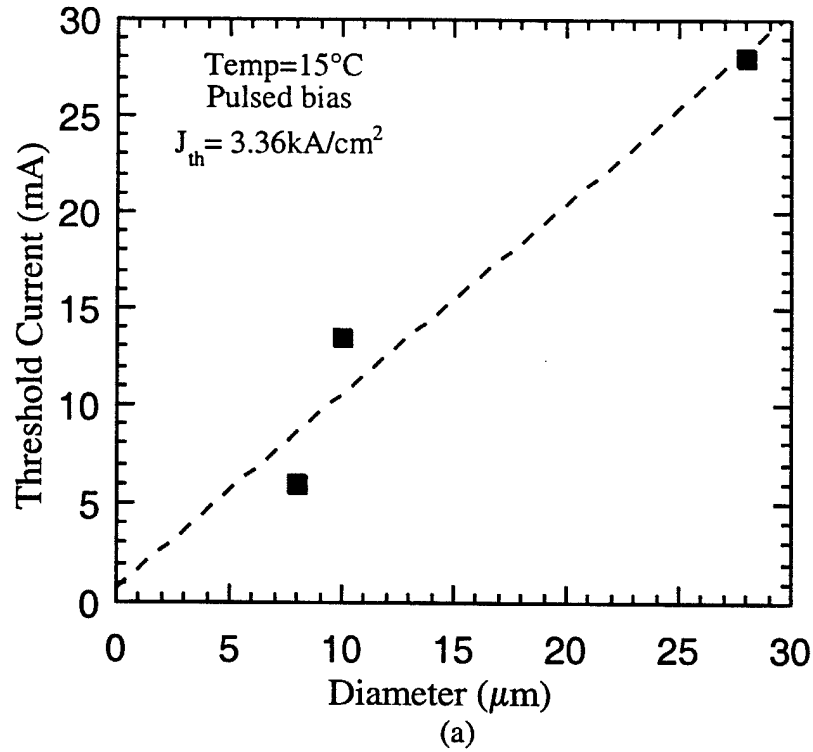
Figure 5.2: (a) Threshold current vs device diameter at 15°C and, (b) temperature dependence of the light-current characteristic for an 8μm device, under pulsed bias conditions.
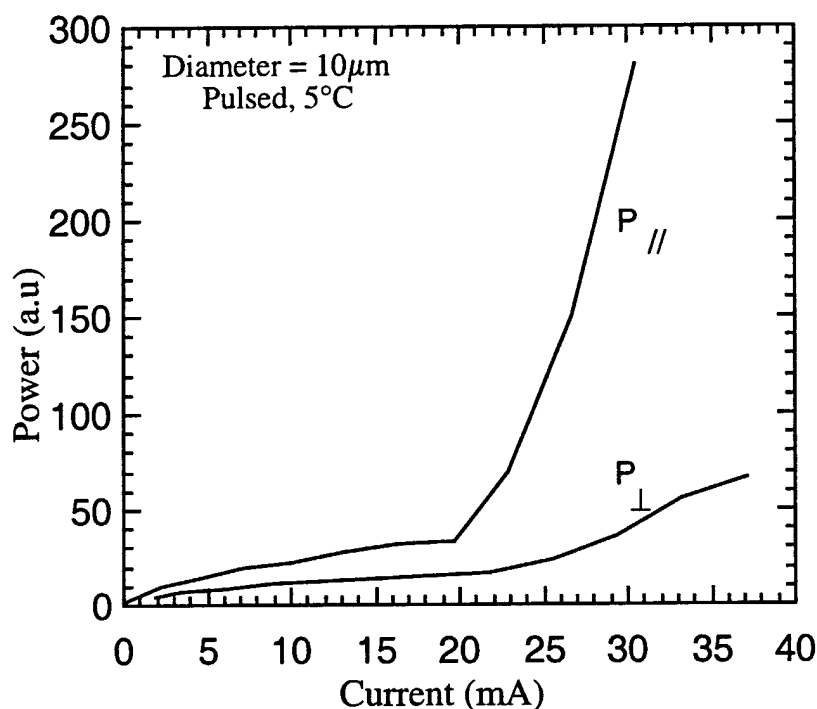
Figure 5.3: Polarization resolved L-I characteristic of a 10μm device; E // [011] or [01$\bar{1}$]

5.2.2.b   Resistance of the p-InGaAsP/InP Mirror

Above threshold, most of the voltage drop in the device is due to the electrical resistance of the bottom mirror. For low voltage operation of LW-VCSELs, it is better to remove the high resistance layers such as the InP/InGaAsP bottom mirror pairs which contribute to the overall series resistance of the device. Although the electrical resistance of p-GaAs/AlAs DBRs is widely reported [3],few groups have reported the resistance of n and p-doped InP/InGaAsP DBRs [4]. We have measured the resistance of the bottom mirror in these devices, since it contributes to the series resistance of the device and thus affects the external efficiency as studied in Chapter 4. Figure 5.4 shows the resistance of

45 pairs InGaAsP/InP DBRs, extracted from I-V characteristics obtained from varying size (20-40μm) mesas. The InP/InGaAsP were uniformly doped to 2×10^{18} cm^{-3}. The resistance of the p-doped DBR is found to be 2.03×10^{-6} Ω–cm^2/pair. This value agrees with published values of the resistance of n-doped InP/InGaAsP mirror. It is also important to note that this value is at least one order of magnitude lower than the reported value for p-doped InP/InGaAsP DBRs. The high resistance of the DBRs has been attributed to the valence band discontinuity between InP and InGaAsP [5]. For InP and InGaAsP ($E_g= 0.86$eV), as in this case, the valence band offset energy between InP and InGaAsP is 0.297eV; therefore the resistance of the p-DBR is mainly limited by the InP/InGaAsP interface resistance. Ensuring that the resistance of the bottom mirror is minimized is critical in achieving a low voltage drop across the device.

5.2.3 Discussion

5.2.3.a   Influence of Gain-Offset on Threshold Current

At this stage, it is important to discuss the temperature performance of long wavelength VCSELs. Long wavelength laser diodes show a strong temperature dependence, especially of the threshold current, which is caused by carrier leakage across the quantum wells and high non-radiative losses such as inter-valence band absorption (IVBA) [6] and Auger recombination [7]. The behavior of Fabry-Perot edge emitters can be characterized by T_o, while for VCSEL it has to be used cautiously. Here, the mode spacing is usually large and usually there is one mode in the range of the gain linewidth. Unlike in edge-emitters, varying the temperature leads to an offset λ_p-λ_c of gain peak wavelength λ_p and cavity mode λ_c. At low temperatures, this mismatch dominates the temperature sensitivity. It is a common design rule that the temperature
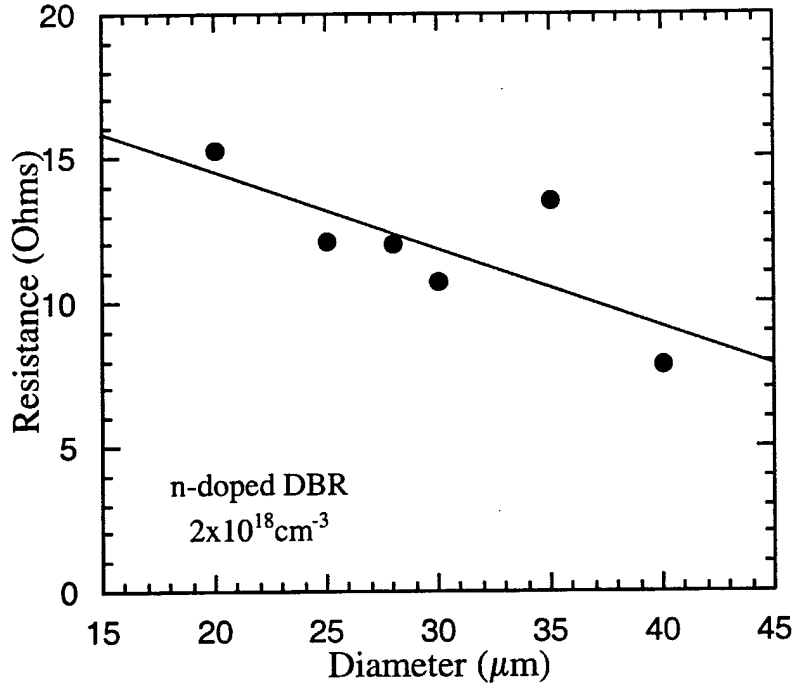
Figure 5.4: Resistance of the 45 pair n-doped (n =1×10^{18} cm^{-3}) InP/InGaAsP (λ=1.45 μm) DBRs vs mesa diameter

related minimum threshold current occurs for the matching case. This rule has been shown not to apply to long wavelength VCSELs [8-9].

Lasers with varying offsets at room temperature were fabricated and investigated by Rapp *et al.* at the Royal Institute Technology [9] of in a 1.5μm VCSEL with similar strain-compensated InGaAsP active region. The energy bandgap change with temperature is found by measuring the PL peak shift with temperature and is found to be −0.28meV /K, which corresponds to a wavelength shift of 0.54nm/K. The cavity mode shift, due to changes of the refractive indices with temperature, is small. For semiconductor layers, dn/dT generally is 2×10^{-4}K^{-1}, and the cavity mode red-shifts by about 0.1nm/K. The minimum threshold current and the zero gain-offset did not occur at the same temperature. When the gain offset λ_p-λ_e is increased by lowering the temperature, an increase in gain occurs for the same carrier density ie. The same gain is

achieved by a lower carrier density. Within a certain temperature change, this effect can overcome the mismatch of gain and cavity mode; the threshold carrier density decreases in spite of the bad tuning. For a large temperature drop, the gain drops again for N= constant and so, the mismatch dominates; the threshold current increases again. In other words, to maintain a given threshold gain g_{th} required for lasing, the threshold carrier density $N_{th}(T)$ is minimum for a gain-offset intentionally towards smaller wavelength ie. for λ_p-λ_e<0 at room temperature.

We have calculated the optical gain for one strain-compensated quatum well in our device. The optical gain is calculated[i]. on the basis of Fermi's golden rule and the
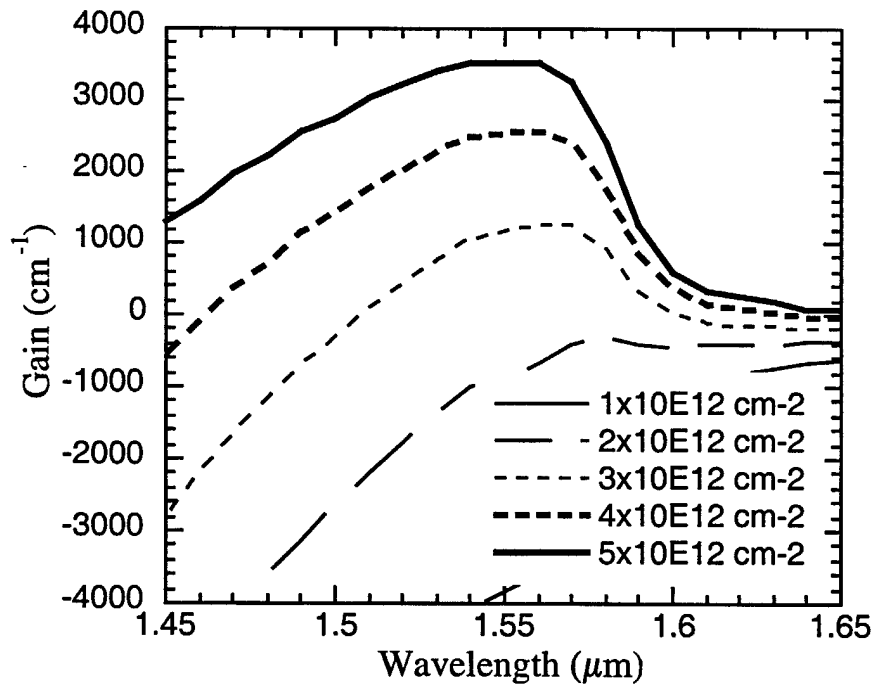
Figure 5.5: Calculated optical gain at room-temperature for varying sheet carrier concentrations

[i] Code for gain calculation was written by HongTao Jiang, *University of Michigan*
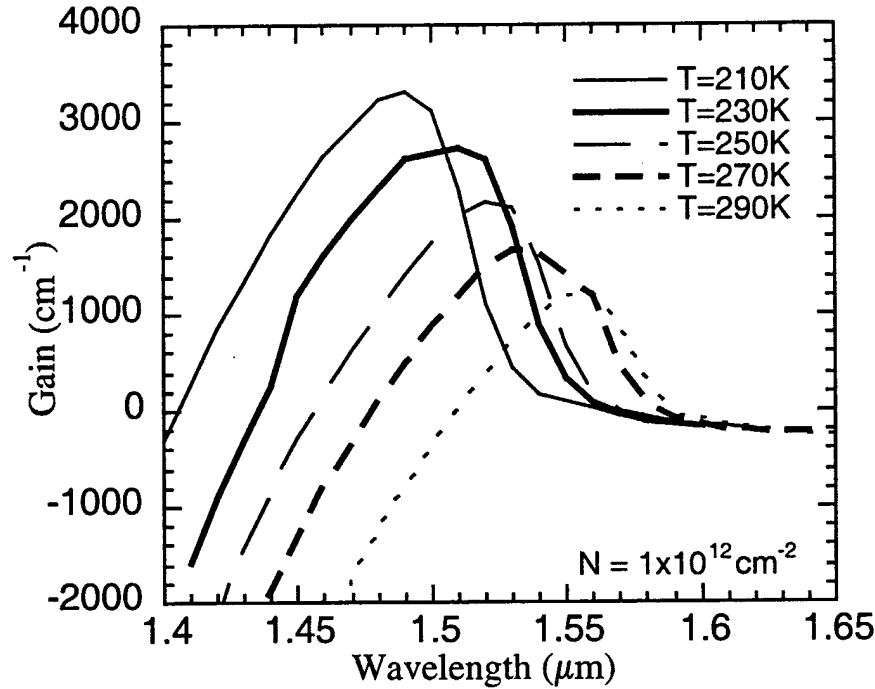
Figure 5.6:   Optical gain as a function of temperature for fixed sheet carrier density

by the 4x4 k•p bandstructure computations (taking the strain effect) detailed in [10]. Fig. 5.5 shows the gain as a funtcion of sheet carrier density at room temperature. From the data, we obtain a differential gain of 7.9×10^{-16} cm^2. The temperature dependence of the optical gain for a fixed sheet carrier density is plotted in Fig. 5.6. The gain peak rises with decreasing temperature. The peak wavelength blue shifts by -0.6nm/K. Most of the parameters for the $In_{1-x}Ga_xAs_yP_{1-y}$ quaternary compound were derived from the four binary compound parameters by using the interpolation scheme [11]. For our device, the room temperature gain-offset is -30nm.

5.2.3.b   Internal Cavity Loss

The threshold gain g_{th} is determined according to the formula:

$$\Gamma_l L_{eff}g_{th} = L_{eff}\alpha_c + \frac{1}{2}\ln\left(\frac{1}{R_t R_b}\right) \qquad (5.1)$$

where, Γ_l is the vertical confinement factor, L_{eff} is the effective cavity length, α_c is the internal loss of the cavity, and R_t and R_b are the top and bottom mirror reflectivities. We have calculated a longitudinal optical confinement factor to be 0.0045 from the vectorial transform matrix method used in Chapter 4. For our structure, the effective cavity length (which includes the penetration lengths into top and bottom mirrors) is calculated to be 0.5μm, using the simple formula from [12], also given in Appendix B.

We had previously measured the internal quantum efficiency of this device η_i from the threshold current density of edge-emitting lasers with various cavity lengths, taking into account the internal quantum efficiency and internal waveguide loss. It was found to be 0.6. The active region used was exactly the same as in this VCSEL. The confinement factor for the edge emitting lasers was estimated by a simple calculation.

The external differential quantum efficiency, for the top-emitting VCSEL, is expressed by:

$$\eta_d = \eta_i \frac{1 - R_t}{2\alpha_c L_{eff} + (1 - R_t)} \qquad (5.2)$$

This is valid if $(1-R_{top}) \ll 1$ and $(1-R_{bot}) \ll (1-R_{top})$, which is the case of interest in a VCSEL where we desire to extract all the light out one side of the cavity. As mentioned in an earlier chapter, the top and bottom reflectivities of our device and are 0.998 and 0.999, respectively. The optical output power density P is related to the current density J_i by:

$$P = (J_i - J_{th})\frac{hc}{e\lambda_o}\eta_d \qquad (5.3)$$

where e is the electron charge, h is the Planck constant, J_i is the radiative current density and c is the speed of light in vacuum. Figure 5.5 shows the radiative current density as a
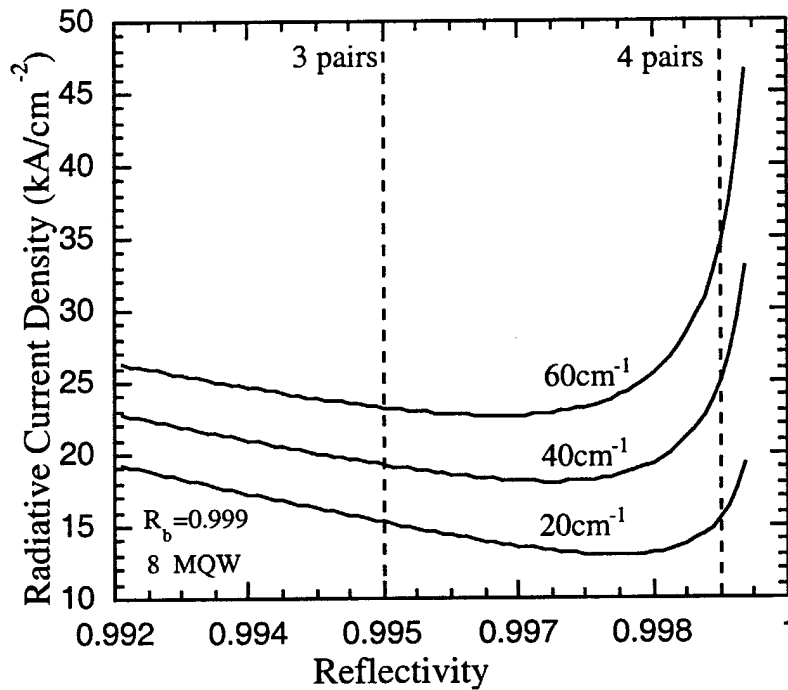
Figure 5.7: Current density needed to reach 1mW output power (from a $10\mu m$ diameter device) as a function of the top mirror reflectivity for 20, 40, 60 cm^{-1} internal loss.

function of top reflectivity R_t, when 1mW of power is required. The assumed device diameter is $10\mu m$. One can see that it is effective to reduce internal loss and choose an optimal mean reflectivity. Again, the reflectivities of 3 and 4 pairs Al_xO_y/GaAs are marked on the graph. Heating effect due to electrical resistance above threshold current density was ignored in this analysis.

Once again, it is clear that for this requirement, the optimal reflectivity is around 0.997, provided a uniform and high bottom reflectivity can be obtained over a large wafer area. In addition, although 5 pairs were used in this device to overcome the non-uniformity of the bottom mirror reflectivity, using more than 4 pairs of Al_xO_y/GaAs top DBR mirrors may have proved ineffective in further reducing the threshold current density of these devices.

5.3 Other Loss Mechanisms

Other mechanisms contribute to the overall loss and limit the performance of these devices, including self-heating, carrier losses and optical losses. Self-heating is to the internal heat production of and heat flux towards the heat sink, low voltage consumption, series resistance measurement.

Carrier losses are caused by injected electrons and holes that do not recombine within the quantum wells (carrier leakage) and those which participate in non-radiative recombination processes such as Auger recombination and Shockley-Read-Hall recombination. All these recombination processes depend on the ambient temperature.

Optical losses are due to photons that leave the resonant optical wave in the cavity by emission, absorption or scattering. In general, these loss mechanisms also depend on the temperature of the device. Photon scattering happens at the mirror sidewalls or at the oxide aperture rim, within the first mesa. Another prominent absorption mechanism at 0.8eV photon energy is inter-valence band absorption (IVBA) by electron transitions from the split-off valence band to the heavy hole band [13-14]. This type of absorption generally increases with injected carrier density and exponentially rises with temperature. The overall effect of the above probable loss mechanisms is to rise g_{th} strongly, leading to rising N_{th} and increasing I_{th}.

5.4 Summary

1.5μm vertical cavity surface emitting lasers were fabricated using standard laser fabrication techniques including selective oxidation of InAlAs for current confinement . The characteristics of the laser were studied in this chapter. Based on the data, the performance is found to be limited by the non-uniformity of the bottom reflector over the area of the sample, resulting in large cavity-gain detuning. In addition, heavy losses due

to self-heating and other non-radiative recombination processes limit the performance of these devices.

Room temperature operation, under pulsed bias conditions is reported with a minimum threshold current of 5mA for 8μm diameter device at 15°C and maximum output power of 60μW for a 26μm device. Finally, the optimal top reflectivity R required to obtain 1mW optical power at low current densities is predicted for various internal cavity losses. Again, it is clear that optimizing the top mirror reflectivity is key in reducing current density. The results from these VCSELs can be used as guidelines for developing future higher performance LW-VCSELs.

References

[1] C. Amano, Y. Itoh, H. Takenouchi, T. Tadokoro, T. Kurokawa,"MOVPE growth of InGaAsP/InP-based vertical cavity structures for wafer-fused VCSELs", *J. of Crystal Growth*, Vol. 187, pp.35-41(1998)

[2] A. Mathur and P. Dapkus,"1.55μm dual polarization lasers, implemented with compressive and tensile strained quantum wells", *IEEE Photon. Tech. Lett*, Vol. 7(11), p.1243 (1995)

[3] R. F. Kopf, E. F. Schubert, S. W. Downey, and A. B. Emerson,"N-and P-type dopant profiles in distributed Bragg reflectors structures and their effect on resistance", *Appl. Phys. Lett.,* Vol. 61,pp.1820-1822, 1992

[4] Y. Ohiso, C. Amano, Y. Itoh, H. Takenouchi and T. Kurokawa," Long wavelength (1.55μm) vertical cavity lasers with InGaAsP/InP –GaAs/AlAs DBR's by wafer fusion", *IEEE J. of Quantum Electron.*, Vol. 34(10), pp.1904-1913, 1998

[5] T. Miyamoto, K. Mori, H. Maekawa, Y. Inaba, F. Koyama, and K. Iga, "Carrier transport in p-type GaInAsP/InP distributed Bragg reflectors", *Jpn. J. of Appl. Phys.*, Vol. 33, pp. 2974-2976 (1992)

[6] J. Piprek, D. I. Babic and J. E. Bowers," Numerical analysis of 1.54μm double-fused vertical cavity laser operating CW up to 33°C", *Appl. Phys. Lett*, Vol. 68, pp.2630-2632, 1996

[7] G. P. Agrawal and N. K. Dutta, *Semiconductor Lasers*, New York: Nostrand Reinhold, 1993

[8] M. Osinki, "Vertical cavity surface emitting lasers: effects of heating on modal characteristics and threshold current", *Proceedings of SPIE*, Vol.2398, pp.42-57,1995

[9] S. Rapp, J. Piprek, K. Streubel, J. Andre, E. Rodriguez Messner and J. Wallin," temperature performance of 1.55μm vertical cavity lasers with integrated InP/InGaAsP Bragg reflectors", *Proceedings of IPRM Conf.*, Boston, MA, pp. 36-39, 1997.

[10] S. Seki, T. Yamanaka, W. Lui, Y. Yoshikuni, K. Yokoyama, "Theoretical analysis of pure effects of strain and quantum confinement on differential gain in InGaAsP/InP strained quantum-well lasers", *IEEE J. of Quantum Electron.*, Vol. 30, pp.500-509, 1994.

[11] S. Adachi, "Material parameters of $In_{1-x}Ga_xAs_yP_{1-y}$ and related binaries", J. Appl. Phys. Vol.53, pp.8775-8792, 1982.

[12] D. I. Babic and S. W. Corzine, "Analytic expression for the reflection delay, penetration depth and absorptance of quarter wave dielectric mirrors", *IEEE J. of Quantum Electron.*, Vol. 28, pp.514-524, 1992.

[13] I. Joindot and J. L. Beylat,"Intervalence band absorption coefficient measurements in bulk layer strained and unstrained MQW 1.55μm semiconductor lasers,"

[14] J. Piprek," High temperature lasing of long wavelength VCSELs: problems and prospects", *Proceedings of the SPIE*, Vol. 3003, p.182 (1997)

6. GaAs-BASED HIGH POWER VCSEL ARRAYS

6.1   Background

6.1.1   VCSEL Arrays for High Power Application

Two-dimensional (2-D) arrays of semiconductor lasers offer the promise of very high power levels with a large aperture producing a narrow beam divergence [1]. Ideally, one would use a coherent array of lasers to produce large amounts of power. As in one-dimensional edge-emitting arrays, maintaining coherence laterally over a large area is a major challenge in two-dimensional arrays. Coherence is therefore extremely important for applications that require power delivered to a point, such as, a satellite receiver. For an array with N elements, each producing the same output power P, the on-axis power in the far field is ~NP for an incoherent array, but ~N^2P for a coherent array [2]. Although coherent arrays have been demonstrated with VCSELs, there are many obstacles to maintaining coherent, single frequency operation at very high powers. As the 2-D array increases in size, the number of modes increases. Also, the quality of the mirrors (unlike the near-ideal cleaved facets of edge-emitters) is critical, requiring excellent fabrication techniques to obtain good performance and beam quality. If a monolithic approach is to be taken to fabricate coherent 2-D arrays, the layer thickness and compositions must be

not only near perfect, but also, excellent uniformity and flatness must be maintained over a large area.

2-D VCSEL coherent or incoherent (not phase-locked) arrays are also expected to be of great use for application where conventional but less efficient high power gas and solid-state lasers are used. The power, efficiency, and beam properties of individual emitters and arrays make them ideal for applications of lasers in data storage, medicine, laser printing, remote switching, solid-state laser pumping, illuminators, and space and fiber communication systems. In addition, the planar nature makes them ideal for optical processing, computing, neural networks and optoelectronic integrated circuit (OEIC) applications where optical interconnects provide a solution to communication between IC chips. Therefore it is worthwhile to design and fabricate efficient VCSELs arrays using a practical fabrication process and, to study their optical characteristics.

This chapter concentrates on the process development of incoherent selectively-oxidized VCSEL arrays for high power application. Emphasis will be placed on the fabrication technology, differential efficiency, and thermal crosstalk issues. Heat removal is critical and necessary since even in the very best devices, only half of the input power is converted to optical power.

6.1.2 Selectively Oxidized VCSEL Arrays

Small VCSELs with typical sizes of 5-10μm and low output powers of a few mW have been established as efficient light sources for application such as optical interconnects, but do not render enough power for high power appplications[3]. During the last few years, the wall plug efficiency of VCSELs have slowly been increased to >50% [4-5], enabling even small devices to emit powers of ~50mW. The maximum power depends strongly on power conversion efficiency, but is limited by the thermal rollover. Thus, high output power are expected from large areas of efficient lasers.

Although broad area top-emitting VCSELs with output power of 180mW (CW) have been demonstrated [6], it has been found that quantum and conversion efficiencies decrease very quickly, owing to less efficient heat dissipation. In addition, poor beam quality due to current crowding near the aperture makes these devices unsuitable for high power applications. Large diameter $70\mu m$ bottom-emitting devices, which have been shown to benefit from more homogeneous current distribution with power outputs of 350mW have been achieved. However, the conversion efficiency of such devices decreases with increasing active area. Thus output powers in the watt regime seem unattainable with single devices.

The alternate technique to achieving high power is to combine the output power of as many as possible emitters in an array. Earlier array work has focused on etched pillars as a means for both current and optical confinement, thereby reducing the threshold current. However, the success of this fabrication technique was limited by the surface recombination at the etched sidewalls, sidewall optical scattering and highly non-planar processing. Recently, succesful fabrication of VCSEL arrays with high packing density using selective oxidation and parallel electrical contacting have been demonstrated [7]. Attempts to achieve scalable powers from VCSEL arrays have been limited by difficulties in thermal management and non-uniformity between elements of the array. Thermal coupling between adjacent elements increased with array size. Additionally, for larger array sizes, it was observed that higher order mode operation was favored even in pulse bias operation [8].

In this study, densely-packed 2D oxide-confined top-emitting VCSEL arrays were investigated with array elements varying in diameter size from $4\mu m$ to $24\mu m$ after oxidation. The aim was to achieve high overall output powers at reasonably high conversion efficiencies and optical power densities - which can be realized with oxide-confined VCSELs. In addition, improved thermal characteristics and efficiencies are

expected with proper heat sinking. Much of this work was done in collaboration with *Princeton Electronics Systems Inc*, based in New Jersey.

## 6.2 Device Structure and Processing of Oxide-Confined GaAs-based VCSELs

6.2.1 GaAs-based VCSEL with InGaAs/AlGaAs Active Region

The VCSEL structure was grown by MOVPE. The layer structure used for this device is shown in Fig. 6.1. The epitaxial layers were grown on n+ GaAs substrate and, are: a 0.5μm GaAs buffer layer, a 0.05μm AlAs layer, 29 pairs of n-doped Al $_{0.8}$Ga $_{0.2}$As/GaAs mirror layers and a n-doped Al $_{0.96}$Ga $_{0.04}$As layer for oxidation. Graded DBRs consisting of 663Å Al $_{0.8}$Ga $_{0.2}$As, 100Å grading layer , and 663Å GaAs, doped with Si to 3e18cm^{-3}, are used for each pair. Using Si for n-type doping results in low loss and low resistivity mirrors. The resonant cavity consists of two AlGaAs/InGaAs MQW in a AlGaAs spacer layer. The laser is designed for emission at 945nm. Above the cavity is a p-doped Al $_{0.96}$Ga $_{0.04}$As oxidation layer, followed by 17 pairs Al $_{0.8}$Ga $_{0.2}$As/GaAs. The mirrors are C-doped to 1-4e18cm^{-3} with the exception of the top three pairs, which are doped with Zn to greater than 1e19cm^{-3}. The low diffusion coefficient and the high ionization rate of C can been exploited in this design to form sharper doping doping profiles with increased doping levels at the heterojunctions and a lowered doping concentration throughout the rest of the mirror

The as-grown relative reflectance spectrum measured on an area of the wafer is shown in Fig. 6.2(a) . The resonance wavelength is obtained directly from this measurement. Figure 6.2(b) shows the variation of the resonant wavelength across the

x3	GaAs 574Å	Zn, >1e19 cm^{-3}
	Al(x)GaAs (0.8->0) 100Å	Zn, >1e19 cm^{-3}
	Al(x)GaAs (0.8) 663Å	Zn, >1e19 cm^{-3}
	Al(x)GaAs (0.8->0) 100Å	Zn, >1e19 cm^{-3}
x14	GaAs 574Å	C, 1e19 cm^{-3}
	Al(x)GaAs (0.8->0) 100Å	C, 1-4e18 cm^{-3}
	Al(x)GaAs (0.8) 663Å	C, 1-4e18 cm^{-3}
	Al(x)GaAs (0.8->0) 100Å	C, 1-4e18 cm^{-3}
	GaAs 574Å	C, 1e18 cm^{-3}
	Al(x)GaAs (0.96) 663Å	C, 1e19 cm^{-3}
	Al(x)GaAs (0.3) 1234Å	C, 3e17 cm^{-3}
	In(x)GaAs (0.15) 70Å	U/D, 1e19 cm^{-3}
	Al(x)GaAs (0.3) 80Å	U/D, 1e19 cm^{-3}
	In(x)GaAs (0.15) 70Å	U/D, 1e19 cm^{-3}
	Al(x)GaAs (0.3) 1234Å	U/D, 1e19 cm^{-3}
	GaAs 574Å	Si, 1-3e18 cm^{-3}
x29	Al(x)GaAs (0.96) 663Å	Si, 1-3e18 cm^{-3}
	GaAs 574Å	Si, 1-3e18 cm^{-3}
	Al(x)GaAs (0.8->0) 100Å	Si, 1-3e18 cm^{-3}
	Al(x)GaAs (0.8) 663Å	Si, 1-3e198cm^{-3}
	GaAs 2μm buffer	Si, 1-3e19 cm^{-3}
	AlAs	Si, 1-3e19 cm^{-3}

GaAs n+ <100>substrate

Figure 6.1:   Layer structure for InGaAs/AlGaAs VCSEL (target λ =945nm). The dashed line represent similar grading as for the mirror layers
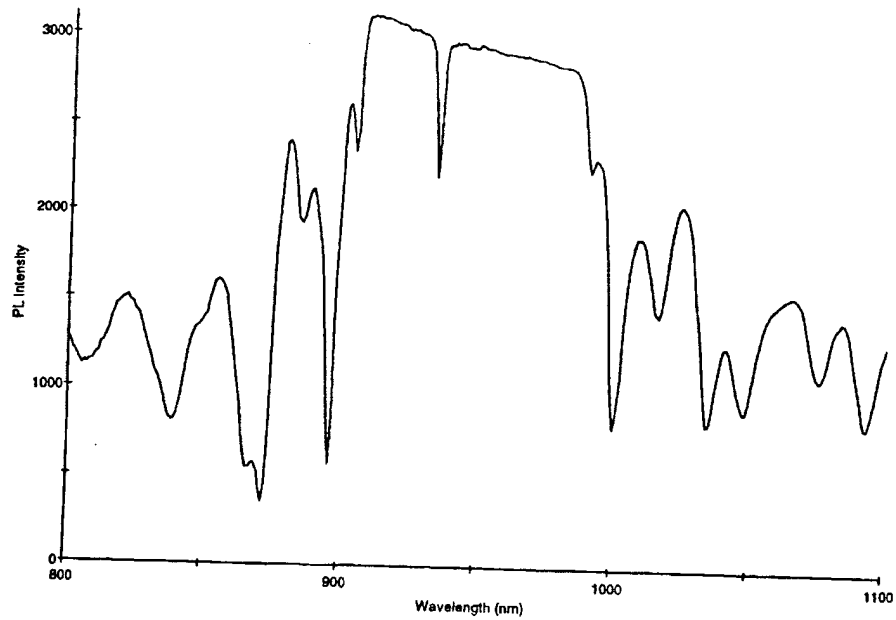
(a)
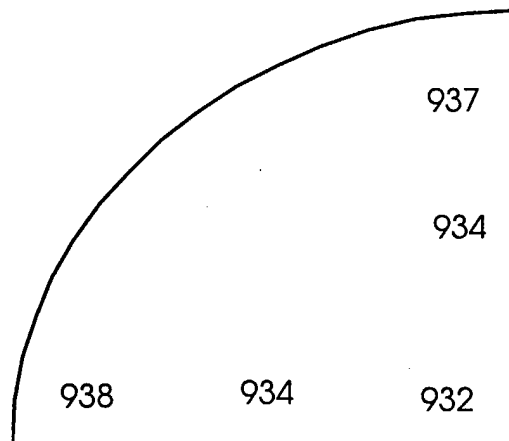
(b)

Figure 6.2: (a) Reflectance measurement on wafer (etalon at 934nm) and (b) map of the etalon peak wavelengths on the quarter inch wafer processed

wafer area. Because the lasing wavelength is determined by the cavity resonance wavelength, this last one is measured at several points on the wafer. In this case, the cavity resonance wavelength varied between 933-950nm across the wafer. Although not necessary in our case, the lasing wavelength can be tuned/adjusted in the last step of processing, using a dielectric mirror. This can be done with a deposition system that can simultaneously measure deposition rate and monitor the reflectance on wafer.

6.2.2 Fabrication of VCSEL array

The VCSEL array fabrication process is shown in Fig. 6.3, for an individual array element. The fabrication begins with the deposition of a Pt./Ti/Pt/Au/Ti p-ohmic metal ring contacts. Mesas (ranging in diameter between 20-50μm) are defined by lithography and and etched by reactive ion etching (RIE) using a BCl_3/Ar gas combination plasma. It is necessary to etch a pillar down to the n-doped layers below the cavity, since the VCSEL has two oxidation layers. Following the RIE step, the mesas were wet-etched in a weak phosphoric acid-based solution prior to oxidation to remove any RIE damage.

The mesas were oxidized according to the desired aperture sizes. Generally, the devices are selectively oxidized typically for 30-40 mins at 450 °C. The oxidation rate for C-doped $Al_{0.96}Ga_{0.04}As$ at this temperature is 0.8μm/min. Both the n and p-doped Al $_{0.96}$Ga $_{0.04}$As layers were oxidized. Following oxidation, the Ni/Ge/Au/Ti/Au n-contact metal is evaporated. Mesas were planarized using a photosensitive polyimide. Contact holes were opened by exposing the polyimide and developing it. The polyimide was cured overnight at 280°C. Ti/Al/Au interconnect metal was deposited above the polyimide to contact the p-ohmic ring while keeping the center of the ring contact open for light output. Contact is also made to the n-ohmich metal from the top. This VCSEL

uses intra-cavity contacts which can be used effectively in oxide-confined VCSELs and reduce the series resistance dramatically [9].

Because the device only contains 17 pairs of AlGaAs/GaAs top mirror pairs, it was necessary to deposit one or two additional MgF_2/ZnSe dielectric mirror pairs to increase the top reflectivity. This was done in the last step of processing, prior to substrate thining. The dielectric mirror was deposited using a standard electron beam evaporator and lifted-off using a standard photoresist recipe. The refractive indices of MgF_2 and ZnSe were 1.45 and 2.56 respectively, at $\lambda= 945nm$. The refractive indices vary with substrate temperature during the evaporation; therefore it was critical to calibrate the mirror prior to each deposition. The mask used in this process was comprised of individual devices with varying diameters, as well as 2x2, 2x4, 4x4 and 10x10 arrays of these devices. Figure 6.4 shows optical micrographs of fabricated 10x10 and 4x4 arrays, prior to mirror deposition.

1. Evaporate p-ohmic rings and pattern mesas fo
oxidation

p-ohmic

Layers exposed
for oxidation

Top
DBR

Bottom DBR
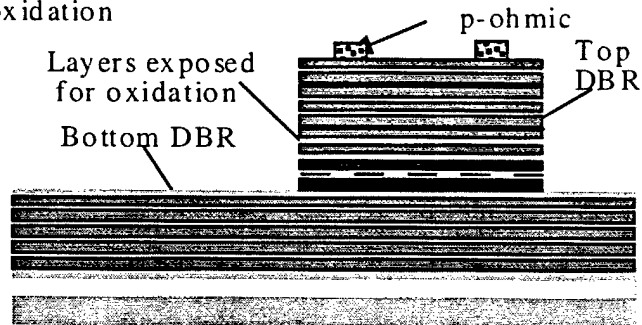
2. Oxidize AlGaAs (x=0.96) to AlxOy

Oxidized
layers
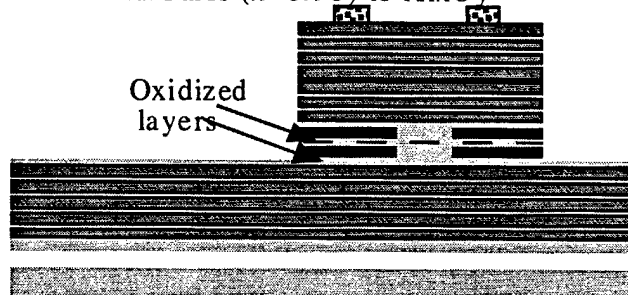
3. Evaporate n-ohmic metal, planarize with
polyimide and evaporate interconnect metal

polyimide
n-ohmic
interconnect
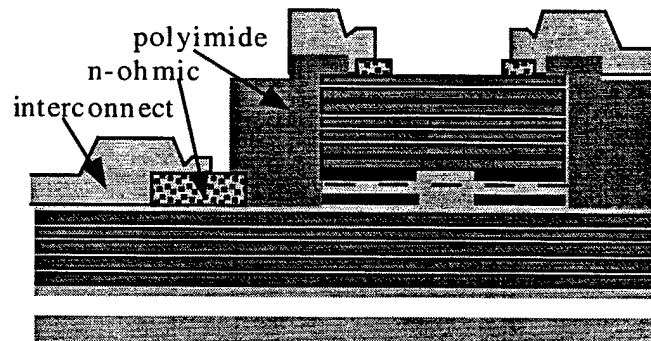
4. Evaporate dielectric mirror and lift-off
dielectric for probing areas

$MgF_2/ZnSe$
mirror

Figure 6.3: Fabrication sequence for a single element in the array
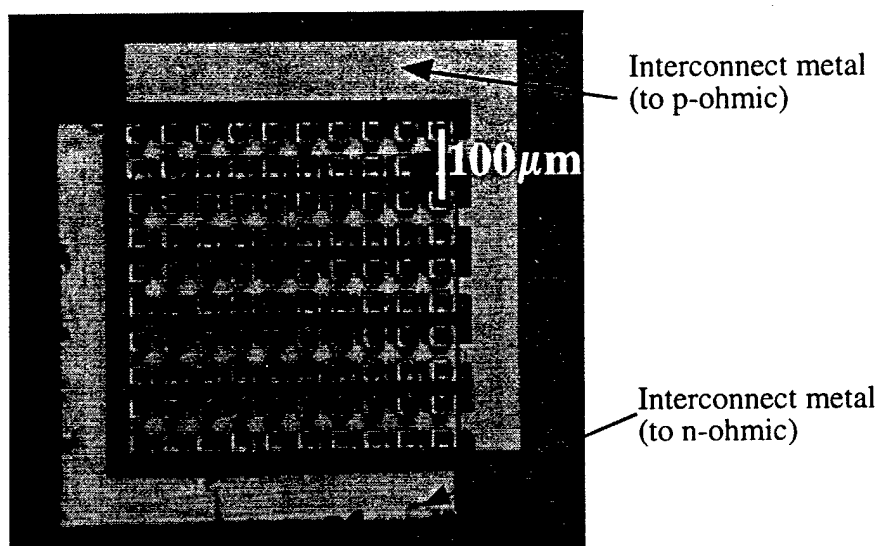
(a)
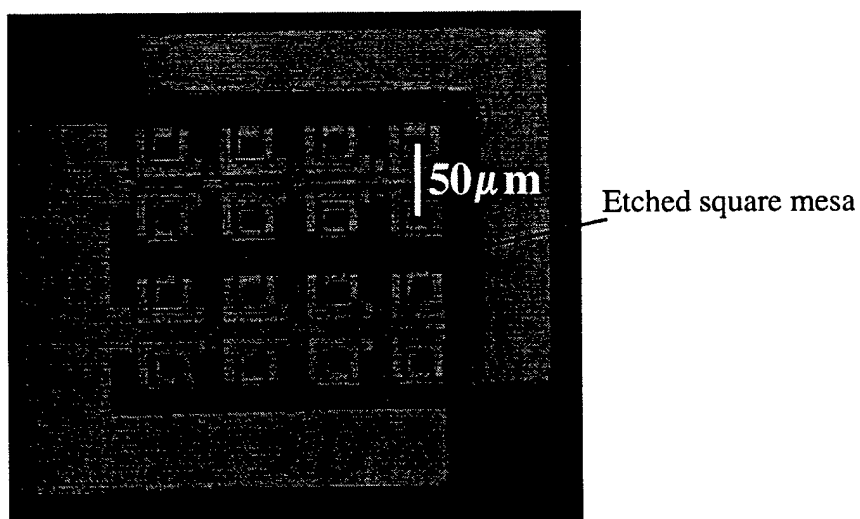
(b)

Figure 6.4: Optical micrographs showing two array sizes, with 40μm etched diameter mesas (pitch=50μm): (a) 10x10 array and, (b) a close up of 4x4 array

6.3   Characterization of VCSEL Arrays

6.3.1   Light Output Characteristics

Individual devices were thinned and mounted on a diamond-coated substrate for efficient cooling. Reduced thermal resistances of heat-sinked devices lead to higher output powers [10]. Figure 6.5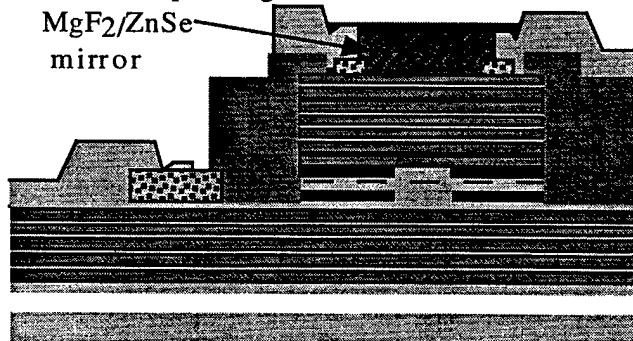 shows the typical light-current (LI) characteristic of a single 24μm individual device under continuous wave operation. Output power of the device increases linearly above threshold and rolls over for higher currents due to self-heating. The average threshold currents recorded for the 4, 14 and 24μm devices, at room temperature, were 0.3, 0.8 and 1.9mA respectively.

Figure 6.5:   Typical CW L-I(solid) and V-I (dotted) charateristic of a 24μm device at 15°C

The highest conversion efficiency was obtained for the 4μm devices . These can emit a maximum power up >0.8mW with less than 10mA supplied. The average differential quantum eff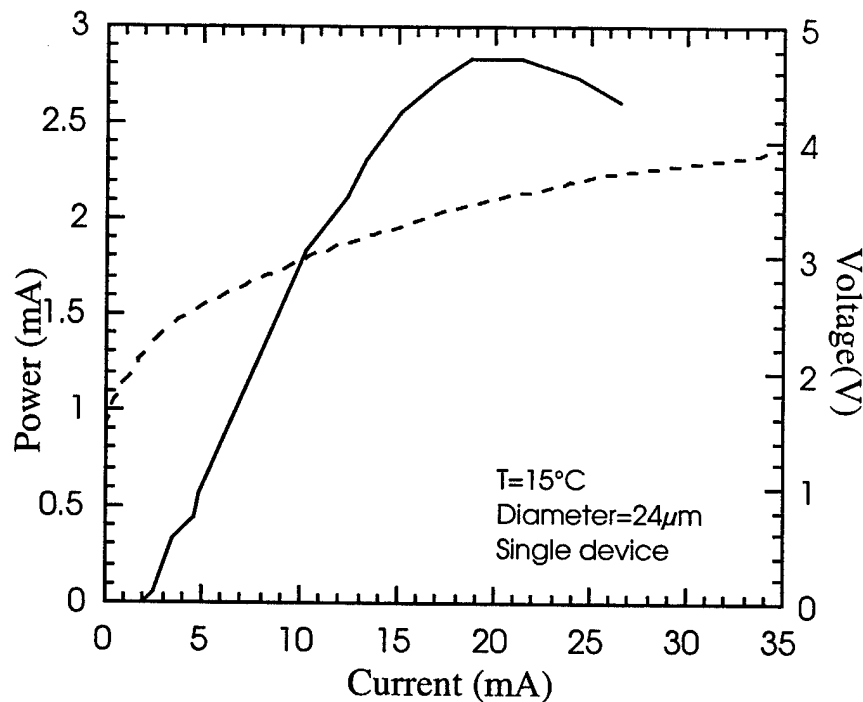iciency, obtained from the slope efficiency right after threshold, was 31.6%. The maximum external efficiency of the device was ~5%.

The temperature dependence of the LI characteristic of a 14μm device was investigated. Figure 6.6 shows the LI chraracteristic measured as the temperature is varied from 10°C to 40°C. The slope efficiency dropped at a rate of 0.005W/A-K. We can obtain a value of the characteristic temperature using the temperature dependence of the threshold current given by $I_{th} \cong I_o \ exp(T/T_o)$[11]. The characteristic temperature is a figure of merit commonly used to represent the temperature sensitivity of the laser. The T_o in this case is 71K for this temperature range.

One of the challenges in making large size arrays is to achieve scalable power. The CW LI- characteristics of different size arrays of 14μm devices are shown in Fig.6.7. The strong internal heating suppresses CW laser emission in the larger arrays and quickly causes the thermal rollover. Reduced efficiencies in the large arrays are mainly caused by increased heating and possibly thermal crosstalk, which is investigated later in section 6.4.2.

The internal quantum efficiency of these devices was also calculated by fabricating in-plane broad-area lasers with the material and, measuring threshold current densities for different lengths lasers. An optical confinement factor was calculated and the internal cavity loss was estimated for the material. From the measurements, we extracted an low internal quantum efficiency of ~59%. The differential efficiency is therefore limited by it. Further optimization of the active region in future designs will be needed.

Finally 10x10 arrays were also tested on the thinned substrate. As can be seen from the infra-red image in Fig. 6.8(a), not all the devices in the array are on, especially in the periphery of the array. Figure 6.8(b) shows the L-I-Vcharacteristics of a 10x10
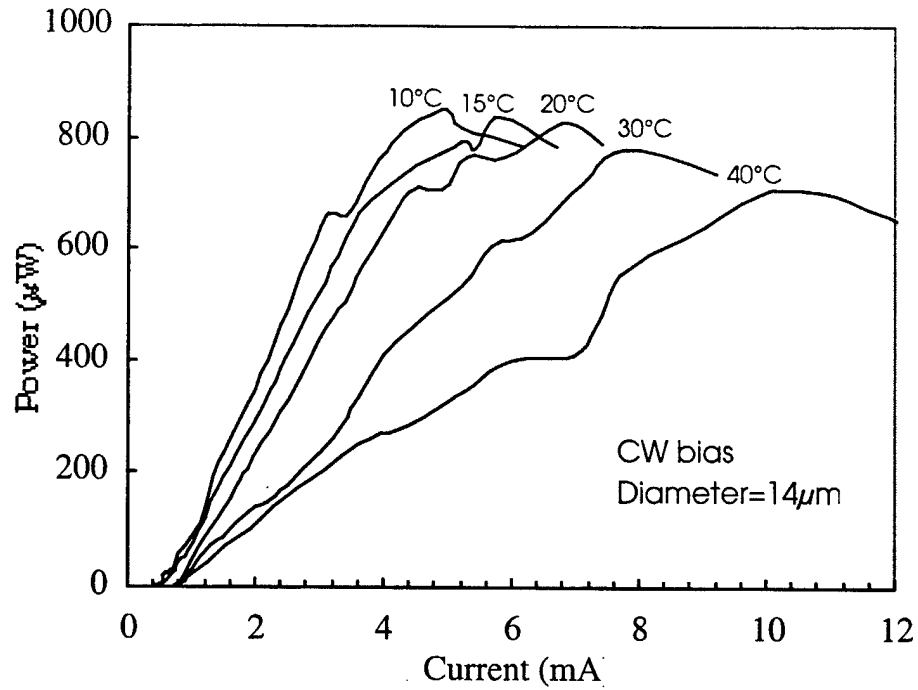
Figure 6.6:   CW L-I characteristic of a 14μm device as a function of stage temperature.
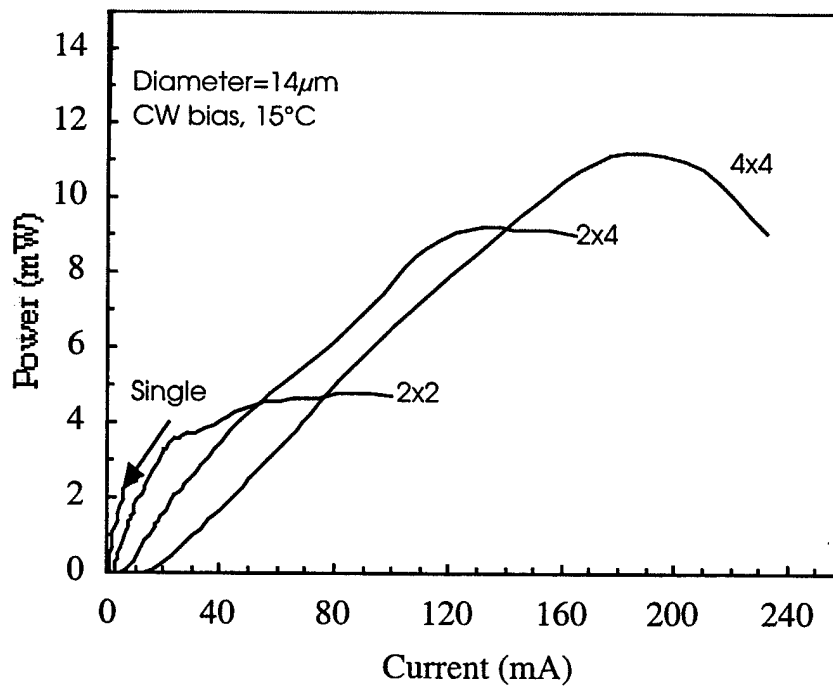
Figure 6.7:   Room temperature continuous-wave light-current characteristic of 14μm for a single, 2x2, 2x4 and 4x4 array at 15°C.
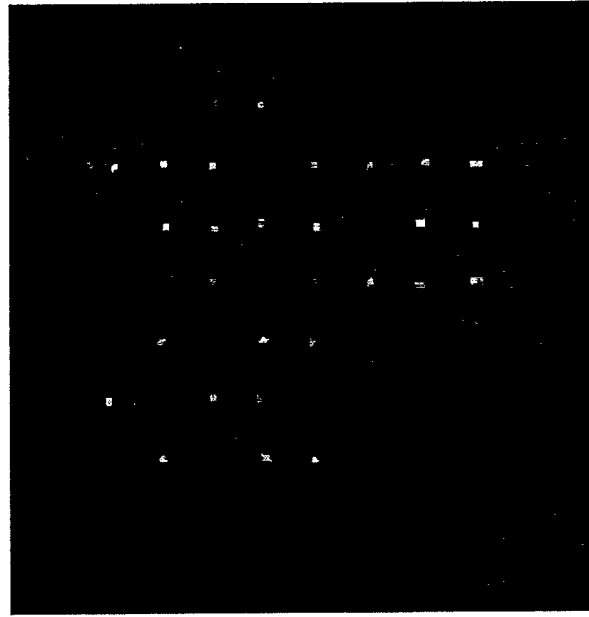
(a)
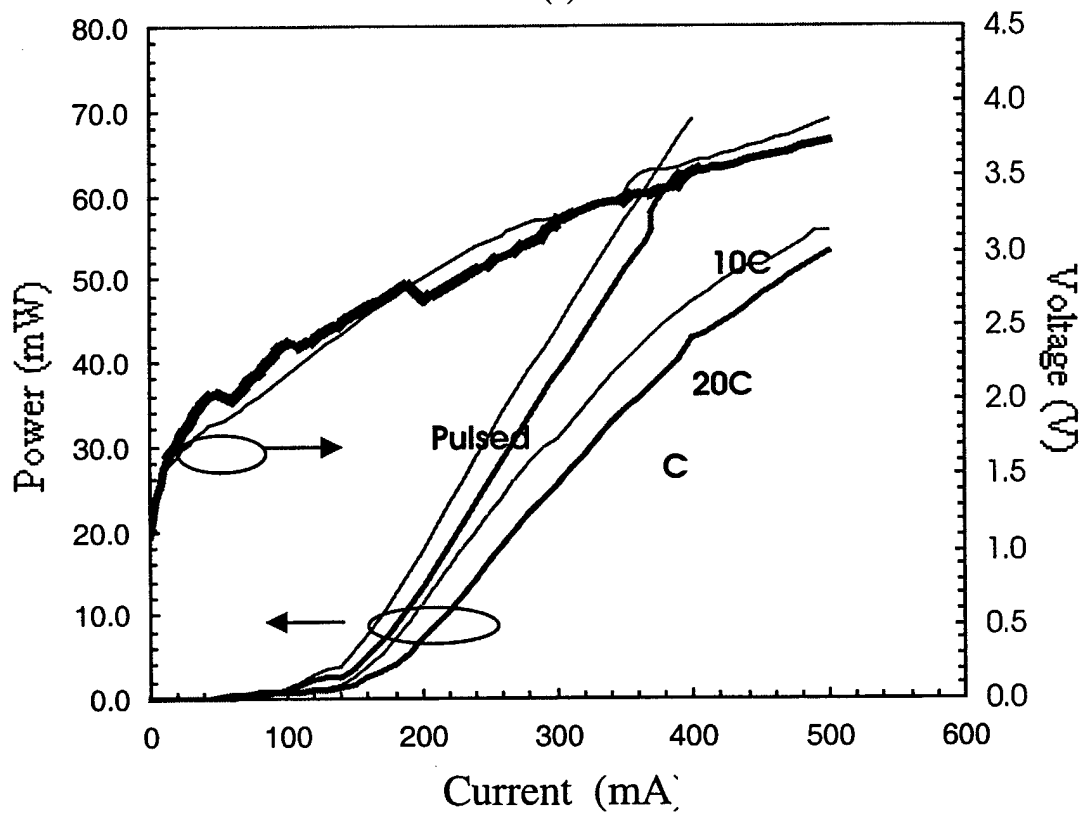
(b)

Figure 6.8:   (a) Infra-red image of the 10x10 array (I =150mA) and (b) Pulsed and
CW light-current-voltage charateristic of 10x10 array (diameter =24μm) tested at
10°C and 20°C

array at 10°C and 20°C. A maximum power of 55mW was obtained with a CW source. The array was also tested under pulsed operation using conditions similar to the CW tests. The current source could only supply up to 500mA. From the graph, it is evident that output power > 100mWcan be achieved which is adequate for many pratical applications.

6.3.2 Thermal Characteristics

Thermal resistance of the etched and oxidized pillar lasers is dominated by the thermal conductivity of the bottom DBR mirror in the normal direction to the layers. Since phonon scattering at the interfaces is high, the thermal conductivity of

Figure 6.9: Optical micrograph showing 2x2 array of individually addressed 40μm diameter elements used in the thermal crosstalk study

AlGaAs/GaAs is expected to be higher than the bulk values [12]. Thermal crosstalk between elements increases the internal device temperature in the array elements, resulting in an altered transverse mode behavior .

Thermal crosstalk is measured by monitoring the wavelength shift in one device as a neighbor is activated, ie. while laser 1 is kept at a constant input power and the electrical input power ΔP_2 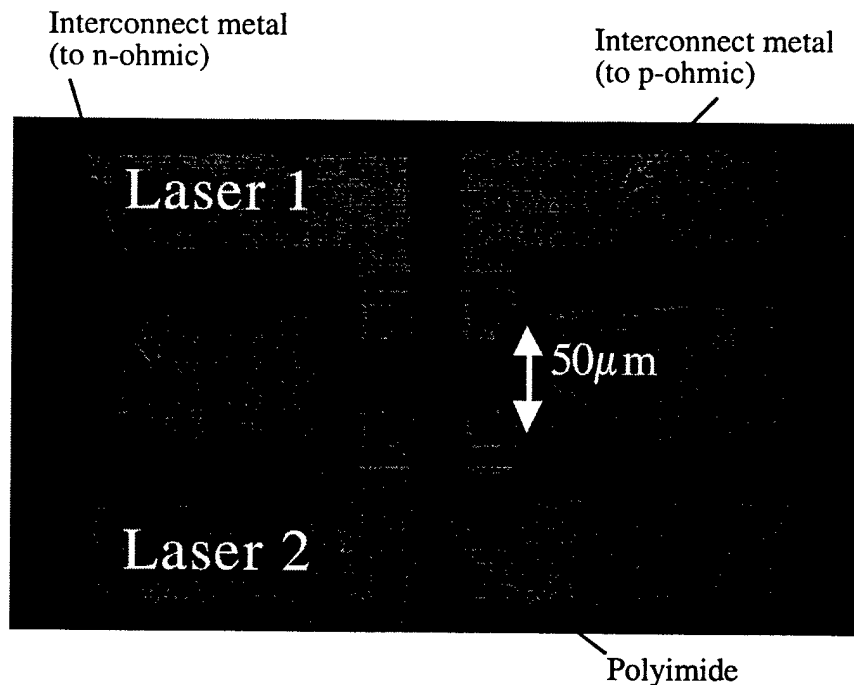of laser 2 is varied. For this measurement, individually addressed array elements, illustrated in the optical micrographs of Fig. 6.9, are fabricated. The devices tested are operated above threshold. Spectral measurements on laser 1 are made using the HP-OSA and a single mode fiber, as described in section 1 of Chapter 5. Care is taken to couple light only from laser, by aligning the fiber to maximize input from laser 1 while eliminating any input from laser 2. Figure 6.10 represents the modal red-shif of laser 1 as the current in laser 2 is changed from $I_1 = 3mA$ to $I_2 = 6mA$.

The thermal isolation between laser 1 and laser 2, used to describe thermal crosstalk is defined by:

$$Z_{12} = \Delta P_2 / \Delta T_1$$

ΔT_1 is obtained by measuring $\Delta \lambda_1$. The Thermal sensitivity $\Delta T / \Delta \lambda$ is obtained by varying the ambient temperature of several devices and measuring the modal shift with respect to changing ambient temperature. For our calculations, we used a previously measured thermal sensitivity of 0.06nm/K, and related the modal shift to a temperature rise, ΔT_1. ΔP_2 is found simply by multiplying ΔI_2 by ΔV_2 taking into account the external efficiency of the device. The average external (or wall plug) efficiency of the individual $14 \mu m$ devices was typically ~5%.

Typically the thermal isolation relationship with r can be modeled by the simple linear function given by:

$$Z_{12} = 2 \pi \sigma_{th} r$$

where σ_{th} is defined as the material conductivity. This relationship is obtained by
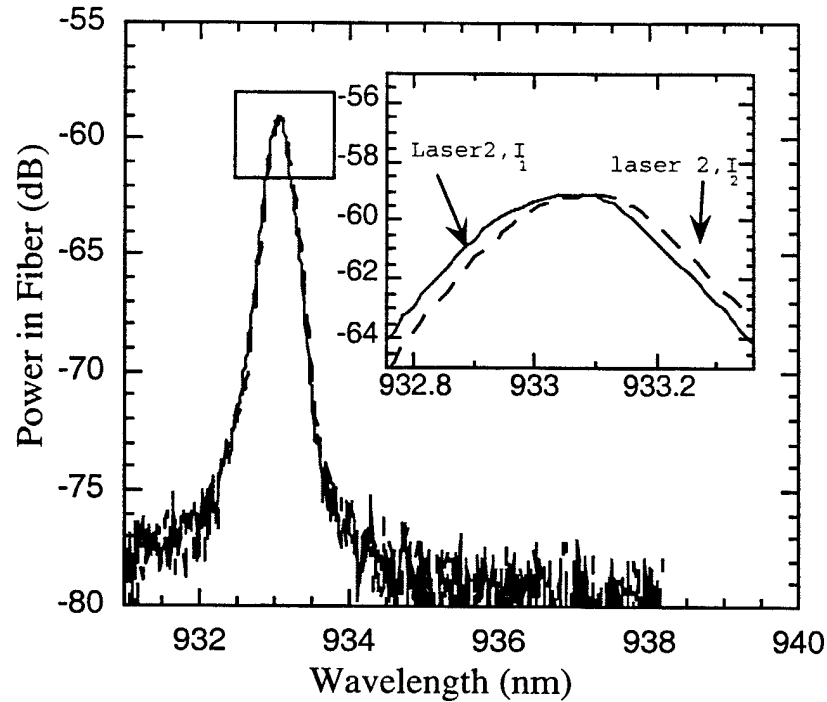
Figure 6.10: Spectra of laser 1 as current in neighboring laser 2 is increased from
I=3mA to I=2mA

calculating the local temperature rise $\Delta T(\mathrm{r})$ in a semi-infinite medium at a distance r

caused by a heat source of power ΔP. This temperature is simply given by $\Delta T(\mathrm{r})=$

$\Delta P/2(\sigma_{th}\pi r)$. The thermal isolation data, shown in Fig. 6.11 measured on 14μm oxidized

VCSELs tested with CW bias, at room temperature (and low current levels) shows that

the thermal isolation approximately follows a linear relationship from which we can

extract a value for the transverse thermal conductivity σ_{th}. From the linear fit, we find

thatσ_{th}= 0.057W/cm.K. This value is the lateral thermal conductivity and is much lower

than the bulk GaAs transverse thermal conductivity $(\sigma_{GaAs}$=0.45W/cm-K). Intuitively,

this is expected since heat must flow through the thick DBR prior to traveling laterally.
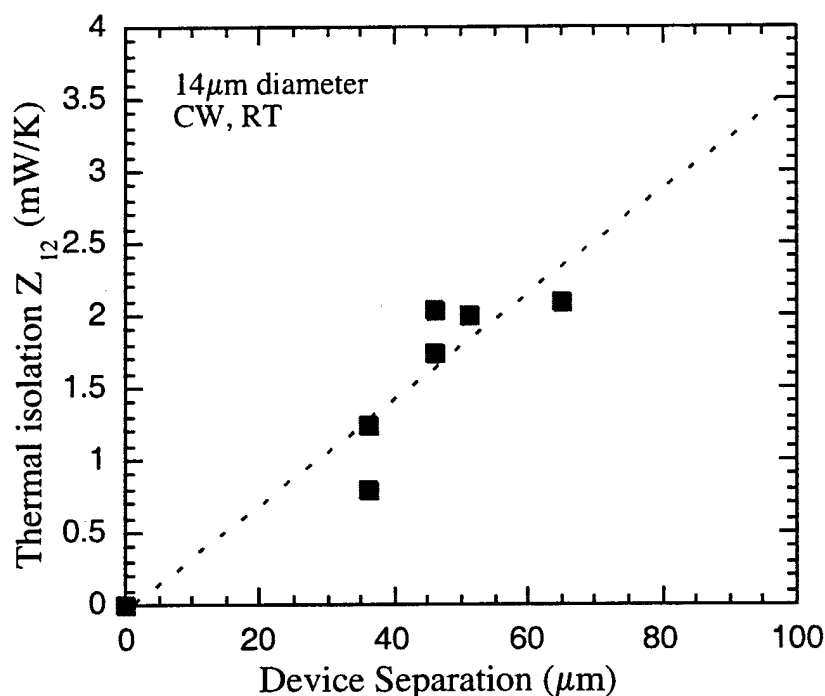
Figure 6.11: Thermal isolation vs. separation for 14μm devices measured at room temperature.

6.3.3 Temperature Dependence of Output Power

Laser design and operating conditions affect the temperature dependence of the output power. It has been demonstrated [13] that a large offset between the spectral gain maximum and the lasing mode at room temperature can lead to a compensation for the lower optical gain at higher temperatures, providing a fairly constant output power for a fixed driving current. In contrast, the lasers in the present study were designed in a way that the gain and mode are well aligned at room temperature. Therefore we expect the output power to decrease with increasing ambient temperature for a fixed laser current as
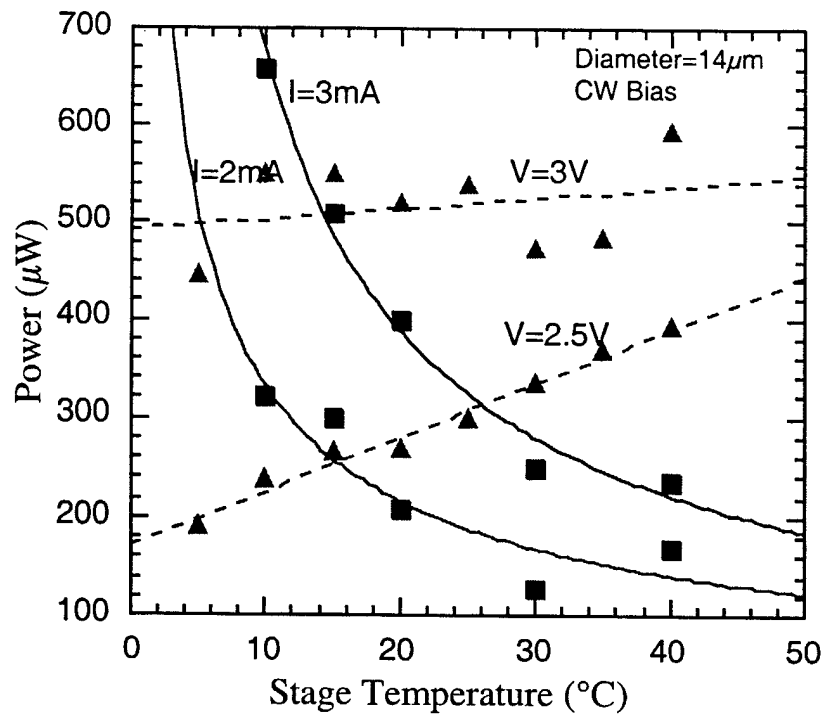
Figure 6.12: Output power as a function of laser stage temperature under constant voltage (dashed) and constant current (solid) operation

shown in Fig. 6.12. We find that the output power of this 14μm device drops exponentially with rising temperature. On the other hand, a temperature insensitive output power level can be achieved in these lasers under constant voltage operation. The higher device temperature decreases the series resistance especially for the resistive top Bragg reflector layers. At high temperatures, the laser current increases for a fixed voltage compensating for the lower gain. The output power stays fairly flat at 3V over a fairly large range of temperature. This can prove useful for various high power applications.

6.3.4 Modal Properties of Arrays

The lateral mode behavior of VCSELs depends mainly on how the carriers are injected into the active region and the spatial gain profile. Spatial hole burning due to saturation of the gain has been identified as the main mechanism whereby a higher order becomes dominant over a lower order mode[14]. As the device diameter is reduced to ~10μm, the optical modes become restricted. The field is cosine-like and is nearly zero near the edges of the aperture due to the large index discontinuity. Since the stimulated emission rate is proportional to the gain and the modal energy density, the current conversion into photons is not uniform across the device. Thus, lateral carrier densities are not uniform; recombination and leakage currents vary radially, resulting in lateral diffusion currents. As the current is increased, the gain will be saturated at the peak of the mode and carriers will recombine faster towards the perimeter of the oxide-aperture, causing a transition to a higher order mode.

In oxide-confined VCSELs, the current injection is not necessarily uniform. The current path from the ring contacts results in higher carrier concentrations of carrier under the perimeter of the aperture, especially for the larger devices. This can also happen with non-uniform oxidation resulting in asymmetric aperture shapes. As a result, the gain profile will be higher around the lateral cavity perimeter. Higher transverse mode operation can therefore be expected, mimicking the effects of spatial hole burning. Thermal lensing (an increase in refractive index due to increase in temperature) and self-focusing are also mechanisms that may result in higher order mode operation of a VCSEL [15].

The mode behavior of several 2x2 arrays was studied using a near-field (NF) measurement set-up. This set-up consists of a Mitutoyo (50X) microscope objective (with a focal length of 1.5cm) - that can be interchanged with lower magnification objectives – and a Navitar Zoom telemicroscope with a Electrophysics 7290a PbS camera

(400nm-1.7μm). The camera is interfaced directly to a computer on which a beam profile analysis software from Spiricon Inc. is run. The maximum resolution attainable with this system is 0.085nm. The camera system is mounted in 3-axis positioners for focusing and aligning. Neutral density filters can be used to attenuate the light from the VCSELs. Although the exact scale of the images is not known, the beam diameters in our images can be estimated from the pitch of the array.

Figure 6.13 shows the 4 array elements at different pulsed current levels. For this measurement, the duty cycle of the pulse was 1%. Assuming the current distribution is uniform across the array, the average threshold current per element is 0.4mA. This is in agreement with results obtained from individual devices. The first two images show the spontaneous emission from the devices. Image 3-4 show the lasers above threshold. From these NF images, we estimate a beam spot size of ~4μm above threshold. The transverse lasing modes very quickly evolve into higher order modes, with each NF intensity splitting . A close look at the NF images reveals a double-lobe pattern (identified as the LP_{10} mode) form, as the current is increased. No significant change in the NF patterns were observed in other 2x2 arrays tested. The transition to the higher LP_{10} mode was observed consistently.

This intensity peak splitting is indicative of spatial hole burning [16]. It has been observed that the mode symmetries follow that of the shape of the active active region [17]. Lasing peaks are favored in the corners of the square region. In addition, a dependence of the lasing transverse mode behavior on mirror reflectivity has also been found. Increasing the mirror reflectivity to maintain single-mode behavior at higher currents may not prove useful in our devices since output power cannot be compromised.

It is therefore concluded that in this case, heat exchange between devices does not play a big role in transverse mode behavior of the arrays, in this case. In addition, we eliminate optical coupling as a cause for the emergence of higher order since the devices are far apart. It is likely that spatial hole burning and non-uniform current injection are

the mechanisms responsible for the multi-mode characteristic of the array. In the future, the effects of heating, may be explored by varying the duration of the pulse.

Image 1

I = 0.3mA

Image 2

I = 0.5mA
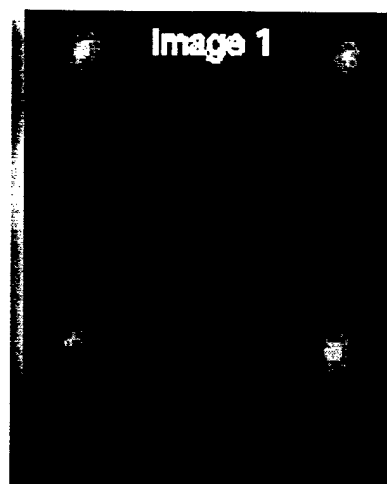
Image 3
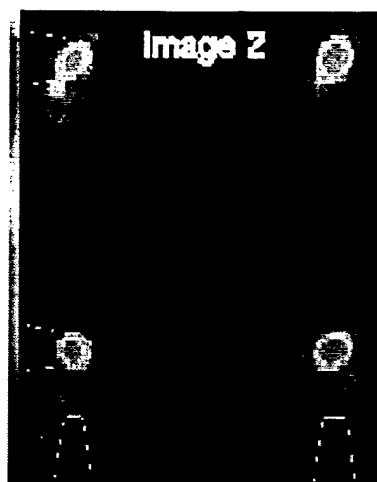
I = 1.6mA

Image 4

I = 2.2mA
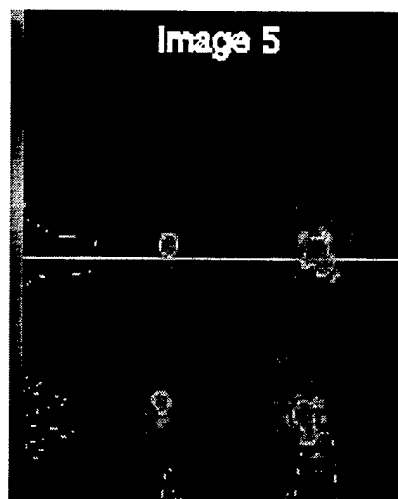
Image 5

I = 2.5mA
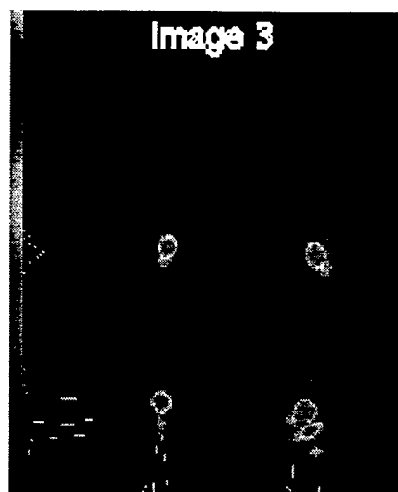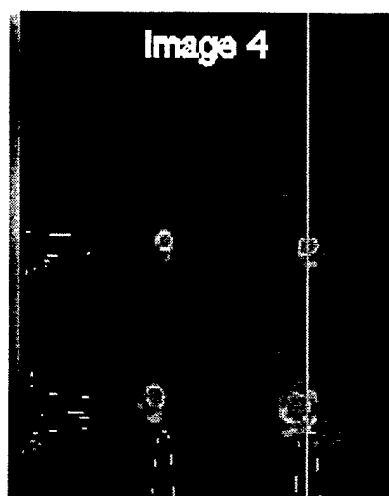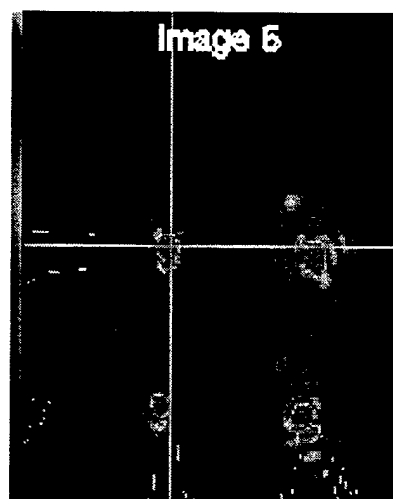
Image 6

I = 5.1mA

Figure 6.13:   Near-field images of 2x2 array with 4μm diameter VCSELs

6.4 Summary

GaAs-based VCSEL arrays with AlGaAs/InGaAs active region were designed and fabricated using a planar process for high power applications applications. Individual devices as well as arrays of varying size were characterized and operated with maximum conversion efficiencies of 5%. We obtain good uniformity in threshold current and scalable power - as measured from different size arrays. 10x10 arrays tested, gave output powers in excess of 60mW (with less than 90 elements lasing and limited by the current supply), with a 3.5% conversion efficiency. The thermal crosstalk in 4x4 VCSEL arrays was also investigated. The experimental number obtained for the average lateral thermal conductivity is 0.057W/cm.K. The ouput power of the lasers is fairly temperature insensitive under constant voltage operation.

The transverse mode behavior of a 2x2 array was studied and eliminated optical coupling as a cause for the emergence of higher order since the devices are far apart. It is likely that spatial hole burning and non-uniform current injection are two possible mechanisms responsible for the multi-mode characteristic of thefabricated arrays.

References

[1] R. A. Morgan, M. K. Hibbs-Brenner, "Vertical cavity surface emitting laser arrays", invited paper, *SPIE-OE LASE 95, Photonics West*, Vol. 2398, pp. 65-93,1995

[2] G. A. Evans and J. Hammer, *Vertical Cavity Surface Emitting Laser Arrays*, Academic Press, San Diego, CA 1993

[3] T. Kurokawa, S. Matso, T. Nakahara, K. Tateno, Y. Ohiso, A. Wakatsuki and H. Tsuda, "Design approaches for VCSEL's and VCSEL based smart pixels toward parallel optoelectroenic processing systems", *Appl. Optics.*, Vol 37(2), pp.194-204, 1998

[4] R. Jager, M. Grabherr, C. Jung, R. Michalzik, G. Reiner, B. Weigl and and K. J. Ebeling, " 57% wall plug efficiency oxide confined 850nm wavelength GaAs-VCSELs", *Electron. Lett.* Vol. 33, pp. 330-331, 1997

[5] K. Lear, D. D. Choquette, R. P. Schneider, S. P. Kilcoyne and K. M. Geib, "Selectively oxidized VCSELs with 50% power conversion efficiency", *Electron. Lett.* Vol. 31, pp. 208-209, 1995

[6] M. Grabherr, B. Weigl, G. Reiner, R. Michalzik, M. Miller and and K. J. Ebeling, "High power top surface-emitting oxide-confined vertical cavity laser diodes", *Electron. Lett.* Vol. 32, 1996

[7] K. D. Choquette, H. Q. Hou, K. M. Geib, and B. E. Hammons, "Uniform and high power selectively oxidized 8x8 VCSEL array", *IEEE LEOS Annual Meeting*, p.11, (1997)

[8] D. L. Huffaker, L. A. Graham and D. G. Deppe," Fabrication of High-Packing-density vertical cavity surface emitting laser arrays using selective oxidation", *IEEE Photon. Tech. Lett.*, Vol. 8(5), pp. 596-598,1996

[9] B. J. Thibeault, J. W. Scott, M. J. Peters, F. H. Peters, D. B. Young and L. A. Coldren,"InGaAs/GaAs vertical cavity surface emitting lasers", *Electron Lett.*, Vol. , 1993

[10] M. Grabherr, R. Jager, M. Miller, C. Thalmaier, J. Heerlein, R. Michalzik, and K. J. Ebeling, " Bottom emitting VCSEL's for high-CW optical output power", *IEEE Photon. Tech. Lett.* Vol. 10(8), pp. 1061, 1998

[11] G.P. Agrawal and N. K. Dutta, *Semiconductor Lasers*, Van Nostrand Reinhold, New York, 1993

[12] T. Wipiejewski, D. B. Young, B. J. Thibeault, and L. A. Coldren," Thermal crosstalk in 4x4 vertical cavity surface emitting laser arrays", *IEEE Photon. Tech. Lett.* Vol. 8(8), 1996

[13] D. B. Young, J. W. Scott, F. H. Peters, M. G. Peters, M. L. Majewski, B. J. Thibeault, S. W. Corzine and L. A. Coldren, "Enhanced performance of gain-offset high barrier vertical-cavity surface emitting lasers", *IEEE J. of Quantum Electron.* , Vol. 29, pp.2013-2022,1993.

[14] R. A. Morgan, G.D. Guta, M. W. Focht, M. T. Asom,K. Kojima, L. E. Rogers, S.E. Callis, "Transverse mode control of VCSELs", *IEEE Photon. Tech. Lett.* Vol. 4, pp.374-377, 1993.

[15] G. C. Wilson, D. M. Kuchta, J. D. Walker, J. S. Smith, "Spatial hole burning and self-focusing in VCSEL diodes", *Appl. Phys. Lett.*, Vol. 64,pp.542-544, 1994.

[16] C.J. Chang-Hasnain, J. P. Harbison, G. Hasnain, A. C. Von Lehmen, L. T. Florez, and N. G. Stoffel, "Dynamic, Opolarization, and transverse mode characteristic of vertical cavity surface emitting lasers",*IEEE J. of Quantum. Electron.*, Vol. 27(6), 1991.

[17] D. L. Huffaker and D. G. Deppe and T.G. Rogers, "Transverse-mode-behavior in native oxide defined low threshold vertical cavity lasers", *Appl. Phys. Lett.*, Vol. 65(13), 1994.

7. CONCLUSIONS

"One moment there had been nothing but darkness; next moment a thousand points of light leaped out-..."[*]

7.1 Summary

7.1.1 Long Wavelength Patterned VCSELs

Long wavelength (1.3-1.55μm) VCSELs are a promising new generation of light sources for optical communication systems and optical interconnects. Several advanced concepts of LW-VCSELs have been developed to overcome the inherently poor material properties and the small variation in refractive index of the InGaAsP/InP system. The most successful has been the utilization of InP/GaAs wafer fusion that led to CW operation. However, several shortcomings of this technology including: the inability to wafer-scale fabricate and test VCSELS utilizing it, the lack of reliability data, and their poor thermal performance, have led to the emergence of new alternate technologies, such as the one presented here. This dissertation explores the design, fabrication and characterization of an all-epitaxial InP-based patterned VCSEL with a GaAs-based top DBR mirror.

---

[*] C. S. Lewis, *The Magician's Nephew* (1955)

135

In Chapter 2, the growth of defect-free strained GaAs/AlGaAs layers on patterned substrates (mesas or grooves) up to thicknesses far exceeding the critical thickness was shown possible. Defect nucleation and propagation are inhibited in such growth. We have exploited this property to propose a novel InP-based 1.55μm vertical cavity surface emitting lasers (VCSELs). Careful photo-luminescence and TEM studies have confirmed that there are no propagating defects in the GaAs/Al$_x$Ga$_{1-x}$As DBR grown on the patterned InP-based heterostructures, specifically in the MQW region.

The oxidation of InAlAs, lattice matched to InP, was characterized for 475°C-525°C for use in long wavelength VCSELs, in Chapter 3. It was found that InAlAs oxidizes at 475°C with no damage to the substrate. The oxidation rate was found to be almost 5 times faster when InP was used as the adjacent layer. This dependence on adjacent layer composition (resulting in a faster rate), is especially important when making oxide-confined InP-based VCSELs. The lateral oxidation of InAlAs was also characterized as a function of thickness, and doping. It was shown that the oxidation rate of InAlAs drops significantly when the layer is 600Å. This may be indication that the oxidation mechanism becomes reaction-limited.

The electrical properties of oxide-confined VCSELs are affected by generation and recombination at the oxide/semiconductor interface. In VCSELs, it is imperative to understand how carrier injection into the active region is altered by recombination centers at the oxide aperture. No direct comparison of the oxidized AlAs/GaAs and Al$_x$Ga$_{1-x}$As/GaAs (for x<1) interface recombination properties had been made thus far. For the first time, a quantitative approach is undertaken by measuring the lifetime of minority carriers in the vicinity of the oxide/semiconductor interface and by estimating the surface recombination velocities near the GaAs/ Al$_x$Ga$_{1-x}$As interface for x=1, 0.98 and 0.96, using the light beam induced current technique (LBIC).

Chapter 4 and 5 included a detailed discussion of the choice of Distributed Bragg Reflectors. Lasers were designed with InP/InGaAsP bottom mirrors, InAlAs-oxide

current confinement and short-stack GaAs/Al$_x$O$_y$ top DBR mirrors. An optimal reflectivity and maximum wall plug efficiency were determined analytically for this structure. In addition, a theoretical analysis of the modulation response of this device is performed using a rate equation model. Both analyses showed the potential of such a device for implementation in practical designs where high power and modulation bandwidth are required. Lasers with 8-40μm diameter have been fabricated and characterized. A threshold current of 5mA is observed at 15°C for an 8μm diameter device; and up to 60μW of light output is recorded. The various loss mechanisms preventing the device from operating under CW conditions were also identified.

7.1.2 GaAs-based VCSEL Arrays

In Chapter 6, oxide-confined VCSEL arrays were realized. GaAs-based VCSEL arrays with AlGaAs/InGaAs active region were designed and fabricated using a planar process for high power applications. Individual devices as well as arrays of varying size were characterized and operated with maximum conversion efficiencies of 5%. We obtain good uniformity in threshold current and scalable power - as measured from different size arrays. 10x10 arrays tested, gave output powers in excess of 60mW with a 3.5% conversion efficiency (with close to 90 elements lasing and limited by the current supply). The efficiency is expected to increase with more efficient heat removal through improved heat-sinking techniques.

The thermal crosstalk in 4x4 VCSEL arrays was also investigated. Thermal isolation >2mW/K was measured for devices separated by 60μm. The experimental number obtained for the average lateral thermal conductivity is 0.057W/cm.K. The output power of the lasers is fairly temperature insensitive under constant voltage operation. The transverse mode behavior of a 2x2 array was studied and eliminated optical coupling as a cause for the emergence of higher order since the devices are far

apart. It is likely that spatial hole burning and non-uniform current injection are two possible mechanisms responsible for the multi-mode characteristic of the fabricated arrays.

7.2 Suggestions for Future Work

This work has shown that the direct growth of high-quality GaAs-based DBR mirrors on InP-based VCSEL heterostructures is possible, eliminating the need for fusion. This technique was successfully applied to the design and fabrication of 1.55μm VCSEL. Continued effort toward lower thresholds, higher powers, longer lifetimes and shorter wavelength (specifically 1.3μm), is a logical extension of this work.
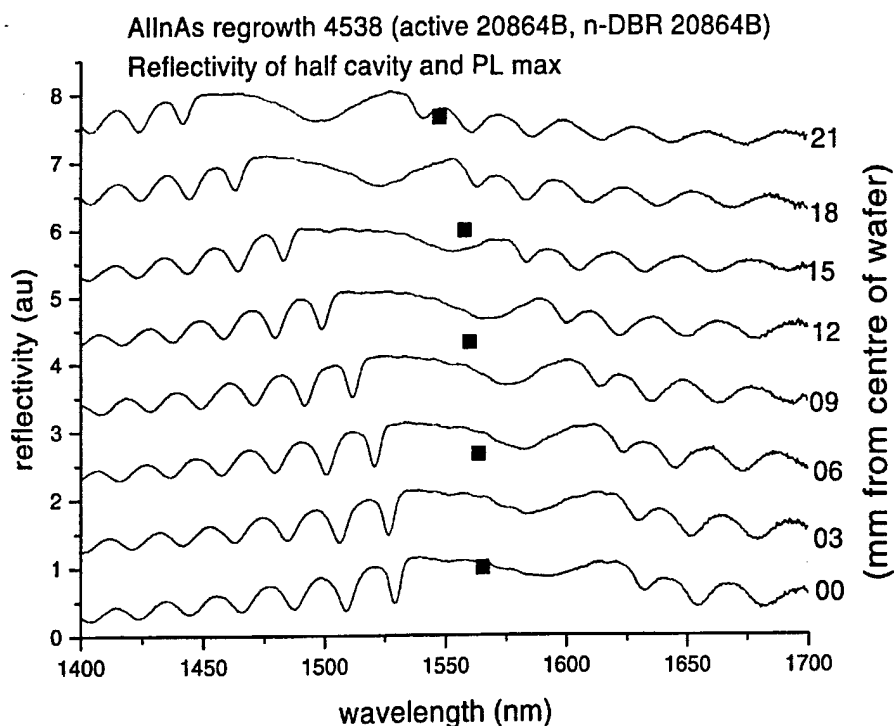
Figure 7.1: Relative reflectivity measurement on VCSEL - 49.5 InP/InGaAsP and cavity (grown at the *Royal Institute of Technology* by MOVPE)

The following is a brief list of suggestions for future work on long-wavelength patterned VCSELs, motivated by interesting device physics, manufacturing issues and emerging technological applications. In addition, continued advances in the growth of InP/InGaAsP DBRs are essential, as are advances in the fabrication techniques of these devices (ie. the elimination of saturated bromine water etch and/or the development of non-carbon based dry-etchants for InP-based materials). Specific suggestions follow.

1) MOVPE Growth Of InP/InGaAsP Bottom Mirror and Cavity

We have discussed the importance of MOVPE growth uniformity especially since the lasing wavelength is determined by the resonant wavelength. It is crucial to measure the reflectance at numerous points on an MOVPE-grown InGaAsP/InP mirror wafer. In addition, it is significant to measure the corresponding PL peak at these points. Figure 7.1 shows data obtained on a recently grown InP/InGaAsP wafer. From this data one can
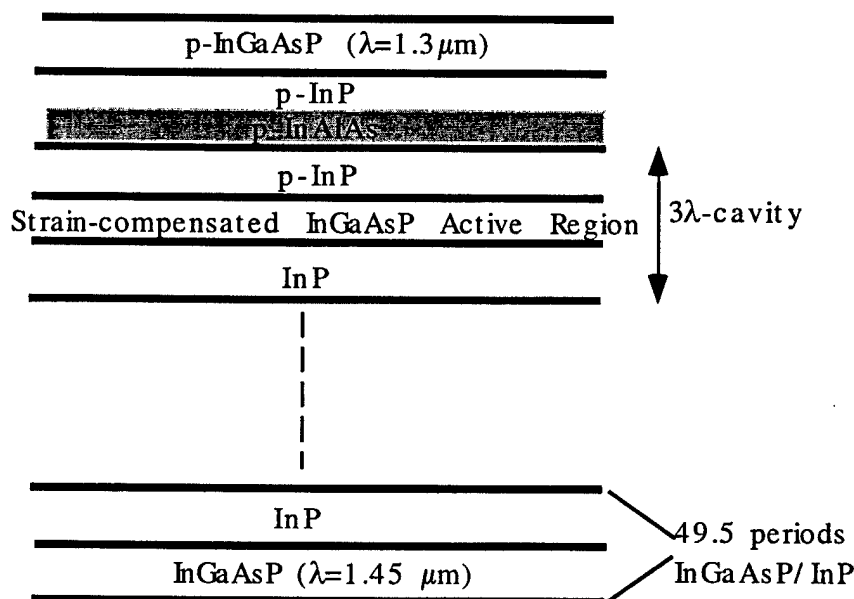
Figure 7.2:   Design of second-generation 1.55μm VCSEL

find the gain-offset at room temperature and process the areas of optimal value.

2) Improved Design of 1.55 μm Patterned VCSEL:

A 1.55μm VCSEL cavity utilizing InP spacers should be used for improved thermal performance. The thermal conductivity of InP is 0.68 W/cm-K; one order of magnitude higher than InGaAsP alloys'. Using InP in the cavity, as in Fig. 7.2, will reduce the overall active region temperature. It is also imperative to extend this well-developed fabrication process to making 1-D and 2-D arrays of 1.55 μm patterned VCSELs[1].

3) Simulation and Analysis of 1.55μm Patterned VCSEL:

A 3-D finite element code (ANSYS) can be used to solve for the steady state heat conduction equation and to obtain a cylindrical symmetrical temperature distribution $T(r,z)$ within the VCSEL. The appropriate thermal conductivities should be used [2]. The thermal conductivity of GaAs/Al$_x$O$_y$ mirror is unknown, and should be investigated. Calculated temperature profile and temperature of the active region as a function of injection current should be used to simulate the optical gain and threshold current accurately. Temperature dependent loss mechanisms and all leakage currents contributing to the threshold current should be considered [3].

4) Microcavity LEDs and Lasers:

In general, the way to reduce threshold current is to reduce the active volume of the VCSEL (threshold current scales with active volume). Another important reason is that it enhances the coupling of the spontaneous emission into a lasing mode, which would enable the zero-threshold operation via the "cavity quantum effect" [4]. With the

research done here on the oxidation of InAlAs, 1.55μm oxide-confined vertical microcavity lasers with high contrast GaAs/Al$_x$O$_y$ mirrors can be achieved.

This will require more work to control the lateral oxidation rate more accurately. In addition, TEM characterization of the InAlAs-oxide/InP interface is needed. Another technique that may be used is the light beam induced current technique (LBIC) which will enable the measurement of the minority carrier diffusion lengths near this interface [5].

References

[1] S. Rapp, J. Piprek, K. Streubel, J. Andre, E. Rodriguez Messner, and J. Wallin, "Temperature performance of 1.55μm vertical cavity surface emitting lasers with integrated InP/InGaAsP Bragg Reflectors", *Proceedings of IEEE IPRM* 1997, Cape Cod, MA, pp.36-39,1997

[2] J. Piprek and S. J. B. Yoo, "Thermal comparison of long waveklength vertical cavity surface emitting laser diodes", *Electron. Lett.,* Vol. 30, pp. 866-868, 1994

[3] J. Piprek, D. I. Babic and J. Bowers, "Simulation and analysis of 1.55μm double-fused vertical cavity lasers", *J. Appl. Phys.* Vol. 81(8), pp.3382-3390, 1997.

[4] I. Vurgaftman and J. Singh, "Steady state and transient characteristics of microcavity surface emitting lasers with compressively strained quantum well active regions", *IEEE J. of Quantum Electron.* Vol.31(5), pp. 852-863, 1995

[5] H. Gebretsadik, K. Zhang, K. Kamath, X. Zhang and P. Bhattacharya, "Recombination characteristics of minority carriers near the Al_xO_y/GaAs interface using the light beam induced current technique", *Appl. Phys. Lett.,* Vol.71(26), p.3865(1997)